



City Research Online

City, University of London Institutional Repository

Citation: Hussein, S. (1997). Characterisation of Planar Defects in Solids Using Ultrasonic Pulse Echo Techniques. (Unpublished Doctoral thesis, City, University of London)

This is the accepted version of the paper.

This version of the publication may differ from the final published version.

Permanent repository link: <https://openaccess.city.ac.uk/id/eprint/31112/>

Link to published version:

Copyright: City Research Online aims to make research outputs of City, University of London available to a wider audience. Copyright and Moral Rights remain with the author(s) and/or copyright holders. URLs from City Research Online may be freely distributed and linked to.

Reuse: Copies of full items can be used for personal research or study, educational, or not-for-profit purposes without prior permission or charge. Provided that the authors, title and full bibliographic details are credited, a hyperlink and/or URL is given for the original metadata page and the content is not changed in any way.

**CHARACTERISATION OF PLANAR DEFECTS IN SOLIDS
USING ULTRASONIC PULSE ECHO TECHNIQUES**

by

SALAH A-R. AHMED HUSSEIN.

Thesis submitted for the degree of

DOCTOR OF PHILOSOPHY

**Department of Electrical, Electronic and
Information Engineering**

City University

London

October, 1997

CONTENTS

ACKNOWLEDGEMENTS	I
COPYRIGHT DECLARATION	II
ABSTRACT	III
1- INTRODUCTION	1
2- THEORY	4
2.1 Propagation of sound in a fluid using the impulse response method	5
2.1.1 Impulse response method to calculate pulse echo waveforms for a point-like target in a fluid	8
2.2 Propagation of sound in a solid	9
2.2.1 Impulse response method to calculate the propagation of sound in a solid	11
2.2.2 Mode conversion	14
2.2.3 Vector particle velocities	15
2.2.4 Calculated impulse responses and particle velocity waveforms	17
2.2.5 Pulse echo waveforms for a point-like target in a solid	21
2.2.6 Physical explanation of the form of the echo responses	26
2.2.7 Echo response of finite size targets in a solid	30
2.3 DGS diagrams	36
2.4 Numerical calculations	43
3- EXPERIMENTAL MEASUREMENTS	46
3.1 The transducers	46
3.2 The targets	46
3.3 Experimental set-up for short pulse measurements	47
3.3 Experimental set-up for multi-cycle pulse measurements	49

4- RESULTS	53
4.1 Experimental factors affecting the measurements.....	54
4.1.1 Measurements of radius of the transducer	54
4.1.2 Uncertainties in measurements of the echo responses	55
4.2 Echo responses from point-like targets in steel	57
4.3 Echo responses from FBH's in aluminium	59
4.3.1 Echo responses from 2mm and 4mm FBH targets	59
4.3.2 Variation of echo response with target size	63
4.3.3 Variation of echo response with target range in the near field	68
4.3.4 Effects of uncertainties in transducer radius	74
4.4 New DGS diagrams for FBH targets in a solid medium	78
4.4.1 Measured and calculated DGS diagrams for 2mm targets	78
4.4.2 Effect of the source velocity function on DGS diagrams	83
4.4.3 Effect of the method of amplitude detection on DGS diagrams	93
4.4.4 Effect of transducer radius on DGS curves	96
4.5 Comparison between DGS diagrams calculated using the solid and fluid models..	99
5- DISCUSSION: IMPLICATIONS AND APPLICATIONS FOR NDT	107
5.1 Interference effects on the echo response	107
5.1.1 Short pulses	107
5.1.2 Multi-cycle pulses	108
5.2 Defect sizing using DGS diagrams	110
5.3 Application of the model as theoretical calibration blocks	113
6- SUGGESTED FUTURE WORK	124
7- CONCLUSIONS	125
REFERENCES	128

ACKNOWLEDGEMENTS

I am most indebted to Dr. J. P. Weight for his constant supervision, valuable advice, and helpful support. I am also very grateful to the Electrical, Electronic, and Information Engineering department for their support; to Professor A. F. Brown for his comments and helpful suggestions on the manuscript. Finally, I would like to thank everybody who supported me during my studies.

I am also deeply indebted to my father, mother, and Mrs Ali and all my relatives and friends for their forbearance, unwavering backing.

Copyright declaration

I grant power of discretion to the university librarian to allow this thesis to be copied in whole or in part without further reference to me. This permission covers only single copies made for study purpose, subject to normal conditions of acknowledgements.

ABSTRACT

With the use of ultrasonic transducers, the relation between defect sizes and ranges with their echo amplitudes has been investigated both theoretically and experimentally. It is demonstrated that this relation is affected by diffraction effects which also complicate the interpretation of echo signals. These diffraction effects are interpreted in terms of compression plane and edge waves together with mode-converted shear edge waves emanating from a circular compressional transducer.

The investigation has been established with the aid of a model that predicts echo responses for flat-bottomed holes (FBH) in isotropic lossless solids interrogated by uniformly excited sources. The results predicted by the model are in good agreement with experimentally measured results obtained using commercially available wide and narrow band circular transducers.

It has been shown experimentally and theoretically that, using transducers excited with multi-cycle pulses produces large fluctuations with range in echo amplitudes for small targets. These fluctuations might result in misinterpretations of target size. The fluctuations disappear when a short pulse is used to excite the transducer.

The model is also used to obtain new distance-gain-size (DGS) diagrams that can predict the significant response variations in both the near and the far fields of a transducer. Calculated DGS diagrams have shown good agreement with experimentally obtained curves for small FBH targets positioned mostly in the near field of the transducer.

Factors like the transducer radius, excitation-pulse shape, and the method of calculating the echo amplitude have been shown to affect DGS diagrams, especially for the case of small targets in the near field. The new model provides the explanation of these effects.

A comparison between the new curves and curves produced using an earlier fluid model showed that there are significant differences between both curves, especially for small targets. Therefore, care should be taken when the fluid model is used to estimate target size in a solid medium.

1- INTRODUCTION

Ultrasonic pulse echo methods have many applications in the nondestructive testing of materials, including material evaluation and defect detection and characterisation. The detection of defects has been considered to be easier than their characterisation (Krautkramer, 1959) because of several factors. These are defect type, shape and the roughness of its surface, the ultrasonic beam behaviour in the material, and the electronics involved in the process of testing.

An early attempt to size defects was introduced by Krautkramer in 1959 in which he related the echo amplitude for flat disc-like defects to their size and distance from the transducer in a fluid medium. These targets were at right angles to the axis of the radiated field. He defined this relation as Distance Gain Size (DGS) diagrams. However, Krautkramer's diagrams were produced theoretically for targets in the very far field of the probe. The rest of the diagrams for targets in the near field were completed experimentally. For targets within the near field of the transducer, it was noted that there were fluctuations in the echo amplitudes with range. These fluctuations increase as target sizes decrease.

Since then, this method of defect sizing has been widely used in many countries and it was considered to be a very important step in solving the defect sizing problem. However, the method is not without its drawbacks. For example, The reason for fluctuations in the echo amplitude for small targets positioned in the near field of the probe was to a certain extent not known. Also, the same method was used for defect sizing in solids, while originally it had been developed for targets in a fluid medium. These setbacks meant that it was very important to understand the propagation of ultrasound in a solid medium, its interaction with targets and the corresponding echo waveforms on reception.

Consequently, many approaches have been made towards this understanding. For example, solving the elastodynamic equations (EDE), (Schmerr and Sedov, 1989) The main setback of this approach is the length of time required. Another approach was using the geometrical theory of diffraction (GTD), (Chapman, 1988).

However, this approach used continuous wave theory and assumed the propagated waves to be plane

A different approach was the transient field theory. In this theory most calculations of transient piston fields have been based on a convolution integral representation (Stepanishen, 1971). This integral introduces the concept of an impulse response which relates the acoustic field to the radiating source geometry. Using the same transient field theory, the propagation of sound in a fluid medium has also been defined using the concept of plane and edge waves (Weight and Hayman, 1978). With the aid of the same concept, the propagation of sound in a solid medium (Weight, 1982, 1987) and the echo responses of small targets in solids (Weight, 1993) were modelled.

The approach given by Weight (1993), gave the ability to develop a model that can predict the echo responses from flat-bottomed hole (FBH) targets of various sizes (as will be seen later in Chapter 2). The study of the echo responses of such targets is one of the objectives of this thesis.

Other important objectives are the applications of the new model in defect sizing in solids. As mentioned earlier, the first method introduced for defect sizing was the use of DGS diagrams for targets in a fluid medium. It is intended that this model will be able for the first time to produce full theoretical DGS diagrams for targets in a solid medium. Also, it will provide a quantitative explanation for the fluctuations in the amplitude of the echo response for the same target size with range and the reason behind the reduction in these fluctuations as the target size increases. A comparison between the new DGS diagrams constructed using the new model and the diagrams produced using the fluid model is given. At this point, it is very important to mention that only aspects relating to the propagation of ultrasound from the transducer face and its subsequent scattering and reception in pulse-echo mode are considered and not the electro-acoustic modelling to relate the motion of the transducer to the electrical excitation pulse.

Briefly, the material presented in this work is laid out as follows:

Chapter 2 begins by introducing, briefly, the transient theory for propagation of sound in a fluid, as well as the impulse response method for the calculation of pressure waveforms and transmit-receive mode responses for uniformly excited transducers. Next, the extension of the impulse response method to model the propagation of sound in a solid is reviewed. This is followed by a discussion of the origin of the mode-converted shear waves radiated from normally coupled transducers. Then, extension of the theory to predict the echo response of small targets in a solid medium is reviewed. This leads to a model which predicts the echo response of finite sized targets in a solid medium.

A brief review of the origin of DGS diagrams follows. The advantages and disadvantages of these diagrams as a method of defect sizing and new developments in this method are discussed. Chapter two finishes with the numerical calculations implemented for the impulse responses and the echo responses for finite-sized targets.

Chapter 3 describes the transducers and measuring systems used to obtain the experimental waveform measurements presented in this work.

Detailed calculations of transmit-receive mode responses from targets of various sizes in a solid medium are given in Chapter 4. These calculations are compared with experimental results obtained using conventional narrow- and wide-band transducers. The applications of this model in producing new DGS diagrams for targets in solids are shown and are experimentally verified for both narrow and wide band transducers. Some other factors that can affect DGS diagrams, like the method of detecting the echo amplitude are discussed. Also, a comparison between the diagrams produced using the new model and diagrams produced using the fluid model is shown.

Chapter 5 deals with the implications of the results in Chapter 4 for defect detection and sizing in practical NDT.

Proposed future work and developments are given in chapter 6, followed by conclusions of this work in chapter 7.

2- THEORY

Much of the theoretical and experimental work presented in this thesis is associated with the propagation of ultrasound in a solid medium, its interaction with targets within the solid and the reception of the ensuing scattering back at a single transducer. This is generally more complicated than the corresponding problem with a fluid medium of propagation, because shear waves as well as compression waves can propagate in a solid. For this reason, the theory for solids is introduced by first briefly reviewing the existing impulse response theory for fluids (after Weight and Hayman 1978). This is followed by a more detailed review of a model used to predict the echo responses of point-like targets in solids (Weight 1993). This model is then extended to deal with finite sized targets in solids. Finally, the use of the new model as a tool to size defects in solids is discussed.

2.1 Propagation of sound in a fluid using the impulse response method

Rayleigh's equation for arbitrary motion of a source radiating into a fluid expresses the velocity potential at a point as the sum of contributions from all the elementary Huyghens sources that make up the source surface. This gives

$$\phi(r, t) = 1/2\pi \iint_S v \frac{(t-\frac{r}{c})}{r} ds, \quad (1)$$

where ϕ is the velocity potential, v is the normal velocity of the piston, r is the distance from the field point to the surface element ds and c is the velocity of sound in the fluid.

The pressure in a fluid of density ρ is then given by

$$p(r, t) = \rho \partial \phi / \partial t. \quad (2)$$

If the piston velocity v is uniform over the piston surface then by using the shifting property

$$v(t - \frac{r}{c}) = v(t) * \delta(t - \frac{r}{c}), \quad (3)$$

where $*$ denotes convolution.

Assuming a linear-time invariant system, the velocity potential for arbitrary motion $v(t)$ of the source is then

$$\phi(r, t) = v(t) * \phi_i(r, t). \quad (4)$$

and the impulse response ϕ_i is

$$\phi_i = \iint_S \delta \frac{(t-\frac{r}{c})}{2\pi r} ds. \quad (5)$$

After a velocity impulse has been applied to a piston at $t = 0$, the field at point Q is made up of contributions from all points on the piston surface a distance ct from Q . These equidistant points lie on a circular arc centred at the projection of Q on the source plane, as shown in Figure 2.1.1.

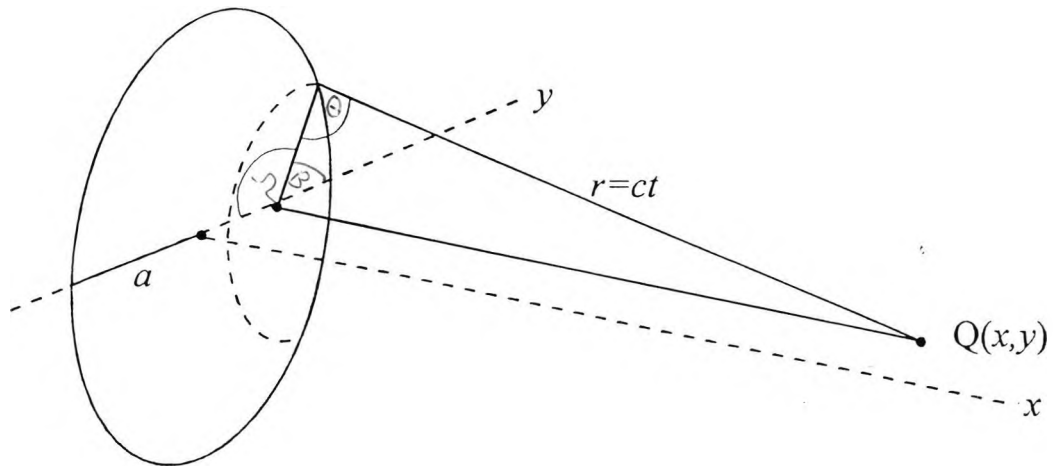


Figure 2.1.1: Geometry for a circular source of radius α , propagating in a fluid medium, showing the angle subtended at the transducer circumference from a point Q on the medium. The angle Ω is the included angle of an arc on the transducer surface, each point on the arc being equidistant from Q .

By a simple change of variable (Stepanishen, 1971), a very useful result is obtained for the solution to Eq (1), namely that the velocity potential for an impulsive motion of a source is proportional to the length of equidistant arc included in the source surface. Mathematically this is

$$\phi_i(r, t) = c\Omega(ct)/2\pi \text{ if } r_1 \leq ct \leq r_2 \quad (6)$$

and $\phi_i(r, t) = 0$ elsewhere, where Ω is the full angle of the included equidistant arc, r_1 and r_2 are the distances from the field point to the near point and the far point of the source circumference, respectively. For the case of a circular source analytic expressions for $\Omega(ct)$ have been given by a number of authors using the law of cosines, those tabulated by Robinson (1974) are summarised in the appendix. The

pressure impulse response may then be obtained by numerical differentiation and convolved with the source velocity motion to give the pressure response as:

$$p = v(t) * p_i, \quad (7)$$

where

$$p_i = \rho \partial \phi_i / \partial t \quad (8)$$

Weight and Hayman (1979), introduced a physical explanation that follows from Eq (7) which said that the field structure for a circular source emanating in to a fluid medium consists of plane and edge waves. The plane wave travels in the geometrical beam region straight ahead of the transducer. The edge wave travels as a spreading wave from the edge of the transducer and has a toroidal wavefront. As an aid to clarify the concept of plane and edge waves Figure 2.1.2 shows a schematic representation for these waves. Since in this thesis more attention is given to the propagation of sound in solids as seen later in section (2.2), more details about the propagation of sound in fluids can be seen elsewhere (Weight, and Hayman, 1978 and 1979)

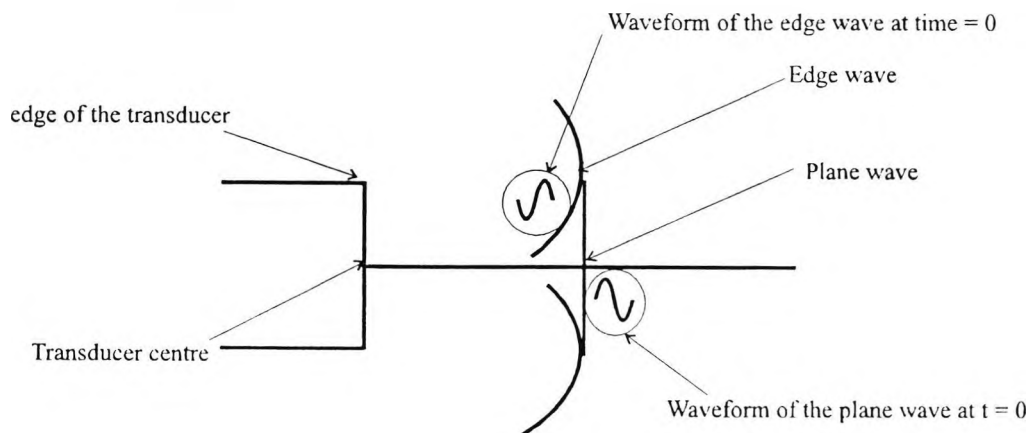


Figure 2.1.2: A schematic representation of the concept of the plane and edge waves emanating from the transducer excited with single sinusoidal pulse. Shown in circles are the opposite polarities of the waveforms at the moment of excitation ($t=0$).

2.1.1 Impulse response method to calculate pulse echo waveforms for a point-like target in a fluid.

By invoking the principle of reciprocity (Weight and Hayman, 1978/ 79), the impulse response method has been extended to allow calculations to be made of the transmit-receive mode response of a uniformly excited source interrogating a point-like target in a fluid. If the source is considered to also function as a receiving transducer that is uniformly pressure sensitive, its output voltage $E(t)$, when used in transmit-receive mode on reception of the echo from an idealised point reflector is given by

$$E(t) = (k\rho/2c)v(t) * \partial\phi_i/\partial t * \partial\phi_i/\partial t, \quad (9)$$

where k is a constant.

The above result is obtained by making the simplifying assumption that the incident wave is locally plane and the target has a reflection coefficient of 1. i.e. the target has an acoustic impedance much smaller than that of the fluid medium in which it is immersed. The double convolution of Eq (9) means of course that the pulse-echo waveform is quite different (Weight and Hayman (1978)) from that obtained for the field point pressure. Predicted echo responses for small targets in fluids using Eq (9), showed good agreement with experimentally obtained echo responses for the same targets (Hayman and Weight, 1979).

2.2 Propagation of sound in a solid

In solids, both longitudinal and transverse waves can propagate, and so the modelling of the propagation of sound in a solid is a harder task than is the case with fluids. Many approaches have been developed. For example, using the Cagniard de Hoop method (1959), Aulenbacher and Langenberg (1983) have given the impulse response and hence the pulsed directivity pattern of a line or point source radiating into a solid half-space. By suitable integration techniques they have extended the line source results to calculate the impulse response of an infinite ribbon source.

Weight (1982) introduced a simple model for the impulse response that can be used to rapidly calculate the propagation of sound in solid. His work is discussed in detail in section 2.2.1.

Kawashima (1984) numerically evaluated the integral expressions for the displacement amplitude for any point in the field of a circular source undergoing continuous sinusoidal motion. He then obtained pulsed displacements by harmonic synthesis.

Ilan and Weight (1987) used the finite difference approach to calculate the time development of displacements within a solid half space. Then they expressed the elastodynamic equations in cylindrical co-ordinates by inserting suitable surface boundary conditions into the equation. From that they calculated the displacements due to a circular source undergoing arbitrary motion.

Bresse and Hutchins (1989) showed how the use of integral transforms and the Cagniard method can give exact, finite integral expressions that can be evaluated numerically for the transient waves generated from axisymmetric sources.

Schmerr and Sedov (1989) calculated the propagation of sound in a solid using an elastodynamic model that uses high frequency asymptotic solutions. This was done for both compression and shear wave transducers that were directly coupled to a solid surface and radiating a short pulse. Interestingly, they demonstrated that within the main beam of the transducer and in the far field, the differences between their model and the fluid model are very small. But, in the near field, the elastodynamic model provides a more complete description of the transducer radiated wave field than does the fluid model. However, they concluded that their solid model agrees very well in many cases with the simpler fluid models that have been used for such problems.

Djelouha and Baboux (1992), modelled the problem of the transient ultrasonic field radiated from a circular source in a solid medium, by a homogeneous isotropic elastic half space whose surface is subjected to a normal load uniformly distributed under the active area of the transducer. Taking account of these particular boundary conditions, they solved the partial derivative equations that govern the propagation of elastic waves using integral transform techniques. The numerical simulation obtained using this formulation showed that the radiated field is relatively complicated because of the diffraction by the transducer edges. The radiated field obtained consists of a compression plane wave propagating in the geometric region straight ahead of the source, together with compression- and shear-edge waves emanating from the transducer circumference.

Baboux and Kazys (1992), studied the transient radiation of ultrasonic fields into isotropic solids by circular sources. Their calculations of the axial and radial components of the particle velocity spatial-temporal distributions were performed using an harmonic synthesis approach. The results obtained were explained in terms of direct, compression-edge, shear-edge and head waves.

Lhemery (1994), introduced an approximate model for the solution of the problem of the radiation of the transient pulses in an elastic medium. In his work Lhemery derived two approximations allowing the proposal of a new integral formula for the

problem of the radiation of transient pulses in an elastic medium by an arbitrary loading. The first approximation was to neglect the first term in Green's dyadic (K. Aki and P. G. Richard, 1980). The second approximation was to ignore the head waves. His results showed good agreement with the exact solutions obtained by Baboux and Kazys (1992).

Most of the above approaches are time consuming in terms of computation even on main frame computers. Since the present work is mainly involved in extremely extensive calculations (like producing DGS diagrams), these approaches would be very time consuming. Hence the need for a model that produces rapid and accurate results has arisen.

2.2.1 Impulse response method to calculate the propagation of sound in a solid.

Plane wave theory predicts that a compression wave obliquely incident on a surface partially mode converts into a shear wave. However, other studies showed the existence of shear waves radiating from normally coupled compressional transducers, (Hall 1977, Hayman and Weight 1977, Saches and Hsu 1978, Ying and Li 1981).

Hayman and Weight (1977) suggested that these shear waves are mode converted edge waves and thus may be considered to be shear edge waves. Evidence to support this hypothesis was given by using a stroboscopic photoelastic system to visualise a short pulse propagating into a fused quartz block.

To show that these waves originate from the edge of the probe and are not due to mode conversion at the edge of the incident compression plane wave, Weight (1982) showed results taken with the transducer water-coupled, at a range of 4mm, to a quartz block. The positions of the compression plane wave and the shear edge wave were marked on a glass slide placed alongside the quartz block.

Then the transducer coupling range was increased to 8mm but the depth of penetration into the quartz remained the same. If the shear edge wave was due to mode conversion at the edge of the incident compression plane wave, the radius of curvature of the shear wave at the new coupling range would be the same as at the 4mm coupling range. However, this was not the case. In fact, consistently with the idea of mode-converted edge waves, the centre of the curvature of the shear edge wave at the 8mm coupling distance was back at the edge of the transducer (allowing for refraction at the fluid/solid interface).

Thus the basis of the model to be used here is to consider that the compression edge wave that propagates from the rim of the transducer partially mode converts into a shear edge wave, the proportion depending on the angle from the field point to each element of the source rim. This is achieved by 'splitting' the compression edge wave component from each element of the source rim into two components, one propagating at the compression wave velocity, the other at the shear wave velocity (Weight, 1987).

It is important that to express the impulsive velocity potential at a point inside the solid as the sum of two Rayleigh diffraction integrals, one for the compression wave the other for the shear wave, is not valid as it stands since the assumptions made in deriving Rayleigh's integrals are only valid for a fluid propagating medium. For instance, such an approach would predict the existence of a shear plane wave from a normally coupled compression wave transducer. This contradicts the theory of the propagation of plane waves across a boundary. However, Weight (1982) suggested that the fluid theory could be used to predict the form of the shear *edge* wave radiated from a normally-coupled transducer. He showed that the the problem of the non-existing shear plane wave also predicted could easily be overcome by simply omitting it from all further calculations.

Thus Weight (1987) expressed the pressure impulse response as,

$$p_{\delta} = \rho c_l [\delta(t - \tau_0) - m_l(\theta) f_l(t - t_l) - (c_l/c_s) m_s(\theta) f_s(t - t_s)]. \quad (10)$$

where $f_i(t - t_i)$ is the edge-wave contribution predicted for a fluid propagating medium having sound velocity c_i and $f_t(t - t_t)$ is that for a medium having sound velocity c_t . The functions $f_i(t - t_i)$ and $f_t(t - t_t)$ are extracted from the impulse response given by Eq (6) and the expressions are listed in the appendix. It should be mentioned that for the on-axis case, these functions reduce to a delta function since, on-axis, the edge wave components are no longer dependant on the angle θ (due to the symmetry around the axis of propagation) and are only dependant on the mode conversion factors. The terms $m_i(\theta)$ and $m_t(\theta)$ are mode conversion factors for compression and shear edge waves respectively and are explained in more detail in section 2.2.2.

Thus $m_i(\theta)f_i(t - t_i)$ and $m_t(\theta)f_t(t - t_t)$ are the compression and shear edge wave components, respectively. t_i and t_t being the arrival times at the field point of the compression and the shear wave contributions from each element of the source circumference. The limits of t_i and t_t are given by

$$r_1/c_i \leq t_i \leq r_2/c_i$$

and

$$r_1/c_t \leq t_t \leq r_2/c_t$$

where, (Figure 2.1.1), r_1 and r_2 are the distances from the field point to the near point and the far point of the source circumference, respectively. The angle θ is now given by

$$\theta = \sin^{-1}(r_0/c_i t_i) = \sin^{-1}(r_0/c_t t_t) \quad (11)$$

2.2.2 Mode conversion

It is convenient at this point to consider the angular variation of the mode conversion factors $m_c(\theta)$ and $m_s(\theta)$. These are dimensionless factors that give the relative amplitudes of the particle velocities of the compression and shear edge waves, respectively. These functions and the constants within them (equations 12 and 13) were empirically derived by Weight (1987) in order to match results predicted using the finite difference method and used in his impulse response model.

$$m_c(\theta) = 1 - e^{-a\theta} \quad (12)$$

and

$$m_s(\theta) = [b\theta e^{(1-b\theta)}]^2, \quad (13)$$

where θ , the angle from each element of the source rim to the field point, is given by

$$\theta = \sin^{-1}(r_0/r_\theta), \quad (14)$$

where r_0 and r_θ are the distances from the field point to the plane and each point of the rim of the source, respectively, and a and b are normalising factors to relate the amplitude of the edge wave components to that of the compression plane waves. Values of a and b may be found by again referring to finite difference results (Ilan and Weight, 1987) to obtain the ratio of the amplitudes of the two edge waves in the normal direction straight ahead of the source rim.

It was found empirically by Weight (1993) that good agreement was obtained between predicted and measured results, if $a = b = 2$.

From Eq (10) the two edge wave components of the impulse response are

$$e_l = \rho c_l m_l(\theta) f_l(t - t_l) \quad (15)$$

$$e_t = \rho c_t m_t(\theta) f_t(t - t_t) \quad (16)$$

2.2.3 Vector Particle velocities

Eq (10) gives the scalar pressure at points in the field of a circular source coupled to a solid. To give a complete treatment for propagation in solids, vector particle velocities are required.

The approach adopted here (Weight, 1987) is to make use of a knowledge of the plane and edge wave structure of the radiated pulses. This, together with considering the wave front as locally plane, will then allow vector particle velocities to be obtained as described below.

Figure 2.2.1 shows a two dimensional schematic representation of the plane and edge waves radiated, including their relative polarities. The convention (Weight, 1987) adopted for the sign of compression and shear wave particle velocities is shown in the same figure. The radial and tangential components of the edge wave portions of the particle velocity impulse response u_δ are denoted u_r and u_θ respectively. The corresponding vertical and horizontal components of the compression wave particle velocities in the plane $z=0$ are denoted by u_{xt} and u_{yt} , respectively. Similarly, the vertical and horizontal components of the shear edge wave are u_{xt} and u_{yt} . The polarities indicated by the arrows representing the

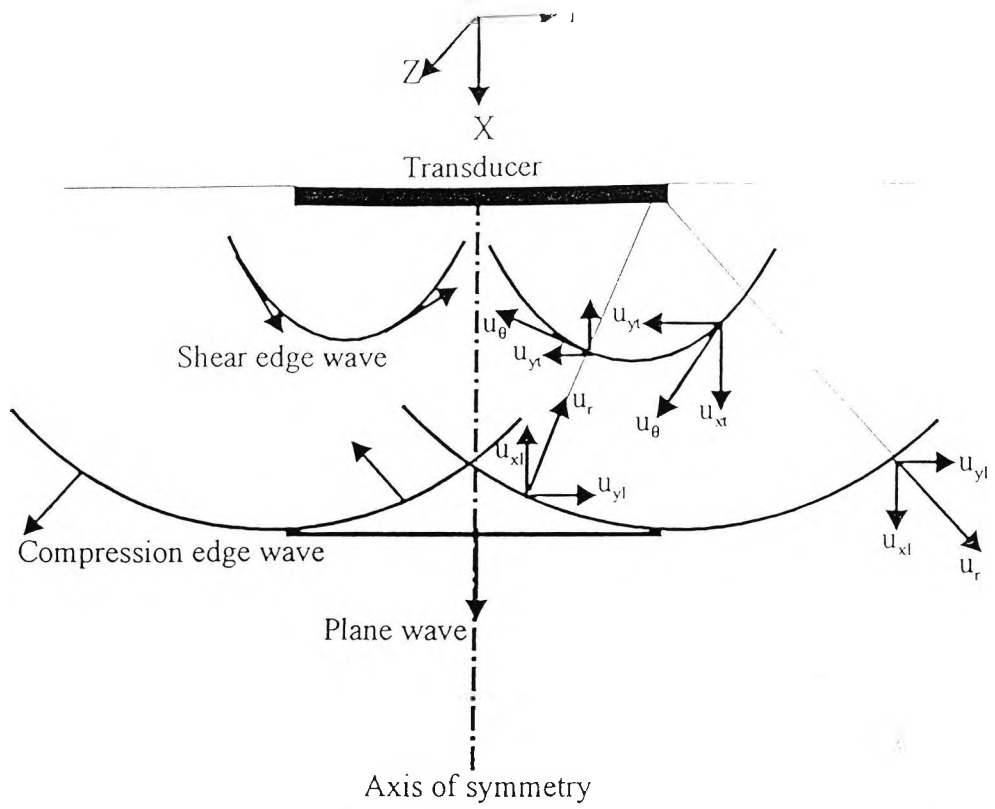


Figure 2.2.1: The wavefront of the plane and edge waves with their relative polarities radiated from a circular source coupled to a solid, Weight (1987).

vector particle velocities are those predicted by scalar impulse response theory and their direction is given by the plane and edge wave structure of the wave fronts radiated. With θ and β as defined in Figure 2.1.1 and 2.2.1, then (Weight, 1987)

$$u_{xl} = u_t \sin\theta, \quad (17)$$

$$u_{yt} = -u_t \cos\theta \cos\beta, \quad (18)$$

$$u_{xt} = u_t \cos\theta, \quad (19)$$

$$u_{yt} = u_t \sin\theta \sin\beta. \quad (20)$$

By assuming that the edge waves may be considered locally plane, the amplitudes of the compression and shear particle velocities are given by, respectively,

$$u_l = e_l / \rho c_l, \quad (21)$$

$$u_t = e_t / \rho c_t, \quad (22)$$

where e_c and e_s are the compression and shear-edge wave impulse responses given in Eqs (15) and (16).

Using Eqs (17) and (19), the normal component of the particle velocity impulse response becomes

$$u_{x\delta} = \delta(t - \tau_0) - m_l(\theta)f_l(t - t_l)\sin\theta - m_t(\theta)f_t(t - t_l)\cos\theta, \quad (23)$$

From which the particle velocity response for an arbitrary source velocity motion becomes

$$u_x = v(t) * u_{x\delta}, \quad (24)$$

where $v(t)$ is the velocity function of the transducer.

2.2.4 Impulse responses and particle velocity waveforms

A graphical representation of Eq (24) will give a clearer picture to the reader about the nature of sound propagation in a solid. This representation is seen in Figure 2.2.2 which shows on-axis calculated impulse responses and waveforms for short ultrasonic pulses propagating from a 19mm diameter, 5MHz transducer into a solid medium. These waveforms and the way in which they vary with range can be explained in terms of the contributions of the compression plane and edge waves together with a mode converted shear edge wave.

The waveform starts with a contribution due to arrival of the locally plane wave (P) which retains its shape and amplitude at all points within the geometric region straight ahead of the source. The plane wave pulse is followed by the compression edge wave pulse (E_c). Since for a point on axis the edge contributions from each element of the source rim arrive simultaneously, there is then just one edge-wave

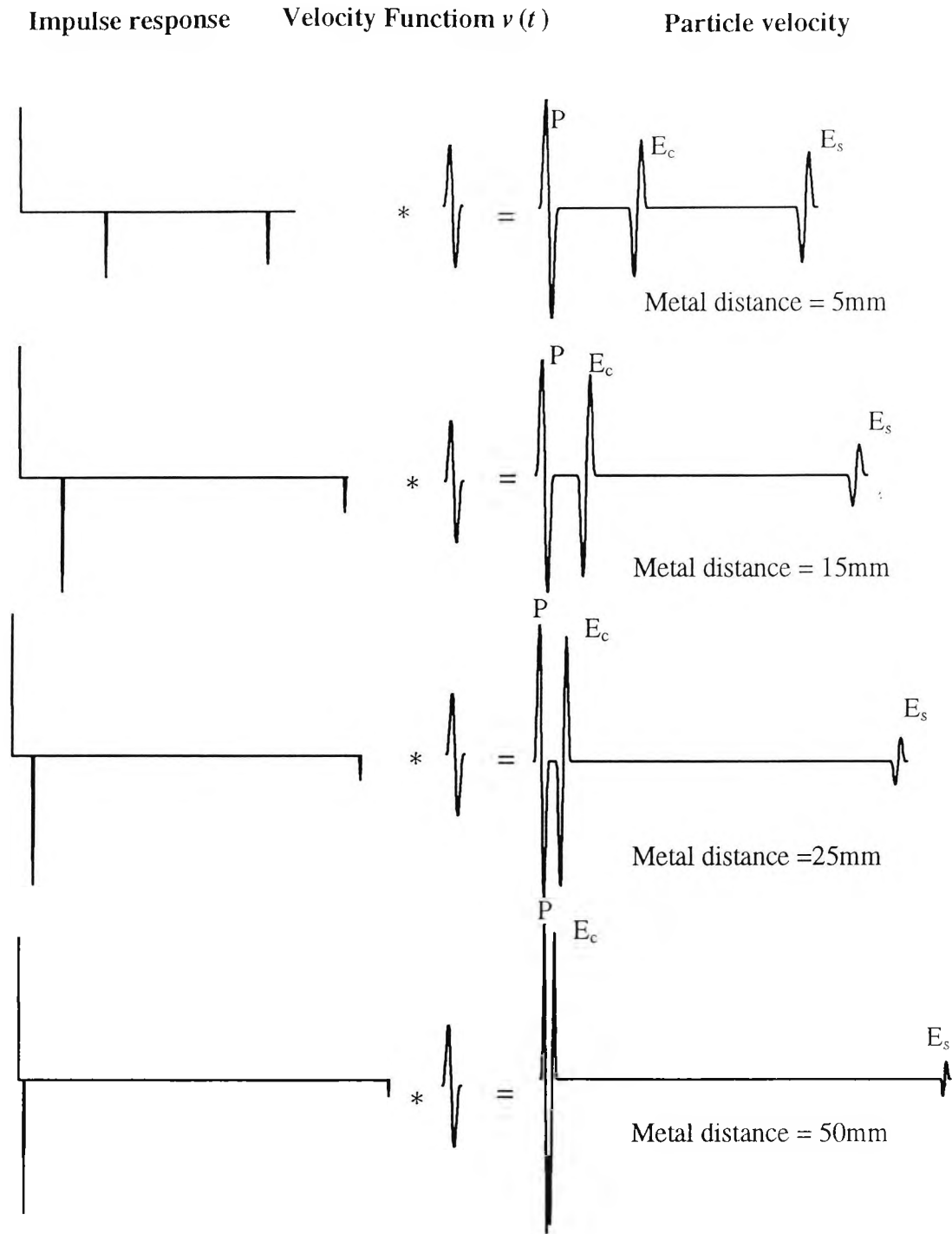


Figure 2.2.2: Impulse responses and particle velocity waveforms of sound propagating in an ideal solid medium at different axial ranges assuming a 19mm diameter source excited with a 5MHz short pulse. P denotes the compression-plane wave pulse, E_c denotes the compression-edge wave, and E_s denotes the shear-edge wave pulse.* denotes convolution

pulse. As described in section 2.1, this pulse has opposite polarity to that of the plane wave pulse (propagation of sound in fluid). In a similar fashion, there is a single shear edge wave pulse (E_s) at an axial point and as expected this arrives after the compression edge wave. At short ranges the angle subtended at the source rim is such that strong mode conversion of the incident compression edge wave occurs, as shown in the examples in section 2.2.2. Further away, the mode conversion effect is less strong. Note also that the separation between the compression plane and edge wave components becomes less with axial range and with increasing range they will eventually overlap. However, since the shear wave travels at approximately half the compression-wave velocity, the shear-wave pulse becomes further separated from the compression pulses and its amplitude becomes smaller than that of the compression edge-wave pulse as the mode conversion becomes weaker.

As shown in Figure 2.2.3, for points off the axis of the source, the plane wave pulse is the same as that in the on-axis results, but each of the edge wave contributions (E_c and E_s) are now smaller and smeared out in time. However, two main contributions to the smeared edge wave pulse can be seen, one from the nearer edge of the source, the other from the further edge.

Weight (1987) verified the predictions of the model by comparing its results with experimental measurements of field point waveforms at points on the surface of a solid.

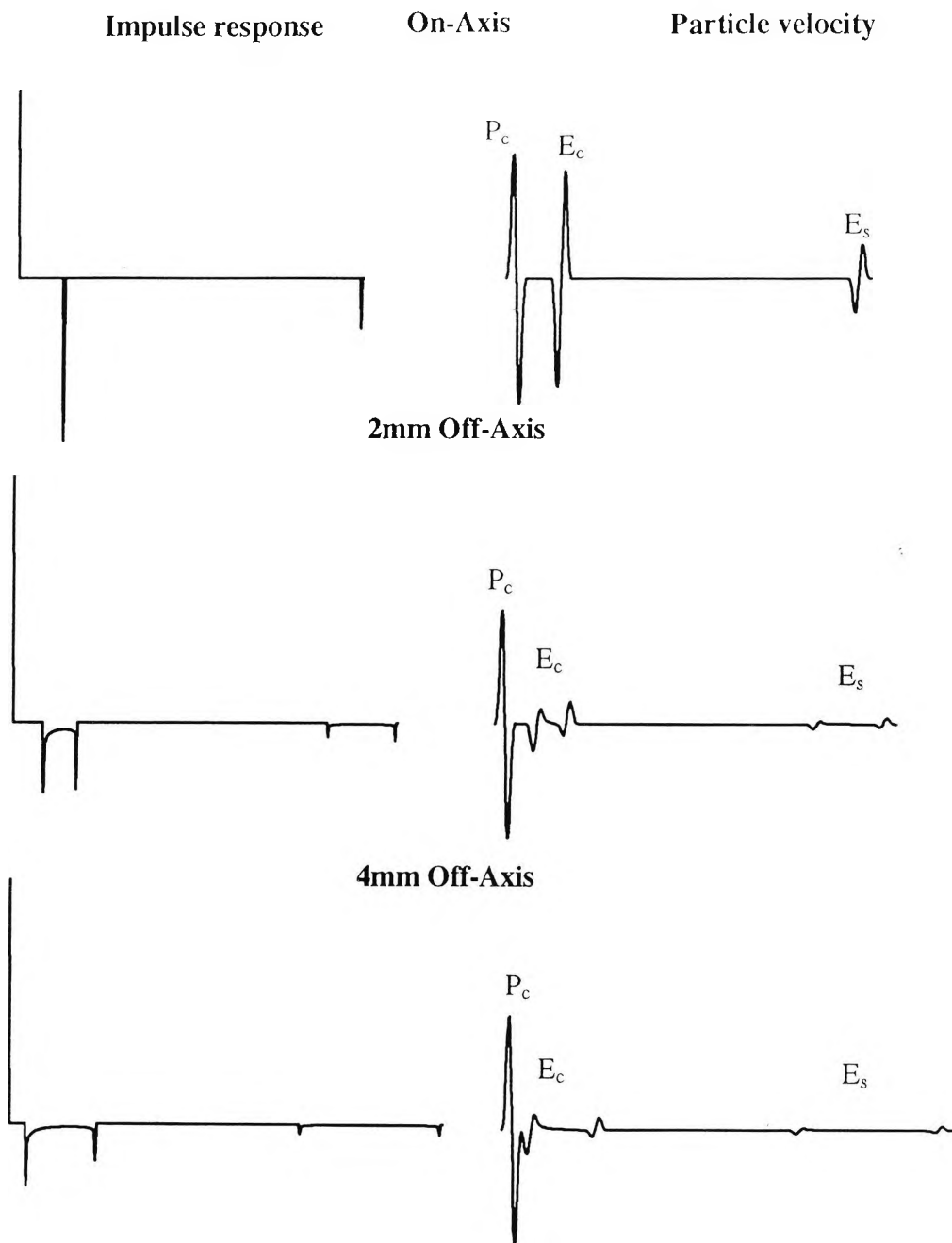


Figure 2.2.3: Impulse and particle velocity waveforms for axial and non-axial points in a solid. The source parameters are as mentioned in Figure 2.2.2

2.2.5 Pulse echo waveforms for a point-like target in a solid

In a solid medium, scattering of the incident plane and edge waves gives rise to a multipulse echo response even more complicated than of a similar target in a fluid (Weight, 1993). Such complications stem from the existence of shear edge waves and the probability of mode conversion at the target. For the case of a target in a solid, the approach adopted here is similar to the approach reviewed in section (2.1.1) for a fluid medium, but takes into account the extra complications of the compression and shear components of the interrogating beam and the behaviour of the transducer when acting as a directly coupled receiver.

Following Weight's approach (1993) the target is considered to be a point-like free boundary in the solid. Using the same geometrical variables as defined in figure (2.1) the motion v_r of the target is equal to the normal component of the particle velocity of the incoming waves. Thus, for impulsive motion of a transducer directly coupled to the surface of a solid, v_r is

$$v_r = -u_{x\delta} \quad (25)$$

where as above $u_{x\delta}$ is the normal component of the radiated particle velocity u_δ (r,t). The minus sign in equation 25 comes as a result of making the simplifying assumption that the incident wave is locally plane and that the target has a reflection coefficient of -1. This assumption is valid since the difference in acoustic impedance between air and a solid medium is sufficiently great.

Consider now the behaviour of the transducer in reception. Since a finite transducer may be represented as a collection of point receivers, it may be considered that a directly coupled transducer is uniformly sensitive to the normal components of the particle velocity of the incoming waves (Weight, 1993).

As a result, for the case of a target in a solid medium, the normalised particle velocity impulse response is given as

$$E_{\delta s}(t) = u_{x\delta}(r, t) * u_{x\delta}(r, t), \quad (26)$$

and the echo response for arbitrary excitation of the transducer is then

$$E_s(t) = v(t) * E_{\delta s}(t). \quad (27)$$

From Eq (27), it is clearly seen that the waveform from a small target in a solid is obtained by a double convolution. This means that waveforms produced by Eq (27) are considerably different from those at points in the radiated field, there being further time-separated components - as discussed below.

Before going into more details about the nature of these echo responses it is appropriate to define 'the path difference (PD)' as used extensively in this thesis. As mentioned earlier, the plane wave travels from the face of the source to reach a certain point in the field. The edge waves travel from the source edge to reach the same point. The difference in the distance travelled by both is defined as 'path difference' or PD. For axial points, the term is defined by

$$PD = \sqrt{R^2 + x^2} - x. \quad (28)$$

where R is the transducer radius and x is the distance from the centre of the transducer to the (axial) field point. This term has considerable importance in the present work, since many of the results shown later greatly depend on the path difference between the plane and edge wave components.

It should be mentioned that for a multi-cycle pulse and at an axial point, when the PD between plane and edge waves is $n\lambda$ (wave length) destructive interference between these waves takes place when they overlap. In this thesis such range is

defined as "Destructive interference range". When the axial PD is $(2n + 1)\lambda / 2$, the overlapping portion of the plane and edge waves interfere constructively. This range is defined as "Constructive interference range".

Computed impulse responses and transmit-receive mode responses, for point-like axial targets at various ranges in a solid are shown in Figure 2.2.4. These exhibit a more complicated structure than the corresponding particle velocity waveforms shown in Figure 2.2.2. The form of these responses has already been described in previous work (Weight, 1993), but briefly, for an axial target, the echo impulse response consists of a series of six pulses. At short ranges, the various plane and edge wave components are well separated. As the target range increases, the PD between compression plane and edge waves decreases. As a result, the first three pulses become closer together, to form a group well separated from the 4th and 5th pulses, which also move towards one another to form a second group. The separation between the second group and the 6th pulse also increases. Further details of the origin and phase relationships of each component is given in the next section.

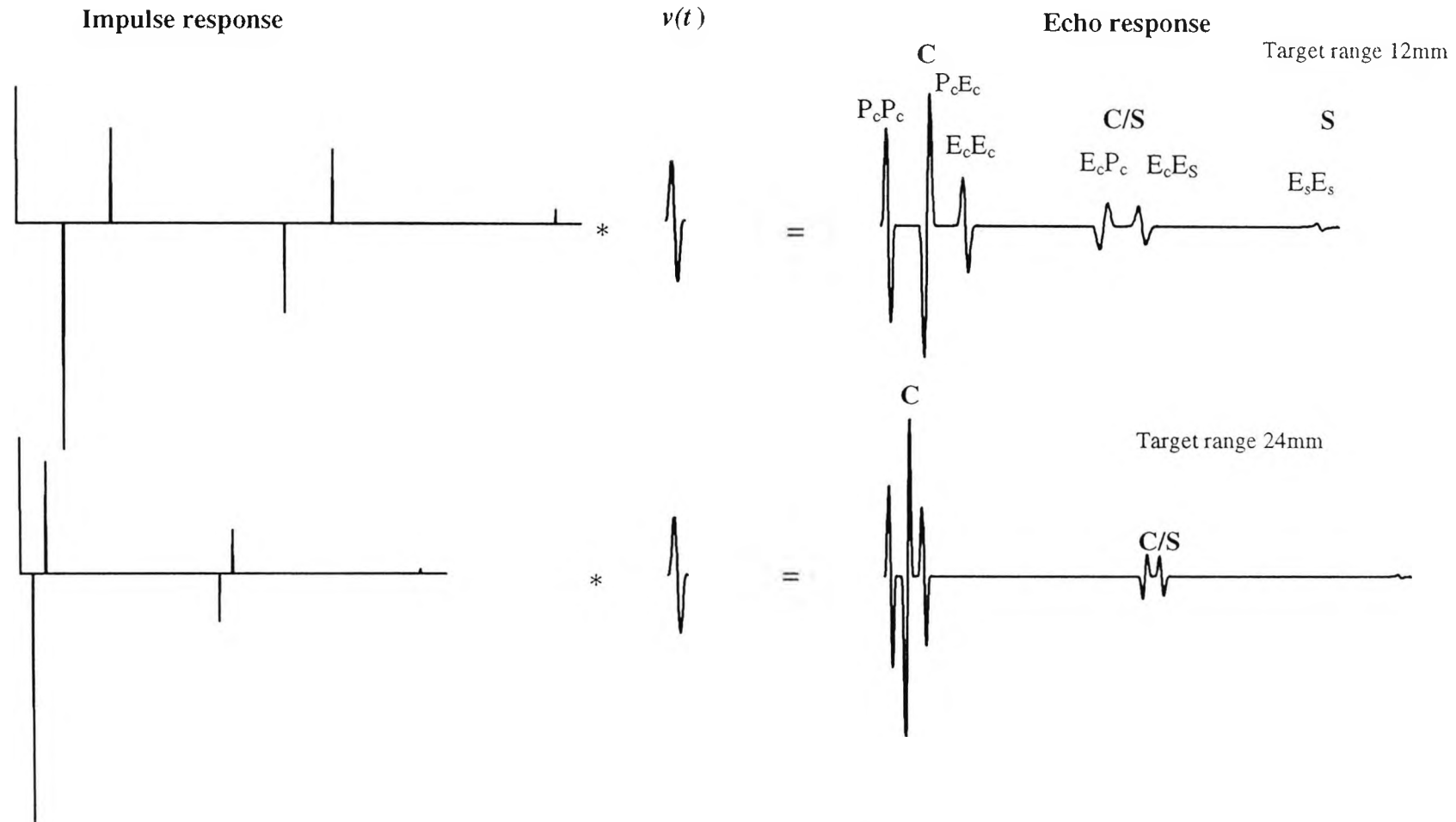


Figure 2.2.4: Calculated impulse responses and echo responses for small target at different ranges assuming a 19mm diameter transducer excited with 5MHz single-cycle pulse. The symbols shown at the top right of the figure are explained in the text.

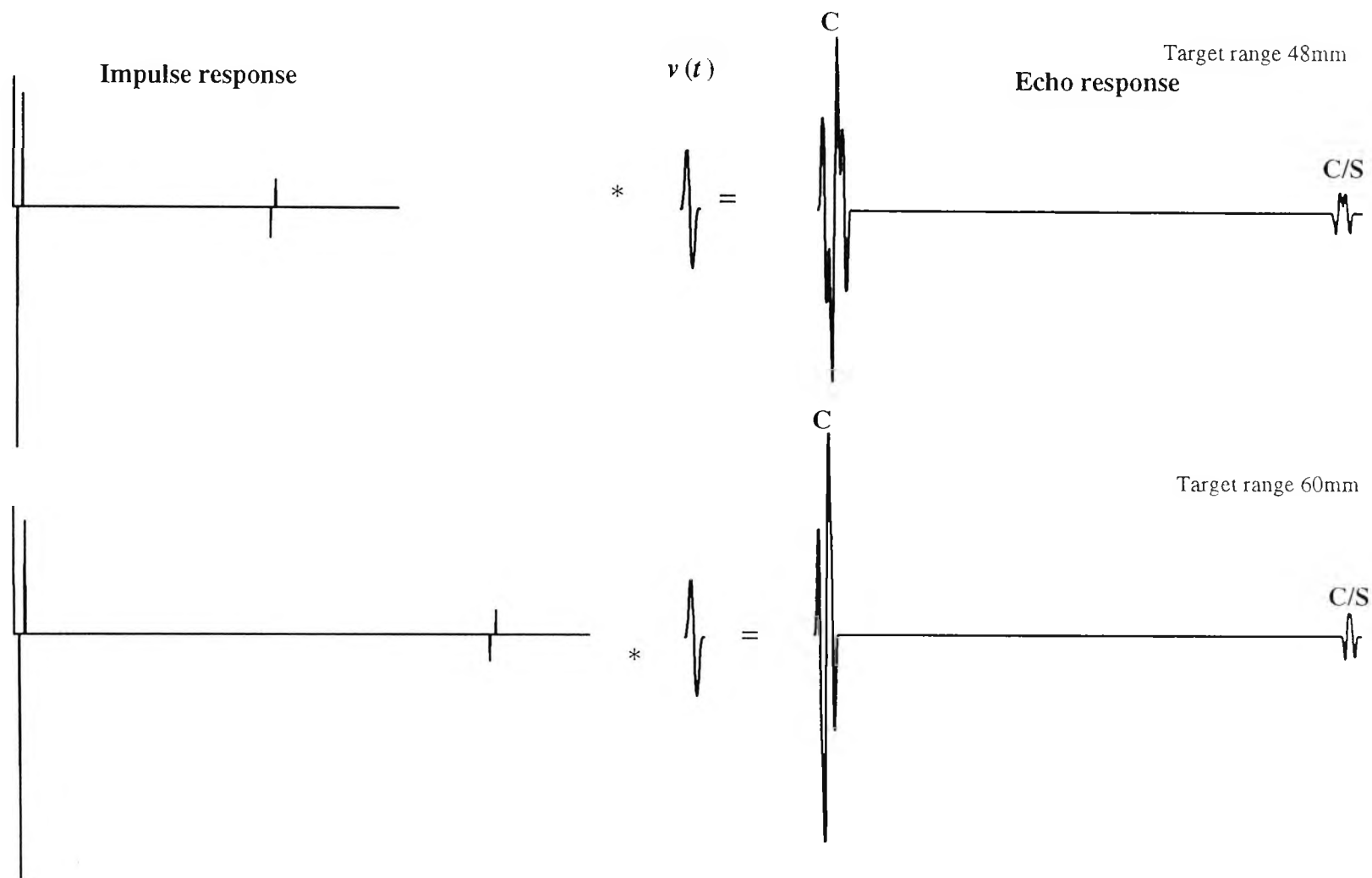


Figure 2.2.4: continued, the S component is not shown in the responses at these two ranges since it is very small.

2.2.6 Physical explanation of the form of echo responses

The definition of each pulse shown in Figure 2.2.4 is based on their physical origin (Weight, 1993). They are arranged according to their arrival time as shown in Table 2.2.1. There are many components that go to form the overall echo response and for convenience each of these is given a separate identity using lower case letters (the "echo component" column in Table 2.2.1, p 28). Some of these components overlap to give overall responses that for circular sources and point-like axial targets consist of six pulses (the "echo pulse" column in capitals in Table 2.2.1). The first component, $p_c p_c$, arises from the scattering of the original compression plane wave that returns as a spreading compression wave to be received paraxially at the centre of the transducer. This is the sole component within the first pulse and hence the corresponding echo pulse is labelled $P_c P_c$. In contrast, the second pulse $P_c E_c$ is comprised of two components that each take a different propagation path, but are received at the same time. Component $p_c e_c$ arises from the scattering of the incident compression plane wave as it is simultaneously received by each element of the source rim. Whereas, component $e_c p_c$ arises as the scattering of the incident compression edge wave reaches the centre of the source. Note that the phase relationships of these various components have been explained in detail in earlier work (Weight and Hayman, 1978, Weight, 1993) but briefly, a locally spherical wave propagating from an axial scatterer to be received at the source centre will give rise to a pulse of opposite polarity to that of the later arriving pulse generated when the wave is received at the source rim. However, since as shown above in Figure 2.1.2 (p 7), the outgoing plane wave has opposite polarity to the edge wave radiated into the geometric region straight ahead of the source, the final result is that the $p_c e_c$ and $e_c p_c$ components have the *same* polarity. Since as a result of circular symmetry they are received at the same time, they reinforce to give an increased amplitude pulse (the second echo pulse labelled $P_c E_c$ in Table 2.2.). The fourth component $e_c e_c$ arises when scattering of the outgoing edge compression wave is received at the edge of the source. Since this is the sole contribution to the third pulse this is labelled pulse $E_c E_c$.

Note that this latter pulse has the same polarity as the first pulse. Since the first three pulses arise from waves that propagate both to and from the target at the compression wave velocity, it is convenient to refer to them as a group labelled 'C', as is also done in Figure 2.2.4.

In similar fashion to that described above for compression waves, there will be a number of components arising from waves propagating either to or from the target as shear waves. The fifth component $p_c e_s$ in Table 2.2.1 is due to reception of the scattering of the outgoing compression plane wave that returns as a shear wave to be received at the source rim. Note that there will be no pulse produced when this latter scattering first reaches the plane of the source, since on reception the source responds to the normal component of the particle velocity. For an axial target, there will be no component in the normal direction when the shear wave scattering it produces is received at the source centre (Weight 1993). The sixth component $e_s p_c$ arises from an outgoing shear edge wave that returns to the transducer centre as a compression wave. Again, the arrival time of these two components is the same and just as with the second and third components they have the same polarity. They therefore superimpose to give the fourth echo pulse (labelled $P_c E_s$) in the overall response. The seventh and the eighth components also have the same total propagation time. The $e_c e_s$ component travels from the rim of the source at the compression wave velocity but back to the rim at the shear wave velocity. Whereas the $e_s e_c$ component travels from the rim at the shear wave velocity but back at the compression wave velocity. Again these components add to give the fifth pulse $E_s E_c$ in the echo response. Also, note that the $P_c E_s$ and the $E_s E_c$ pulses have opposite polarities. Since the fourth and fifth pulses in the response arise from waves that travel with the compression wave velocity and back with the shear wave velocity or vice versa, they are denoted as the 'C/S' group. As can be seen in Figure 2.2.4, this group becomes increasingly separated from the "C" group as the target range increases.

The final, ninth component $e_s e_s$ travels from and to the source rim as a shear wave. Again, since this is the sole contribution to the final pulse in the overall

response, it is labelled pulse $E_s E_s$ in Table 2.2.1 and this is the only pulse in the final "group" denoted 'S'. Again, as the target range increases, this pulse becomes increasingly separated from the "C" and "C/S" groups (see Figure 2.2.4).

The form of the above calculated results has been experimentally verified elsewhere (Weight, 1993). Further confirmation showing results appropriate for the current work are given later in section 4.2.

Echo component	No	Echo pulse	No	Echo group	Incident wave	Received at source:	Scattered wave
$p_c p_c$	1	$P_c P_c$	1	C	plane compression	Centre	compression
$p_c e_c$	2	$P_c E_c$	2		plane compression	Rim	compression
$e_c p_c$	3				edge compression	Centre	compression
$e_c e_c$	4	$E_c E_c$	3		edge compression	Rim	compression
$p_c e_s$	5	$P_c E_s$	4	C/S	plane compression	Rim	shear
$e_s p_c$	6				edge shear	Centre	compression
$e_c e_s$	7	$E_c E_s$	5		edge compression	Rim	shear
$e_s e_c$	8				edge shear	Rim	compression
$e_s e_s$	9	$E_s E_s$	6	S	edge shear	Rim	shear

Table 2.2.1: Labelling system to identify the various components in the overall echo response of small targets as given in Figure 2.2.4. (after Weight, 1993).

So far, this section has dealt with echo responses from axial point-like targets at various ranges. It is now helpful to consider what happens when targets lie off axis. As will be seen later, this will aid in describing the form of echo responses from finite sized targets. Figure 2.2.5 shows responses for a point-like target, on and off axis at a range of 12mm. Since all of the targets are within the geometrical region, each will give rise to scattering of the incident plane wave and this will be first received when the scattering first returns to the plane of the source. Therefore the first component of the echo response will have exactly the same form whether or not the target is on axis. However, with off-axis targets, all the later arriving components arise either from the scattering of edge waves or from the rim reception of the scattered plane wave. On reception, such components are smeared

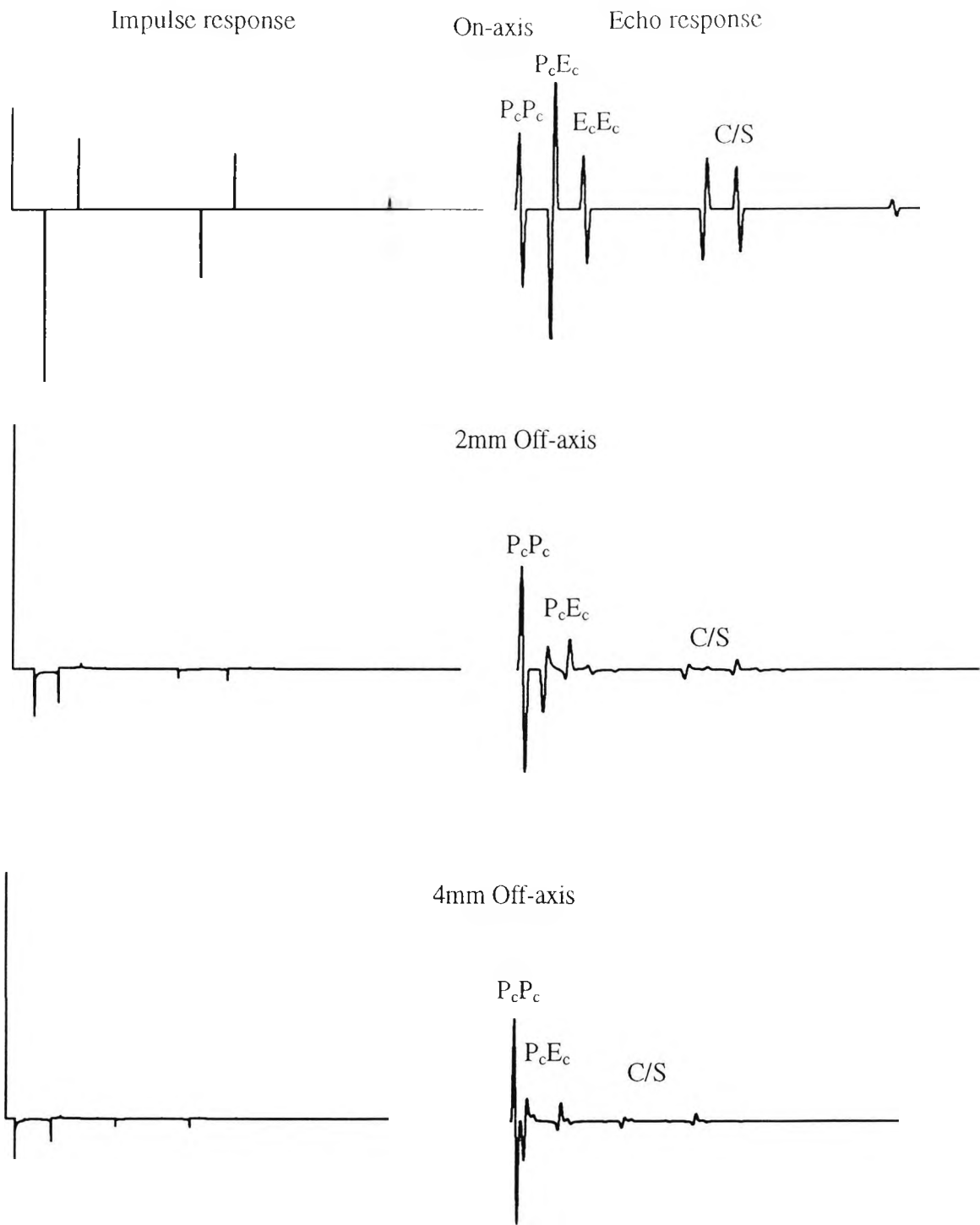


Figure 2.2.5: calculated Impulse and echo response for small target on and off-axis at 12mm range assuming the source parameters mentioned in Figure 2.2.4.

out in time, since the propagation paths from each element of the source rim to the target and back are not equal.

2.2.7 Echo responses of finite sized targets in a solid

There have been several approaches used to predict the echo response of planar finite sized targets in a solid medium. These approaches assume that the medium of propagation is isotropic and lossless and that the target is interrogated by waves emanating from a circular compressional wave transducer.

However, some of these approaches assume that the target is in the far field of the transducer and is interrogated by plane waves only. For example, Chapman (1988), used the geometrical theory of diffraction (GTD) to predict echo responses for planar targets in isotropic lossless solids. But this was only valid if all the dimensions of the problem are much greater than the pulse wave length.

Another approach adopted by Ogilivy (1991) was the use of Kirchhoff theory. Using this theory the target needs to be at least three pulse wavelengths in extent to give reliable predictions. However, real piezoelectric ultrasonic transducers used in NDT, have been shown to produce more complicated pulses, as mentioned in sections 2.2.5 and 2.2.6. Diffraction effects and mode conversion generate significant compression and shear edge waves and these go on to scatter and produce significant extra signals in many practical situations. Also, the target in many cases can be in the near field of the transducer. Hence, the above assumptions can neither explain such signals nor deal with situations in which they arise.

By using the finite difference method, a more accurate approach to model the echo response of targets in solid has been developed by Stacey and Weight, (1993). This approach provides a relatively straightforward way of modelling the formation of echo responses from scattering defects and readily incorporates realistic transducer

signals. However, one disadvantage of this work is the length of computer time needed.

Recently, Lhemery (1995) proposed a model to predict the echo response from a defect of complex geometry at arbitrary position in a solid medium in the field of an arbitrary transducer. His model treated scattering by the defect under the Kirchhoff approximation, assuming homogeneous, free boundary conditions. He illustrated the applicability of his model by treating the case of flat-bottomed holes.

Krstelj and Markucic (1997), introduced a different approach of the mathematical modelling of the disc reflector response. Their choice of the mathematical function which represents the echo response is based on trial and error, depending on the experimental data obtained. The fitting parameters of the function are then estimated and optimised using numerical and statistical procedures, respectively.

L. Wang, J. Deng and J. Shen (1997), combined the time-domain boundary element method with electro-mechanical reciprocity relation to give an accurate model for the ultrasonic echo pulse. Good agreement between the measured echo response of a 5mm-diameter void in a solid and its simulated response was obtained. Although their model was accurate, its main disadvantage is the computing time required.

A rapid method for predicting the echo response of finite sized targets can be implemented by extending the model mentioned in section 2.2.5. However, the extension is valid only for axisymmetric circular targets.

As might be anticipated if only the front surface scatterer is considered, the echo waveform from the surface of a finite sized target can be thought of as the sum of the contributions from all the elementary point targets that make its surface (McLaren and Weight, 1987). As a result, the impulse particle velocity response for a finite sized target can be represented as:

$$E_{\delta s}(t) = \iint_{\sigma} u_{x\delta} * u_{x\delta} d\sigma \quad (29)$$

where σ is the surface area of the target.

As a result of the circular symmetry of the radiated field from a circular source, the particle velocity impulse response at all points on a circular arc on the scattering surface that are equidistant from the source centre are identical. The surface integral in Eq (29) may therefore be transformed into a line integral by treating the surface of the target as a sum of elemental circular rings of area $d\sigma$, all points on the circular segments being equidistant from the transducer centre. For axial circular targets these equidistant ring segments are complete and $d\sigma$, Figure 2.2.6, is then

$$d\sigma = 2\pi y dy \quad (30)$$

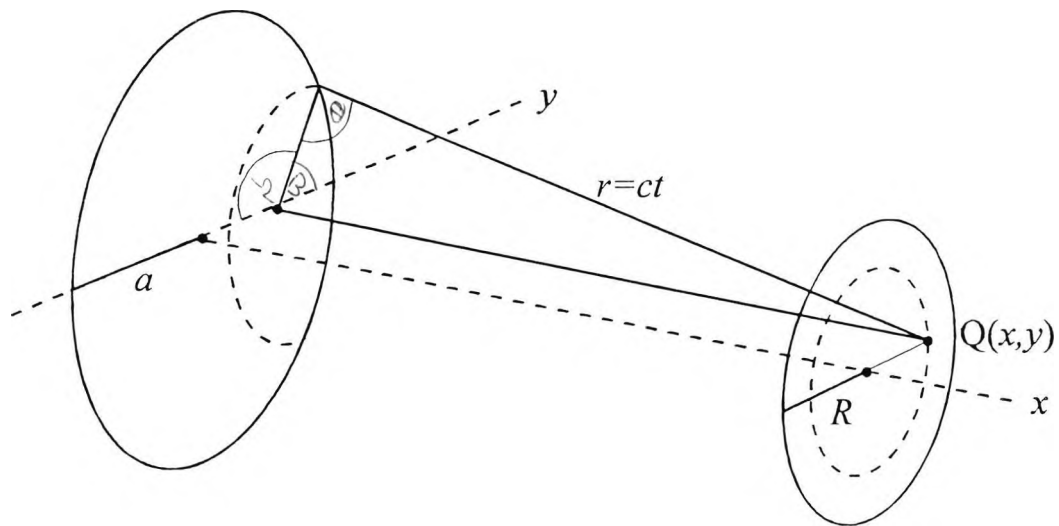


Figure 2.2.6: As in Figure 2.1.1, but the ultrasonic beam is interrogating a circular target of radius R .

where y is the distance off axis. The particle velocity impulse response now becomes

$$E_{\delta s}(t) = \int_0^R u_{x\delta} * u_{x\delta} 2\pi y dy \quad (31)$$

where R is the target radius. The echo response is

$$E_s(t) = -k_s v(t) * \int_0^R u_{x\delta} * u_{x\delta} 2\pi y dy \quad (32)$$

For circular targets of different size, but with identical acoustic properties, relative echo amplitudes are determined by the integral within Eq (32).

Although the integral in Eq (32) is derived from the work of McLaren and Weight (1987) for targets in a fluid medium, the present formulation for $u_{x\delta}$ calculates an echo response for finite targets in a solid in terms of particle velocities and not pressure.

It should be mentioned here that in deriving Eq (32) a number of assumptions were made. Firstly, the head and surface waves were ignored. The justification for neglecting them is that the Rayleigh waves are confined near to the surface of the solid and since most uses of ultrasonic transducers involve the interaction of the radiated field with subsurface reflectors many wavelengths into the solid, such Rayleigh wave contributions are not significant. Also the head waves have a limited region of influence. Schmerr and Sedov (1989) showed that these waves are absent beyond the region of $1.73R$, where R is the probe radius, into the solid. For example if the probe radius was 9.5mm then the head waves will be absent beyond about 16mm into the solid.

Secondly, it is assumed that the target surface moves with the normal component of any non-normal incident waves such as edge waves. This is a major simplification which is only likely to be reasonably valid for small angles of incidence. Thirdly, on reception the transducer is assumed to respond to the normal component of the incoming particle velocity waveform. Finally, the medium of propagation is assumed to be isotropic and lossless.

The model used in the present work has the advantage that it can predict echo responses more rapidly than the finite difference method mentioned above. Although less accurate than the finite difference method, the new model has an accuracy adequate for many practical applications and gives great insight into the formation of echo responses.

Detailed results using the new model are given later in Chapter 4 but as an aid to demonstrate the way in which the echo impulse response varies with target size some preliminary results are given here in Figure 2.2.7. These results are for various diameter FBH's at a range (12mm) where the variation in echo impulse response with target size is clearly seen. As can be seen in Figure 2.2.7, the first arriving plane wave component comes to dominate the response as target size increases. This is because the edge wave components are smeared out with time as the integration of Eq (31) proceeds, whereas the first received plane wave contribution is not.

Figures 2.2.7 and 2.2.4 show that in general, the C/S and the S components are smaller than those within the C group. As will be discussed later in Section 4.4, this will be of relevance when estimating pulse amplitudes, especially when considering the variation of echo amplitude with range where there will be opportunities to reduce calculation times.

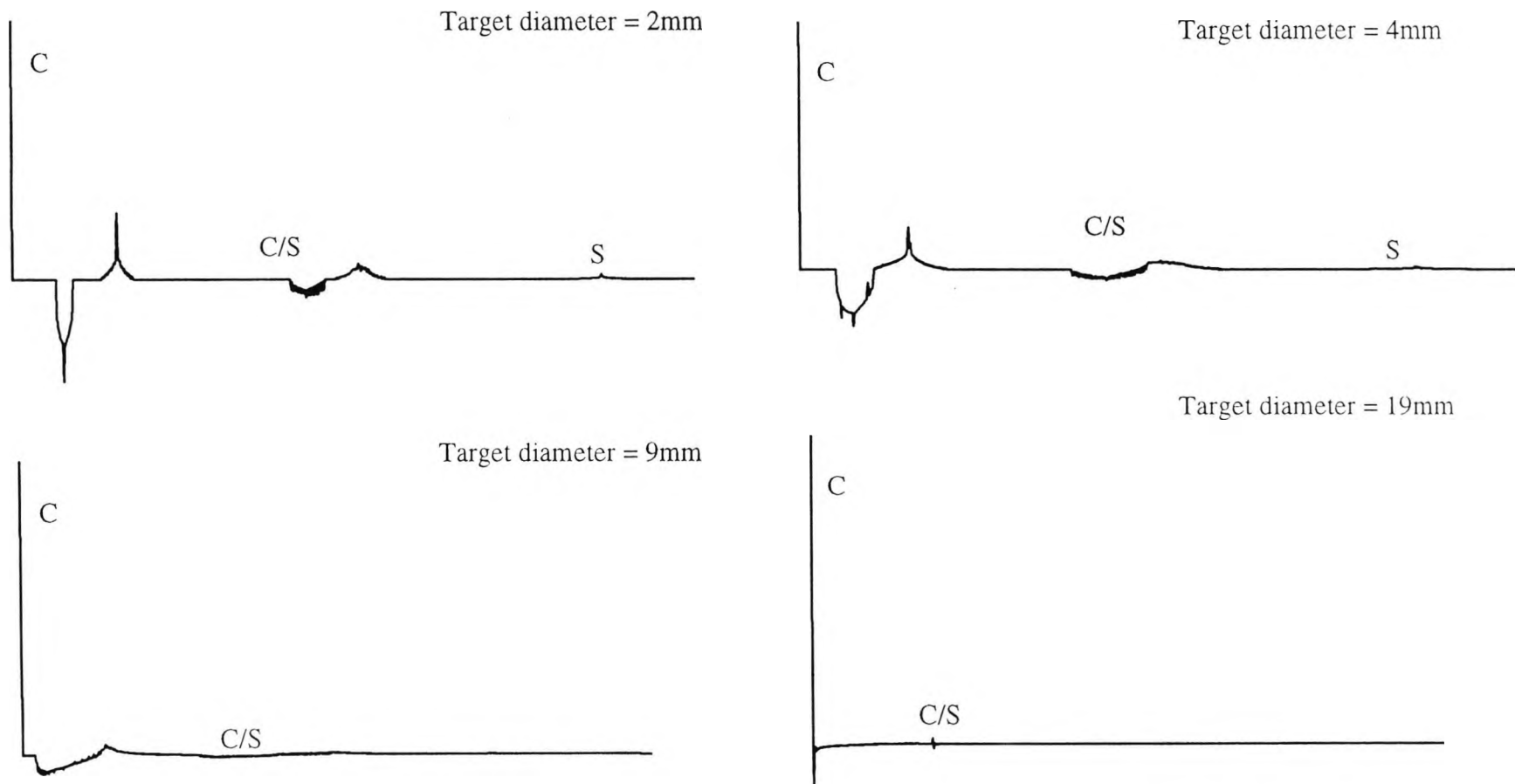


Figure 2.2.7: Impulse responses for various target sizes at 12mm range from a 19mm diameter transducer calculated using the finite-sized target model. The graphs were scaled to show the edge wave components. The S components in the impulse responses of the 9 and 19mm diameter targets are too small to be shown in the figure.

2.3 DGS diagrams

So far we have been looking into the modelling of echo responses for flat-bottomed holes in a lossless isotropic solid medium. It is well known that the target size and its distance from the probe play a big role in determining its echo amplitude. The relationships between echo height, distance and size of a circular disk defect were brought into simple and universally applicable forms by Krautkramer (1959) in a set of curves known as Distance Gain Size (DGS) diagrams.

In deriving his curves, Krautkramer (1959) first considered the sound pressure p at points along the axis of a circular source excited with continuous sinewaves, i.e.

$$p = 2p_0 \sin [\pi/\lambda \{(D_s^2/4 + x^2)^{0.5} - x\}], \quad (33)$$

where λ is the wavelength, D_s is the diameter of the transducer and x is the distance along the axis. p_0 is taken to be the average pressure immediately in front of the probe, when the crystal is much larger than the wave length.

For a large distance x compared with the diameter D_s and with the near field length of the probe, N , where $N = D_s^2 / 4\lambda$, Eq (33) becomes

$$p = p_0 \pi (D_s^2 / 4\lambda x). \quad (34)$$

If $A = x/N$, where A is the normalised distance,

$$p \sim p_0 \pi / A. \quad (35)$$

A very large flat defect or a flat back wall will reflect the beam like a mirror and the transducer then acts as a receiver to its own beam at twice the back wall

distance. The probe will then measure uniform sound pressure over the whole of its surface.

$$p_{backwall} = p_0 \pi / 2A \quad (36)$$

If a small, circular disc is placed in the axis of the beam at so great a distance that the sound pressure $p_0 \pi / A$ is uniform over its surface, then this may be regarded as the initial pressure of a new radiator, which radiates a similar wave back to the probe. The probe itself will therefore measure the echo as:

$$p_{defect} = (p_0 \pi / A) (\pi N_r / x) \quad (37)$$

where $N_r = D_r^2 / 4\lambda$ is the near field of the reflector, the diameter of which is D_r . If the defect size is measured in terms of the diameter of the probe one obtains the 'reduced defect size' G where $G = D_r / D_s$ and equation (37) can be simplified to:

$$p_{defect} = p_0 \pi^2 (G^2 / A^2) \quad (38)$$

The average pressure p_0 can be taken as the back wall echo of a plate which is of thickness less than that of the near field of the transducer.

Eqs (36) and (38) express the facts that for sufficiently large distance from the transducer, the back wall echo amplitude decreases inversely with the distance and the defect echo amplitude is proportional to the target area and inversely proportional to target range. A graphical representation of Eq (38) is shown in Figure 2.3.1.

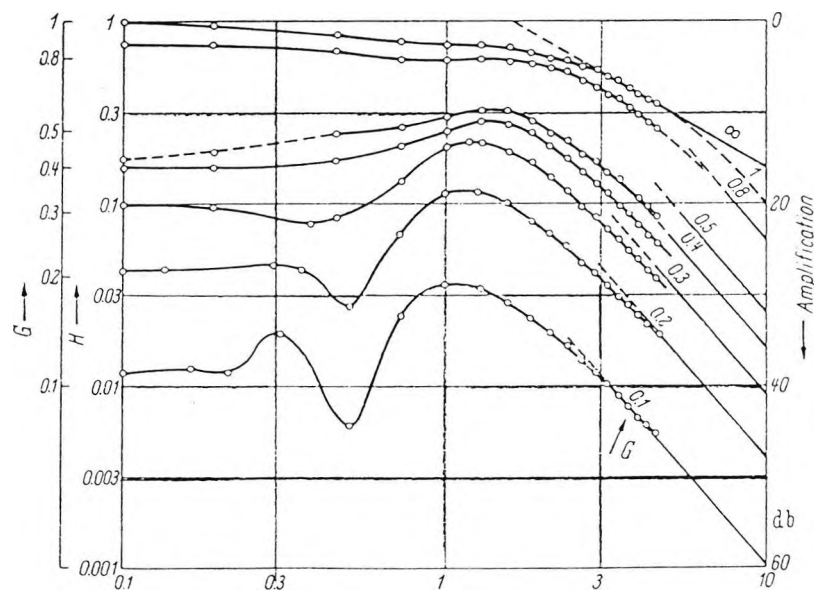
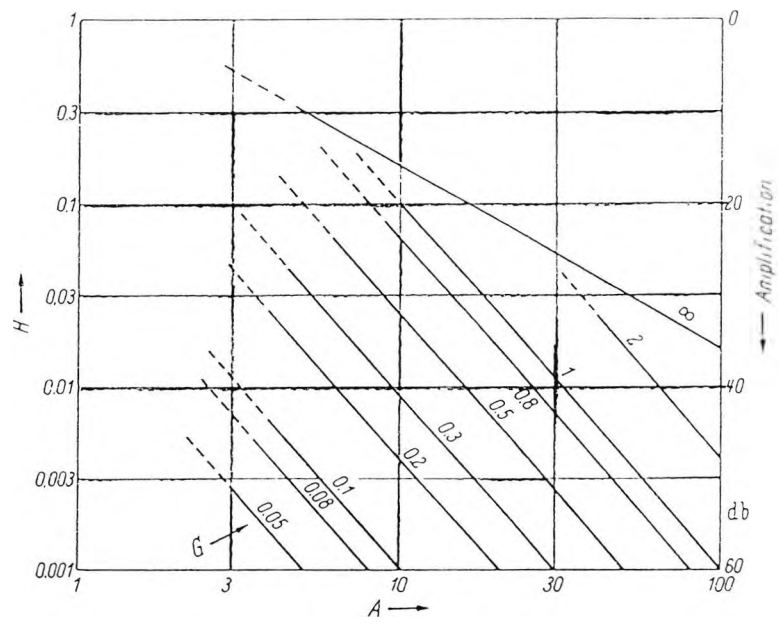


Figure 2.3.1 : DGS curves produced theoretically by Krautkramer (top) and the rest of the curves completed experimentally (bottom).

Eq (38) has several limitations that have been mentioned by Krautkramer. For example, it is only applied to the far field, it assumes a fluid medium of propagation, and is valid as long as the wavelength is not larger than the diameter of either the probe or the defect. This equation was used by Krautkramer to give the far-field portion of his DGS diagrams.

Because of such limitations, many studies published were not in favour of this method. For example, Bastien (1968), Bradfield (1968), Whittaker (1972) and Mundry (1972) claimed the impracticality of such curves in pulse ultrasonic flaw detection due to practical problems, like the influences of the probe and the shape of defects. They suggested that more studies were needed to improve the general understanding of the behaviour of sound in the material.

In contrast, Hislop (1969) showed that, if the probe was chosen so that targets were positioned in the far field of the transducer, results given by the DGS diagrams agreed well with actual target size. He did this by immersing the transducer in a water tank and made sure that the echo was detected in a water bath which placed the target in the far field of the transducer. He also showed that targets can be positioned in the far field easily in direct contact testing by changing the probe i.e. smaller diameter probe. This however has some limitations in practical NDT. For example, in the far field there is beam spreading. Also, a smaller diameter probe limits the ratio of the target size to that of the probe. His results were most satisfactory in the region of 1.5-3 NF distances.

McNab (1977) said that the DGS diagrams and reference block methods had the advantage that they give a reproducible absolute reference against which to judge flaw size. But they do not take into account variation in flaw characteristics, such as shape, reflectivity and roughness. Therefore it is not possible to derive actual flaw size from these diagrams except where the reflector is the same as that used for reference.

Some publications dealt with producing DGS diagrams using shear wave probes (Certo, 1984) and they recommended this method to be used for defect sizing. More details regarding using this method for shear wave probes are explained in the above article.

Following the development of the impulse response method to model the propagation of ultrasound in fluids, McLaren and Weight (1987) developed full theoretical DGS diagrams for disc-like targets in a fluid, using an impulse response method to predict the echo response of finite targets in a fluid medium. Their diagrams compared very well with the diagrams produced by Krautkramer in the near field as well as in the far field.

Schmerr and Sedov (1989), developed a model that predicts the pulse echo responses from a flat-bottomed hole whose axis is aligned with the axis of the compressional wave transducer (axial targets). In their model, they used the Schoch solution (R/λ is much larger than 1, where R is transducer radius) for the waves incident on the hole bottom, the Kirchoff approximation at the hole (the wave length should be larger than the target) and a high frequency asymptotic approximation to obtain an approximate analytical expression for the measured response. However, in their model they neglected the shear waves, i.e. they replaced the elastic solid by an equivalent fluid. This assumption came as a result of their work on developing an elastodynamic model for propagation of ultrasound in a solid, in which they argued that the effect of shear waves is very small (Schmerr and Sedov, 1989). The scattered waves received back at the transducer were obtained via a combination of exact integrations and the method of stationary phase. From this model, they produced DGS-like diagrams that can predict the significant response variation in both the near and far fields of the probe.

Sumbatyan (1989) described the development and numerical implementation of a calculation method for DGS diagrams for a flat-bottomed hole that is positioned coaxially with a normal transducer (compressional). The method is based on the solution of the elastodynamic equations with mixed boundary conditions for the

case of oscillations that are harmonic in time. From his model, he produced DGS diagrams that are similar to those produced by Krautkramer. However, in explaining the behaviour of the diagrams in the near field, he only speaks of qualitative comparison of these results. For example, he mentioned that for small targets there is a sharp minimum in the range of 0.4-0.5 NF and he confirmed this experimentally. He also concludes that DGS diagrams are not universal and that they are dependent on the factor R/λ , where R is the probe radius and λ is the wavelength of the propagating sound.

The research into DGS diagrams since they were introduced, can be summarised as follows:

- i- There are still models that produce DGS diagrams assuming the propagation medium to be fluid, arguing that the effect of the shear waves is very negligible.
- ii- Other models produce DGS diagrams for targets in a solid medium using the elastodynamic equation, which takes into account the shear waves. However, these models use much computer time.
- iii- The two kinds of assumption mentioned in the first and second points, give a qualitative description of the fluctuations seen in the near field of these diagrams without offering a quantitative description.

In the work presented here, DGS diagrams for flat-bottomed holes in isotropic lossless solid are introduced. This can be done by generating programs which use Eq (32) to generate echo responses for several targets at several ranges. Also, experimental DGS diagrams for small targets (i.e. 2mm diameter flat bottomed-holes) in solid are shown and compared with predicted DGS diagrams using the new model, for both wide and narrow band transducers. In addition, a comparison is introduced between the new DGS diagrams for targets in a solid medium and the diagrams produced for targets in a fluid medium. The reason for

this comparison is to quantitatively investigate the differences between diagrams produced for a fluid or solid medium. Finally, some other effects on DGS diagrams, such as the excitation pulse of the transducer and the method by which the amplitude of the echo is calculated, are explored.

2.4 Numerical calculations.

Echo responses from normally aligned flat-bottomed hole targets of finite dimensions are calculated by numerical evaluation of the convolution and the integral in Eq (32). The integration with respect to y is performed with a constant increment of 0.1mm. At each value of y on the target surface the particle velocity potential is calculated as a function of time using the new model and making use of the analytical expressions given in the Appendix. Then it is differentiated numerically to give the particle velocity impulse response. For targets at short ranges, the time increment used in the calculations is chosen to be less than the time difference between the arrival of the compression and plane and edge waves. This is very necessary in order to avoid any numerical errors in the calculations. Also, in order to compare measured and calculated echo responses, the time increment used in calculating the simulated echo responses must equal that of the measured transducer velocity function. At short ranges a time increment of 10ns gives adequate accuracy and the same increment could be used when digitising the experimental velocity function. As the target range increases, the time increment δt must be reduced to maintain adequate accuracy as described later in Section 4.4 that deals with DGS diagrams. It is of course crucial to make a corresponding change in the velocity function time increment and this is done by simple linear interpolation when measured velocity functions are used. The echo response can then be obtained by performing a direct time domain convolution of the particle velocity impulse response with the relevant source velocity function.

The source velocity function $v(t)$ can be in several forms. Examples of $v(t)$ that consist of several cycles of sinusoidal functions are illustrated in Figure 2.4.1. These synthetic pulses are specified by the functions

$$v(t) = \sin(\omega t) - (N/N + 1) \sin[(N/N + 1)\omega t] \quad (39)$$

for the top one and

$$v(t) = \sin(\omega t) \sin(\omega t/N) \quad (40)$$

for the bottom one, where N is the number of cycles and ω is the angular frequency. Alternatively, $v(t)$ could be measured experimentally by digitising the reflected pulse from a perfect reflector. In practice the back wall echo from a thin parallel sided aluminium block can be used for this purpose; it is assumed that any distortion of the incident pulse introduced by the reflector is negligible (G. Georgiou, 1989).

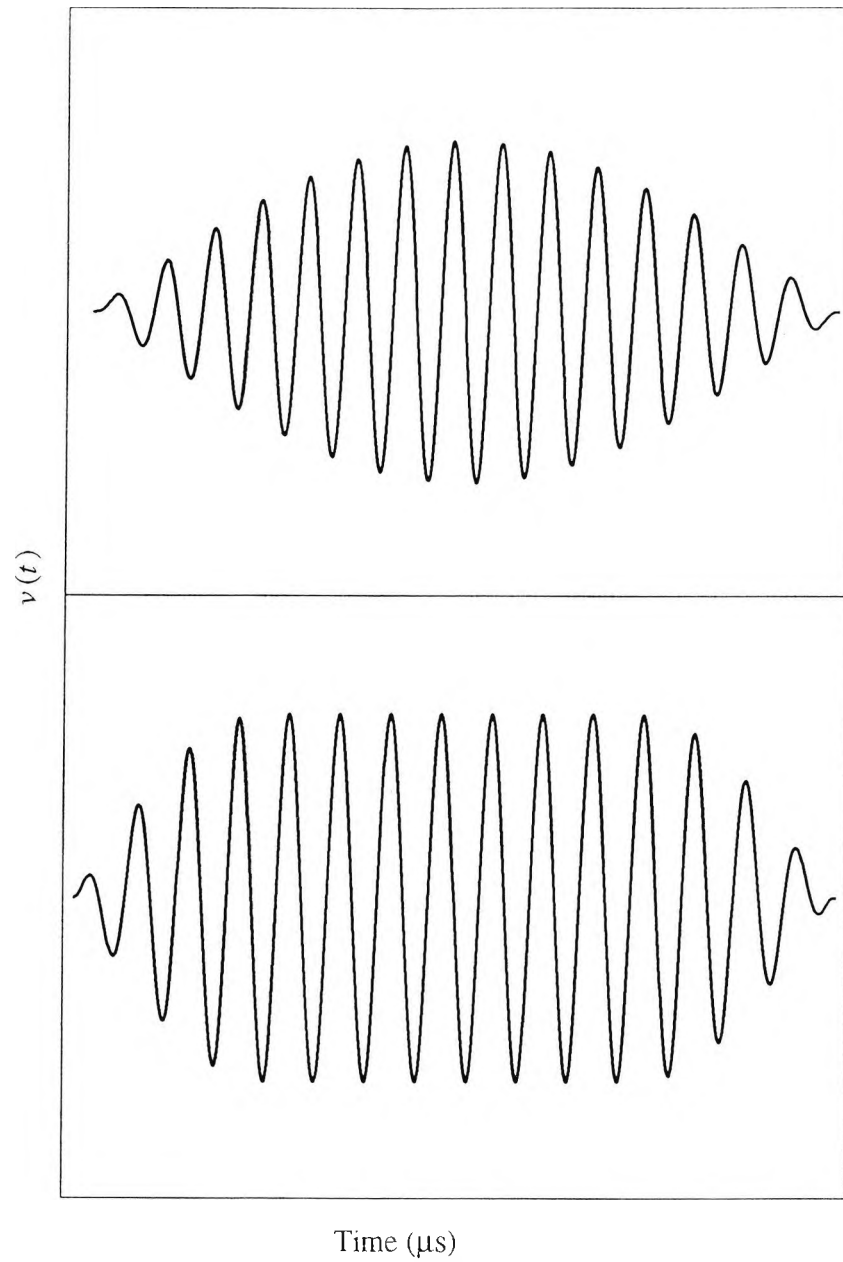


Figure 2.4.1: Graphical representation of the source velocity functions synthesized by using Eqs (39) and (40). Top is the slowly rising and decaying sine envelop function. Bottom is the plateau function.

3- EXPERIMENTAL MEASUREMENTS.

3.1 The transducers.

Two circular transducers were used to obtain all experimental results shown in this work. One was a wide-band transducer (Aerotech Alpha F08179 19mm diameter, 5MHz central frequency, $\lambda = 1.24\text{mm}$ in aluminium). The other was a narrow-band transducer (Harisonic HC-3144, 19mm diameter, 3.6 MHz central frequency, $\lambda = 1.72\text{mm}$ in aluminium). The transducers were used for obtaining short and multi-cycle pulses respectively.

3.2 The targets

The model introduced in Chapter two predicts the echo response for axisymmetric circular targets. To compare the predictions of the model with measured echo responses, FBH's were suitable because they offer an optimum reflecting surface (with the larger sizes) that is reproducible and they are relatively easy to machine. Furthermore, FBH's have many applications in NDT. For example, they are one of the oldest reference/calibration standards in the field of ultrasonic non destructive testing. They have been used for calibration of ultrasonic test equipment sensitivity, flaw detector linearity checks, near surface resolution measurement and for generation of distance-amplitude correction curves (Halmshaw, 1991). They are also useful for equivalent flaw sizing applications since they can represent the response at normal incidence of ideal "perfect" scatterers, such as flat cracks.

As has already been demonstrated the echo response from point-like targets has a complicated multipulse structure and to obtain experimental measurements to confirm this using FBH's it is important to consider the smallest practicable size. One relevant factor is the grain structure of the test material i.e. the target should have a certain size so that its echo response is not masked by unwanted grain scattering. The transducer dynamic range can also limit the smallest target that can usefully be used, since the back scattering which comes from within the transducer backing can mask the reflected signal from the target, especially when the target range is small.

Another factor that experimentally confines the target to a certain range is the 'dead time'. This is the time needed for the amplifier to recover from saturation.

Bearing in mind the above constraints it was found that a minimum FBH target diameter of 2mm could be used. Since this size was larger than some of the wavelengths within the interrogating pulses, the smallest FBH was still too large to behave as a "point-like" target and it was found that a better approximation for a small target was obtained by using a 2mm round-bottomed hole.

3.3 Experimental set-up for short pulse measurements.

Figure 3.3.1 shows the experimental set up used to capture the echo responses of targets using a single, directly-coupled wide band transducer (Aerotech Alpha F08179 19mm diameter, 5 MHz).

A Panametrics 5052PR pulser receiver unit, simultaneously triggers the digital oscilloscope and a high level pulse generator. The pulse generator produces a unidirectional pulse of several hundreds volts. This pulse is then applied to the wide band transducer that is directly coupled to the block under test. The scattered signals from targets within the block are received by the same transducer and fed to the receiver amplifier within the Panametrics 5052PR. The output from the receiver is then digitised at a sampling frequency of 100MHz using the Lecroy digital oscilloscope. The digitised waveforms are then fed to a 486 DX computer and stored as files.

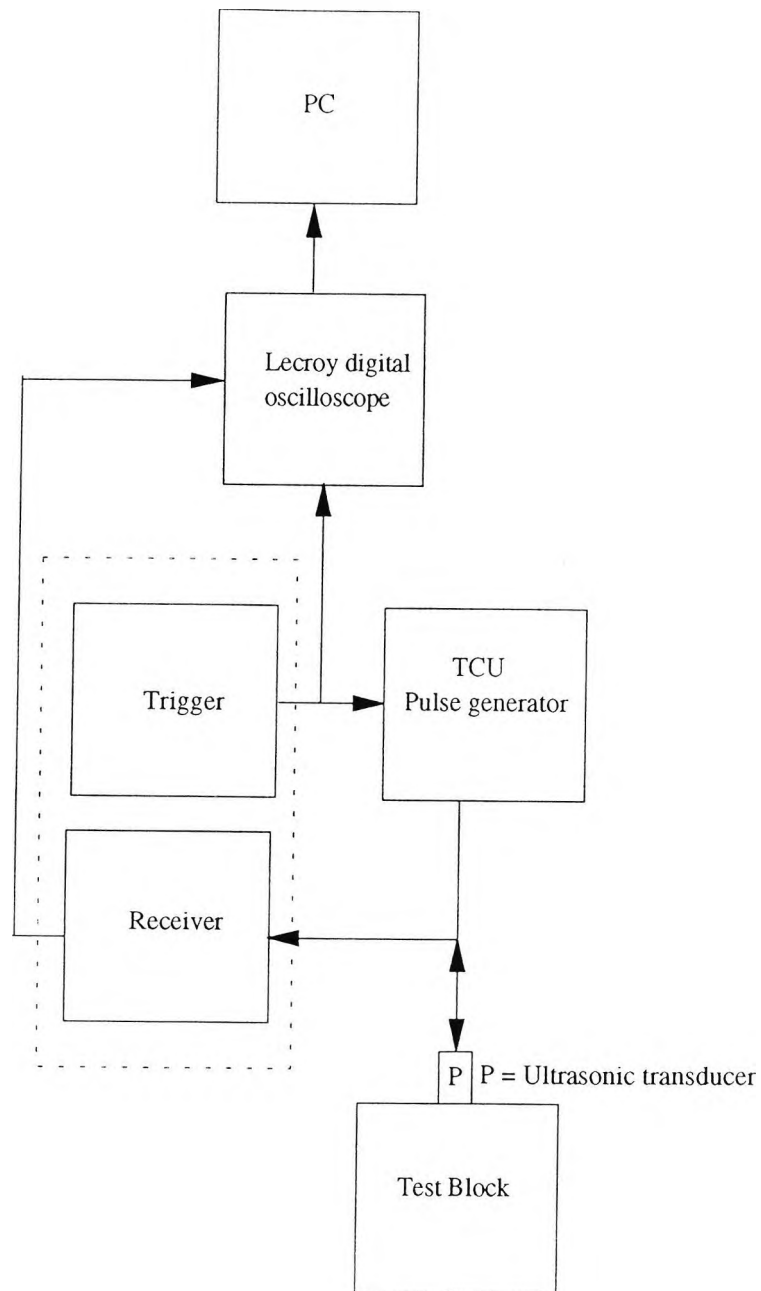


Figure 3.3.1: Block diagram of the excitation system used to capture data using the wide-band transducer. In the dotted box the trigger and the receiver are in the same Panametrics unit.

3.4 Experimental set-up for multi-cycle pulse measurements.

In order to make experimental measurements to investigate the interference effects, a controllable multi-cycle sinusoidal excitation pulse is required. A schematic representation of the set-up that produces such a pulse is shown in Figure 3.4.1. The basis of the system is a gated amplifier and a suitably synchronised high frequency sinewave generator.

The gated amplifier requires to be synchronous to the sinewave generator to generate gated sinusoidal waves that are locked to the gate control pulse. Furthermore, the pulse repetition frequency (PRF) must be adjustable, to avoid the problem of ghost echoes that can mask the echo response of small targets. In order to adjust the PRF the synchronous trigger pulse was derived using the triggering facilities of an oscilloscope. This was done by synchronising the 'Tektronix' oscilloscope type 7603 to the sinewave generator. Because the output pulse from the oscilloscope as it stands was not suitable, some pulse shaping was required. To shape the pulse, the output from the oscilloscope was used to trigger a 'Lyons Instruments LI' pulse generator (type PG 2B). This gave control over the pulse width, height, and polarity. The output pulse from the PG2B then triggers simultaneously the gated amplifier and the Lecroy digital oscilloscope.

Using this set-up, the pulse repetition frequency can be controlled using the time base of the 7603 oscilloscope. It was noted experimentally that to minimise the 'ghost echoes' a PRF as low as 20Hz was required.

At the output of the gated amplifier, the signal level is just a few volts and this must be considerably amplified prior to exciting the transducer. To give useful overall sensitivity, a pulse of several hundreds of volts is required. This is achieved by connecting the gated sinewaves to a 50dB power amplifier.

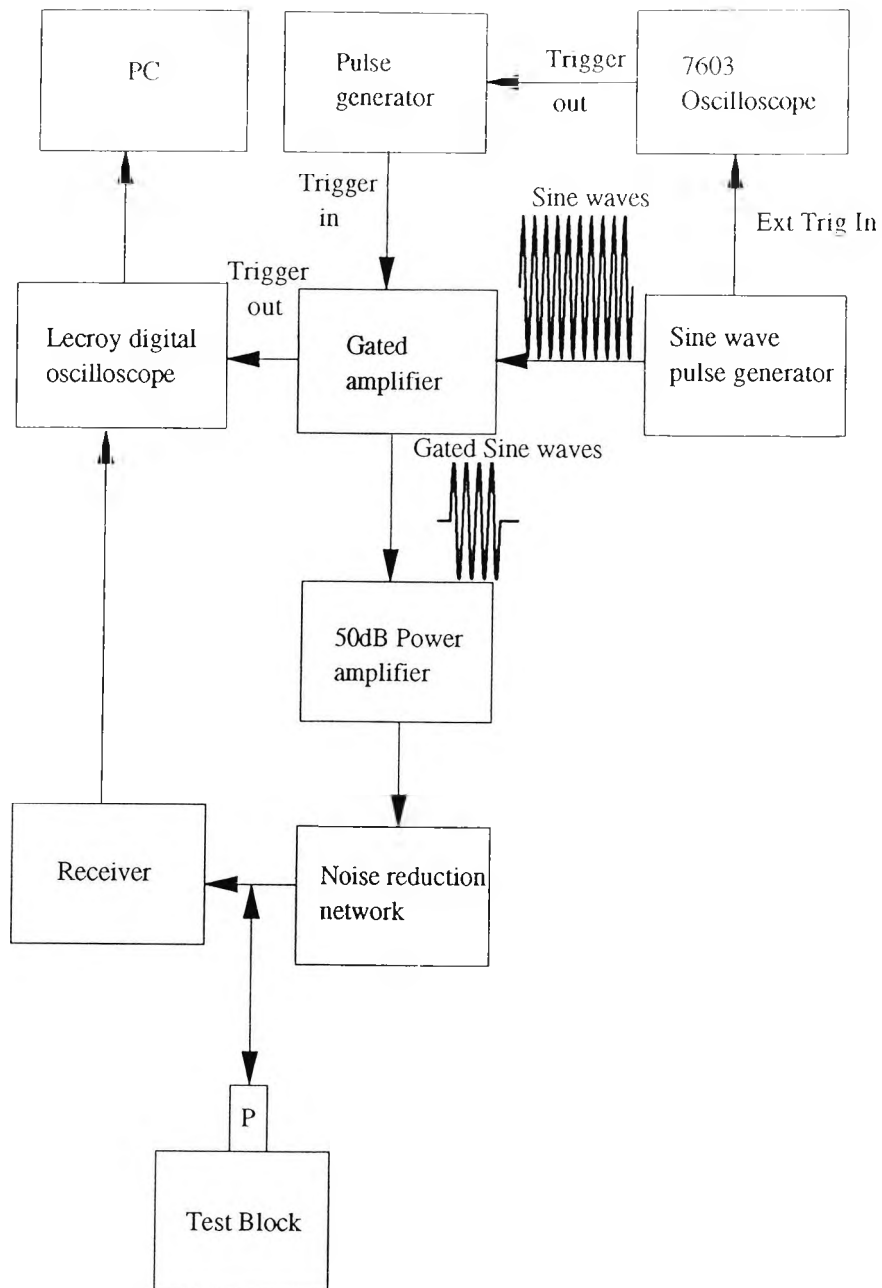


Figure 3.4.1: Block diagram of the excitation system used to capture data when the transducer is excited by gated sinusoidal waves.

Since the measured echo responses are obtained using a single transducer, the noise at the amplifier output will be connected to the receiving amplifier. As a result, extremely poor echo signal to noise ratio will occur between noise and target signals. Using an 'Hewlett Packard' r.m.s voltmeter, the measured noise was equal to 6mv. Such a noise level can be larger than the wanted echo signal from the smaller targets of interest. Fortunately, it is relatively straight forward to reject such noise using the simple diode network shown in Figure 3.4.2.

As a result of their exponential forward characteristics, the diodes will only conduct when the voltage across them is greater than $\sim 0.6V$. So, provided that the noise level is less than 600mv it will be rejected. The output voltage of the gated sinewaves is several hundreds of volts but the measured noise signal voltage is 6mv.

The reflected sound pulse is then fed to the receiver within the Panametrics 5052 PR. The received echo pulses are digitised using the Lecroy oscilloscope and the data stored as individual files on a PC.

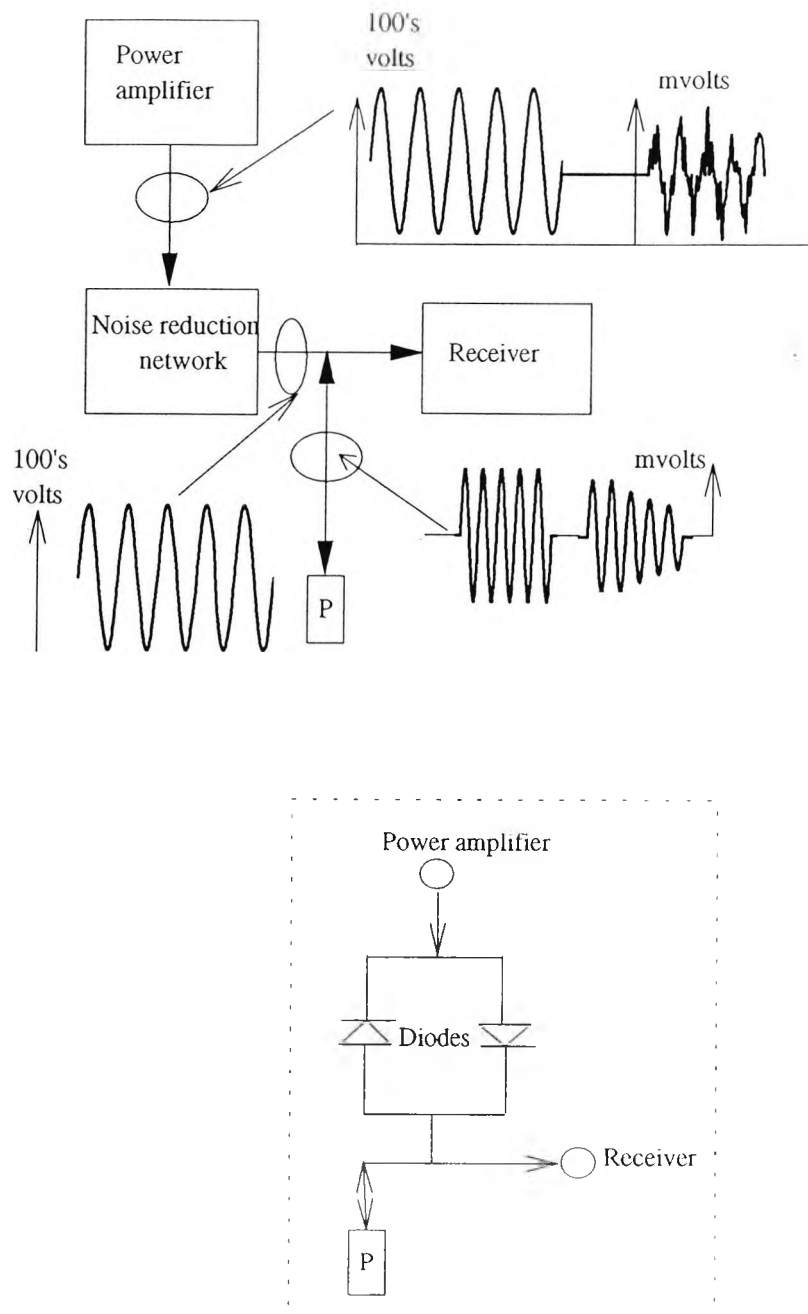


Figure 3.4.2: Block diagram showing the function of the Noise reduction network. Shown in the dotted box the construction of the network.

4- RESULTS

This chapter first introduces a method to measure the radius of the probe and experimental factors affecting the measurements of the echo responses.

Experimental results obtained using short pulses to detect 2mm diameter round bottomed-holes in steel are given. This is followed by results from 2mm and 4mm diameter flat bottomed holes (FBH's) in aluminium. These results are compared with the theoretical predictions of the present model. Using the same targets, the variations of echo responses with range, are then compared with those predicted by the model.

Measured and calculated DGS diagrams using both short and multi-cycle pulses are given. The influence of the source velocity function on DGS diagrams is then shown. Finally a comparison between the diagrams calculated using the solid model and diagrams produced using the fluid model is introduced.

4.1 Experimental factors affecting the measurements.

4.1.1 Measurement of radius of the transducer.

As will be demonstrated later in Section 4.3.4, a number of the theoretical results are particularly sensitive to changes in the effective source radius. Thus to obtain a true comparison between the theoretical and measured waveforms it is necessary to accurately measure the true radius of the transducer. It turns out that an uncertainty in the effective radius of the transducer has the largest effect on the echo response for the case where a multicycle pulse is used to interrogate a small target at a range where destructive interference occurs between the compression plane and edge wave components. Such a combination of experimental conditions can be employed to make accurate measurements of the effective source radius.

To measure its radius, the transducer was immersed in a scanning tank filled with water and was positioned to be axially aligned with the centre of a small (0.8mm diameter) flat-ended cylindrical target. The measurements were taken with the frequency of the (gated) sinewaves accurately set to 3.6MHz using a digital frequency meter. The distance between the target and the probe was adjusted to be close to the range where the PD between the plane and edge waves was 2λ (a "destructive interference" range - see Section 2.2.5, p 22). The target range was then adjusted until a null in the pulse was observed, confirming that the PD was accurately 2λ . The true radius could then be found using Eq (28). Since the method requires an accurate figure for the velocity of sound, the temperature at which the measurements were taken was monitored using a digital thermometer (accuracy $\pm 0.1^\circ\text{C}$). The average temperature was 18.3°C , the corresponding sound velocity in water being $1.48\text{mm}/\mu\text{s}$.

The range was measured using the positional sensors ($\pm 0.1\text{mm}$ accuracy) incorporated in the scanning tank, by first positioning the probe so that it touched the target and then moving it away until the null in the echo pulse was at an exact minimum. This was repeated five times and an average figure taken for the destructive interference range (55.21mm , corresponding to a PD of 2λ). Using Eq. 28, the figure obtained for the source radius was 9.55mm . As it turns out, this was

in fact close to the nominal radius of 9.53mm stated by the manufacturer, but as stated above it is particularly important to accurately know the true radius, and there was no guarantee that the nominal radius was accurate. The way in which errors in the transducer radius affect predicted echo pulse shapes and amplitudes is investigated quantitatively in Section 4.3.4. Similarly, their affect on defect sizing using DGS diagrams is demonstrated in Section 4.6.

4.1.2. Uncertainties in measurements of the echo responses.

Several uncertainties can affect the experimentally obtained echo responses. Firstly, the errors associated with the geometry of the test targets must be considered. The 2mm and 4mm FBH's were machined using specially ground drills. To minimise errors in flatness, the drill was ground on a numerically controlled machine. A check was made on the sensitivity of the calculated echo responses to an error in length of the metal path to each target. The metal path was found by measuring the thickness of the block and depth of the hole using a vernier gauge and subtracting. The estimated accuracy of the metal path was 0.5mm. Feeding this uncertainty into the model showed that the corresponding error in the predicted echo response amplitude was $\pm 3\%$ for the 2mm diameter FBH. For larger targets the error becomes smaller.

The velocity of sound in the test blocks was measured using the method of successive back wall echoes as displayed on the digital oscilloscope. Knowing the thickness of the block, the velocity of sound in the metal was 6.2mm/ μ s, with estimated uncertainty of $\pm 3\%$.

In addition to these uncertainties, there are several factors which can affect both the shape and amplitude of the echo responses of the targets. A major factor is the coupling condition. If the couplant is not uniform over the face of the transducer, the symmetry of the radiated edge waves will be severely affected. As a result, all edge-wave contributions to the overall echo response will be smaller than with true uniform coupling. This effect will lead to errors in echo pulse shapes and amplitudes, especially for small targets, where the effect of the edge waves is

pronounced (as seen later in the measured echo responses for 2mm diameter round-bottomed targets). To ensure the full propagation of both the plane and edge waves, the transducer surface was uniformly and smoothly covered with the couplant and the transducer and test block were carefully lapped. To ensure that the maximum sound energy has entered the metal, the couplant layer was made as thin as possible. As a further check on experimental conditions, repeated checks were made to monitor the reproducibility of the back-wall echo from a region free of known defects.

It should be mentioned that uncertainties that result from the couplant and the flatness of the transducer cannot be easily be estimated quantitatively. To guard against such errors, the measured echo responses were taken several times for each target and the uncertainty in the echo amplitude due to coupling effects was estimated to be $\pm 5\%$.

When measuring relative amplitudes, using an attenuator and a digital oscilloscope, the uncertainty was estimated $\pm 4\%$, leading to an overall accuracy in the measured results of $\pm 12\%$.

4.2 Echo responses from point-like targets in steel.

In this section, a comparison between calculated and measured echo responses for point-like targets is shown. The target sizes and shapes were as discussed in Section 3.2 but briefly, the most suitable practical point-like target was found to be a 2mm diameter-round bottom hole, whereas the calculated results were close to those of an ideal point-like target if a FBH of 1mm diameter or less was assumed.

Figure 4.2.1 shows measured and calculated echo responses for small targets in steel. As described in Section 2.5, to give a good comparison between calculated and measured echo waveforms, the shape of the theoretical source velocity function has been chosen to match the shape of the measured back wall echo (shown inset to the same time scale) of a thin parallel side steel block of 10mm thickness. The theoretical waveforms for each target range have been obtained by convolving this pulse with the appropriate target impulse response.

The agreement between the calculated and measured results is generally good in terms of the *pulse shape*, bearing in mind that the comparison between the simulated and the measured results is for different target shapes (although both are reasonable approximations of a point target), and the existence of coherent ultrasonic "noise" (see Section 3.2). Another possible reason for these differences is the coupling error discussed above in Section 4.1.2.

At 10mm range, the compression group (C) is clearly seen containing the plane P_cP_c and P_cE_c pulses. The P_cE_c pulse is seen to have a different polarity from the plane wave pulse. The C/S group can be seen after the compression packet. Again the difference in polarity is clearly seen in the two components, in both the measured and calculated results.

Further away from the transducer, at 15mm range, the pulses forming the C group start to overlap, and the separation between the pulses is less noted.

Also, as predicted by the model (section 2.2.6), the C/S group is further separated from the C group.

The S group at the two ranges is very small compared with the other two packages, especially at the longer range as discussed earlier in section (2.2.5, p 27).

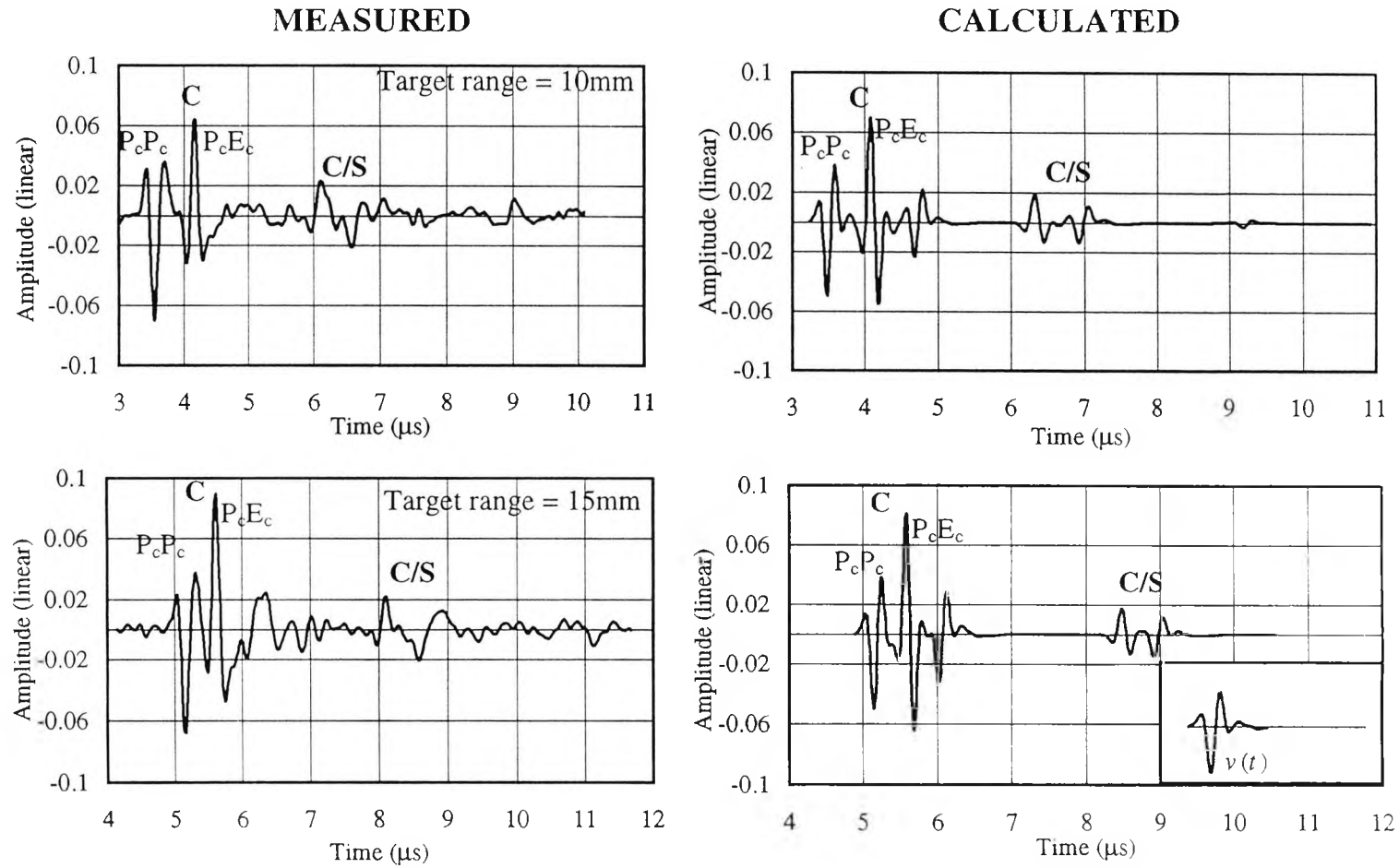


Figure 4.2.1: Measured and calculated echo responses for point-like targets in steel. The measured echo responses were taken using a 19mm diameter wide band transducer excited with a 4MHz short pulse (shown inset). C and C/S denotes the compression and the compression shear groups of the pulse.

4.3 Echo responses from FBH's in aluminium.

In order to evaluate the usefulness and accuracy of the model described in section 2.6, a number of experimental measurements of echo responses from 2 and 4mm-diameter FBH's were made and compared with corresponding theoretically predicted results. The experimental measurements were made using transducers excited with both short and multi-cycle pulses.

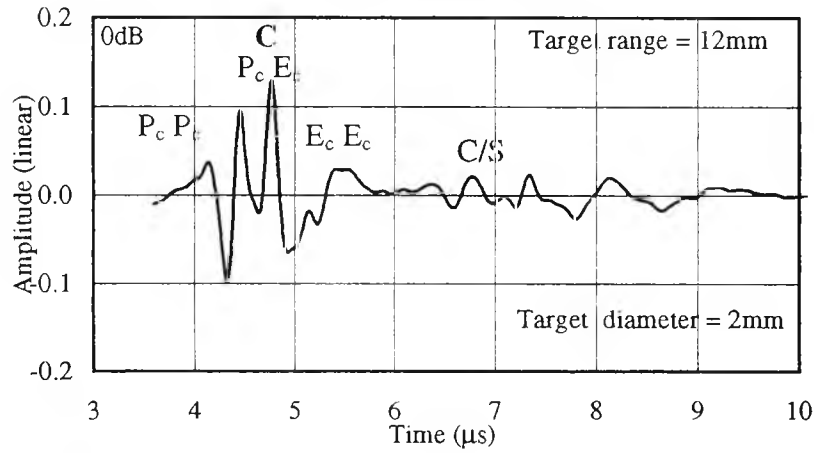
4.3.1 Echo responses from 2mm and 4mm FBH targets.

Figure 4.3.1 shows measured and calculated transmit-receive mode waveforms at a range of 12mm for 2mm and 4mm diameter targets when interrogated by a short pulse from a Panametrics transducer (4MHz, 19mm diameter). As before, the shape of the theoretical source velocity function has been measured by taking the back wall echo (shown inset) of a thin parallel sided block. Here, a 10mm-thick aluminium block was used. The theoretical waveforms were obtained by convolving the source velocity function with the appropriate impulse response.

In general, there is good agreement between the predicted and measured echo responses. However, as is the case for the results from the 2mm round-bottomed holes shown in Figure 4.2.1, there are a number of small discrepancies due to the non-ideal behaviour of the transducer. Note that even though the present model does not take into account Rayleigh and head waves, there is reasonable agreement in the detailed structure of the predicted and measured results. Note also that with all targets greater than about 1mm diameter, the pure shear (S) components are in general insignificant and no attempt has been made to display them in Figures 4.3.1-8.

The pulse denoted 'M' in the measured result for the 4mm diameter target is a "multiple" echo arising from that portion of the first-received pulse that is reflected from the coupling surface to be further scattered by the target. In its present form, the new model does not take such effects into account. Note that the corresponding multiple pulse with the 2mm target is too small to be clearly seen.

MEASURED



CALCULATED

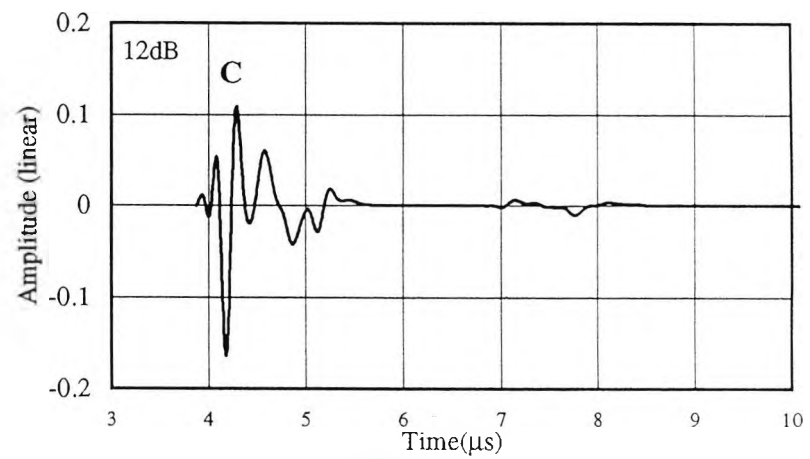
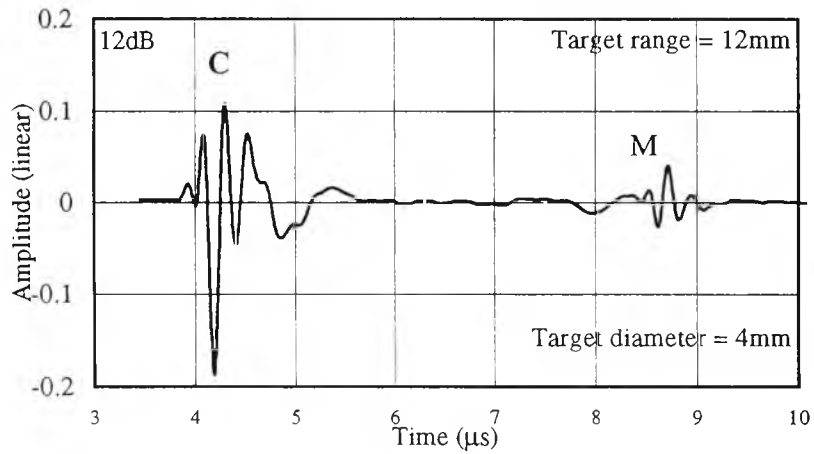
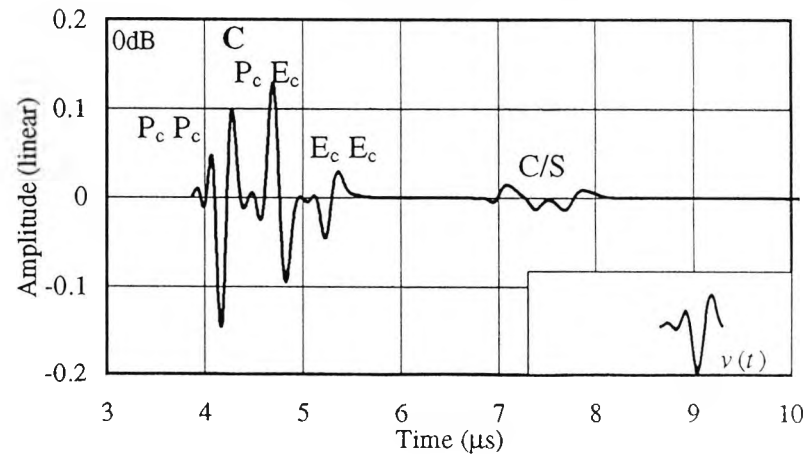


Figure 4.3.1: Measured and calculated echo responses for 2mm and 4mm diameter flat-bottomed holes in aluminium, using a 19mm diameter transducer excited with a 4MHz short pulse (shown inset).

For targets at a range of 12mm, the pulses of the compression group C can be clearly seen, especially the P_cP_c and the P_cE_c pulses with their opposite polarities for the case of the 2mm target. The P_cE_c pulse is less pronounced in the echo responses for the 4mm target as would be anticipated from the explanation of the effect of target size given in Section 2.3.4. The two pulses of the C/S group can also be clearly seen.

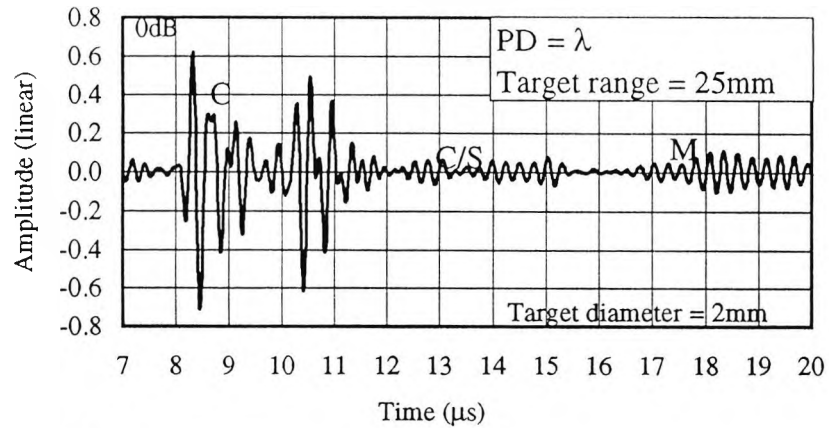
In the results shown in Figure 4.3.2 a multi-cycle excitation pulse was used. It was decided to use a suitable target range of 25mm, where at 1λ the PD gives complete destructive interference over the "steady state" region of the C group. The centre frequency of the multi-cycle pulse was 3.8MHz. The relative sensitivities in the experimental results for each target are given by the scale factors in dB in the left hand corner of each experimental measurement. Again, it can be seen that there is good agreement between the measured and calculated echo responses for both targets.

In the measured and the calculated echo responses for the 2mm target shown at the top of Figure 4.3.2, the null region can be seen in the middle of the compression group 'C'. The existence of this null region makes it look as though there are two separate pulses that could be falsely interpreted as coming from two closely spaced targets. In fact it is just an interference effect over the various components of the C group from a single target.

For the case of the 4mm target, the destructive interference between the plane and edge waves can still be noted, but its effect is not as strong as in the 2mm target case. This is because as the target size increases, the contribution of the plane waves becomes larger than that of the edge wave and hence the echo response is dominated by the plane wave pulse.

Although two completely different source velocity functions were used in obtaining the results shown in Figures 4.3.1 and 4.3.2, there can in fact be quite significant differences in small target echo pulse shapes for relatively subtle changes in

MEASURED



CALCULATED

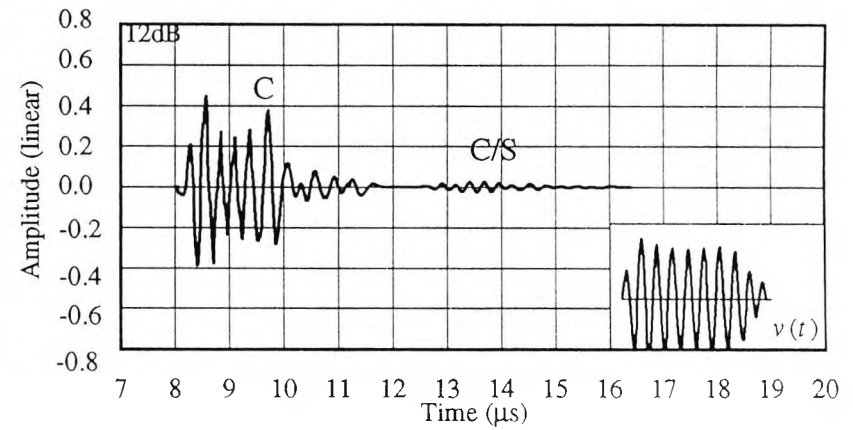
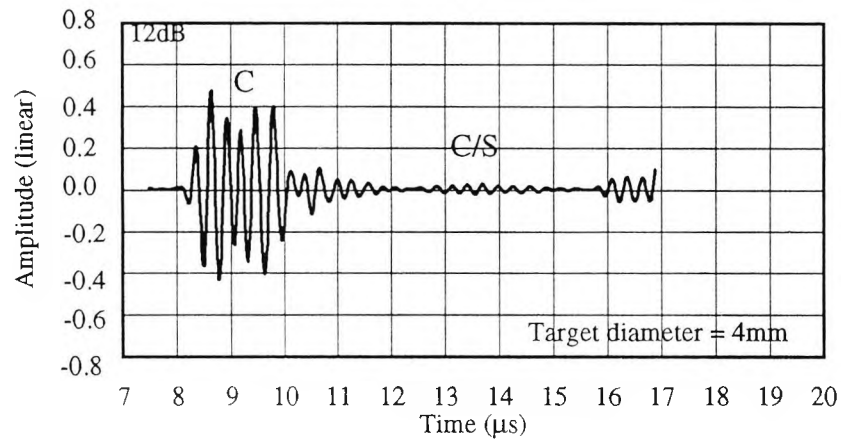
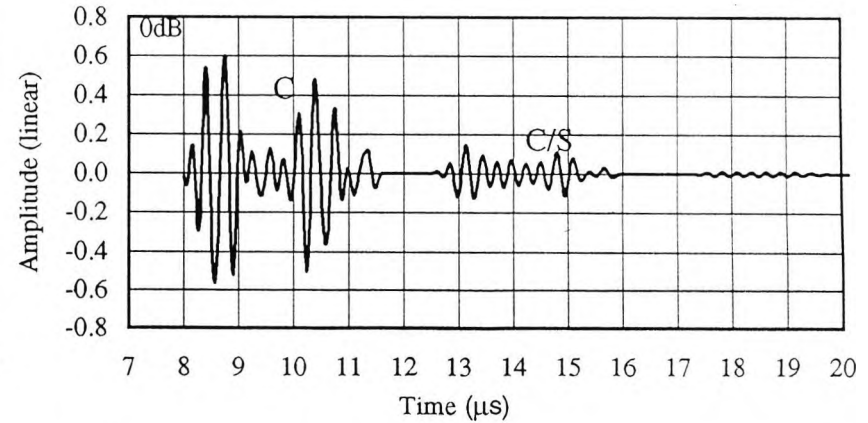


Figure (4.3.2): Measured and calculated echo responses for 2-mm and 4mm diameter targets using a 19mm diameter transducer excited by a 3.8MHz multi-cycle pulse (shown inset) at ranges where destructive and interference occurs. "M" denotes a multiple reflection in the measured result at 25mm range.

velocity function. For example, Figure 4.3.3 shows calculated echo responses for 2mm and 4mm diameter FBH's at the same range and for the same source diameter and centre frequency as in Figure 4.3.2, but with the two velocity functions shown inset. For the 2mm target, there are pronounced differences in pulse shape above that due to the difference in the velocity functions themselves. Again, with the plateau function (right) the echo response could be confused as coming from two separate targets, whereas with the sine envelope (left) function this is not the case, there being one continuous C group. Note also that there is around a factor of two difference in the peak-to-peak amplitude of the two responses, even though the source functions have the same amplitude.

With the larger 4mm-diameter target the difference in the echo response using each velocity function is much less dramatic and is virtually just that due to the different shape of the functions themselves. The explanation briefly stems from integrating the impulse response over the area of the target (see p61 and Section 2.2.7, p 34).

4.3.2 Variation of echo responses with target size.

Figure 4.3.4 shows calculated echo responses for 2mm, 4mm, 9mm and 19mm diameter FBH's at 12mm range, interrogated by short (a) and multi-cycle pulses (b) centered at 3.8MHz. Again a 19mm diameter source is assumed.

From Figure 4.3.4a, the result for the smallest 2mm-diameter target shows the complicated multipulse structure ascribed to diffraction effects and described in Sections 4.3.1 and 2.3.3. At just over 1 (centre frequency) wavelength across, this target behaves as a point-like scatterer.

The result from the 4mm-diameter target shows a similar multipulse structure, but the edge wave contributions are smaller and smeared out in time (see Sections 2.3.4 and 4.3.1). With even larger targets (9 and 19mm diameter), the multipulse structure is less evident, the response being dominated by the first arriving plane wave contribution (again see Section 2.2.7). The 19mm-diameter target, being some 15 wavelengths wide results in an essentially specular reflection of the direct

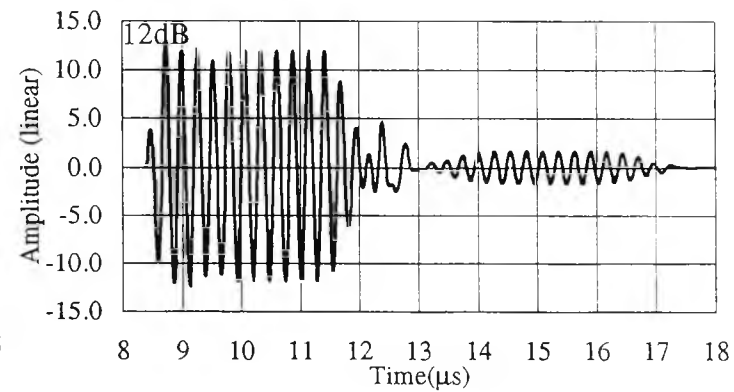
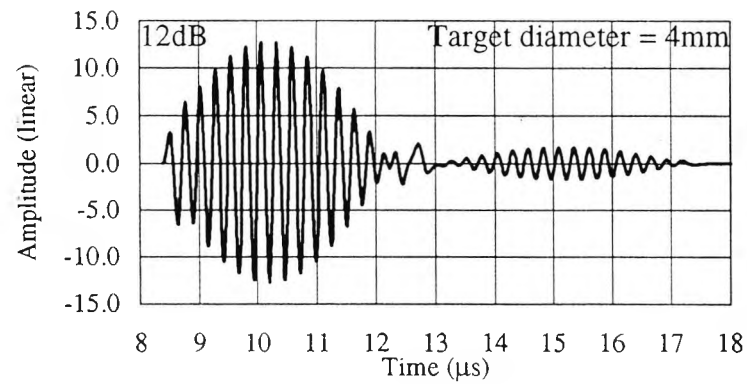
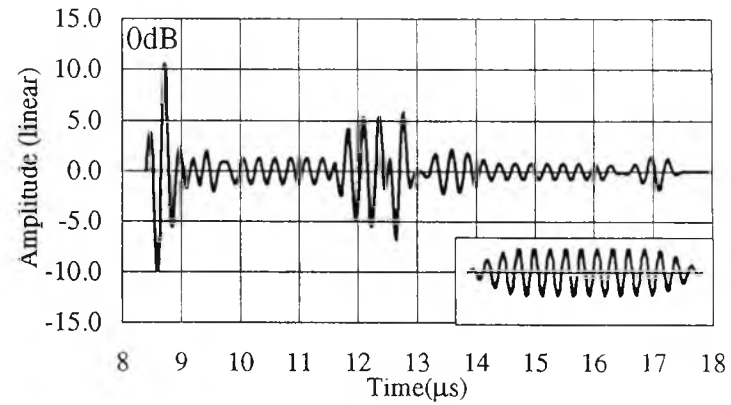
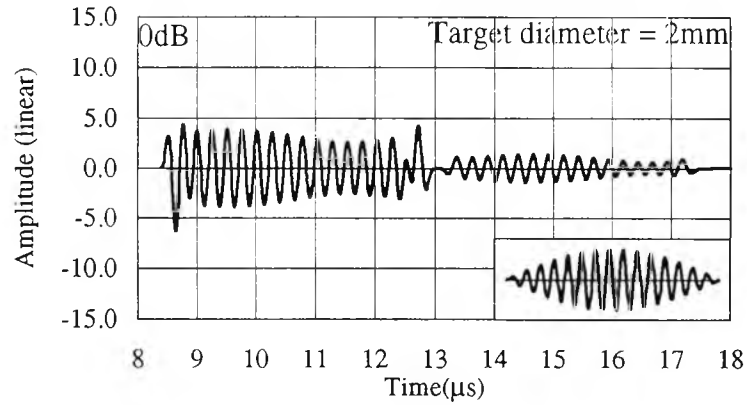


Figure 4.3.3 : Calculated echo responses for 2mm and 4mm diameter FBH's using two different source velocity functions (shown inset) at 25mm.

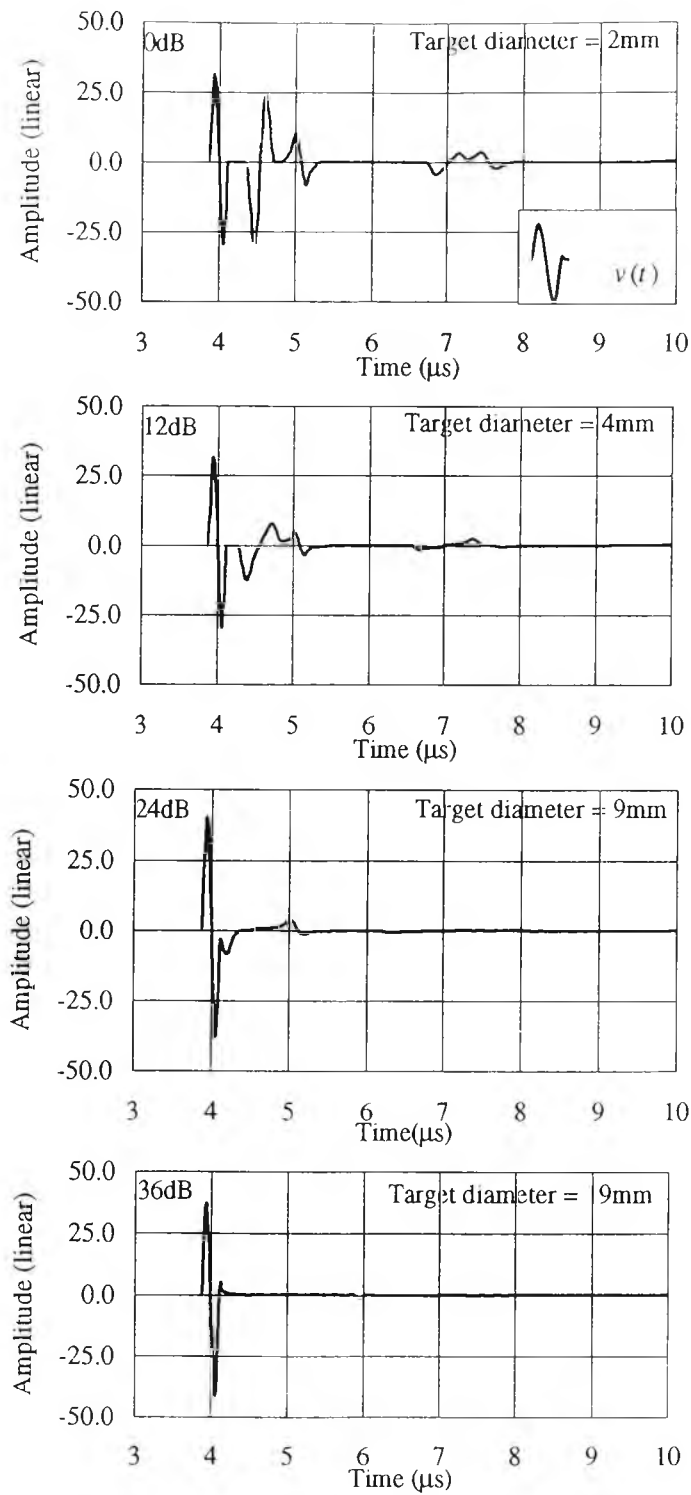


Figure 4.3.4a: Calculated echo responses for several target sizes at 12mm range assuming a 19mm diameter source emanating a single cycle pulse (shown inset) centred at 3.8MHz.

plane wave with just a very small contribution from the edge waves, as illustrated at the bottom of Figure 4.3.4a. It should be mentioned that although the plane wave contribution retains the same shape with increasing target size, its amplitude increases. The increase is approximately proportional to the (planar) target area.

Figure 4.3.4b shows a similar set of results except that the source velocity function is now a multi-cycle pulse centred at 3.8MHz. Since the PD at this frequency, source diameter and target range is almost exactly 2λ , for small targets there will be a marked effect due to destructive interference of the various plane and edge wave components (as also shown in the measured echo responses of Figure 4.3.2). The resulting null region in the steady portion of the response is clearly seen with the 2mm-diameter target but with the larger targets, this is no longer evident. Again this results from the fact that the interfering contributions are no longer of similar amplitude.

It is interesting at this point to consider the way in which the overall echo pulse amplitude changes when the target size increases from 2 to 4mm for both the short and multi-cycle source velocity functions. When the short pulse source velocity function is used, the increase in amplitude is proportional to the target area, i.e. the echo amplitude for the 4mm target is four times larger than that of the 2mm target. This stems from the integration of the plane wave over the surface of the target. Also at such short range, there is no interference between the pulses since they are separated. However, when the multi-cycle source velocity function is used, the echo amplitude for the 4mm target is nearly 6 times larger than that of the 2mm target. The explanation for such deviation can be for two reasons. The first one is that the edge wave contribution in the case of the 2mm target is strong and is nearly equal to that of the plane wave. So, when these waves destructively interfere they nearly cancel each other out. For the case of the 4mm target, the plane wave contribution is larger than that of the edge wave. Hence, the result of the interference will not be as dramatic as in the case of the 2mm target. Hence at this range and for these target sizes the rise in the amplitude is not proportional to the target area.

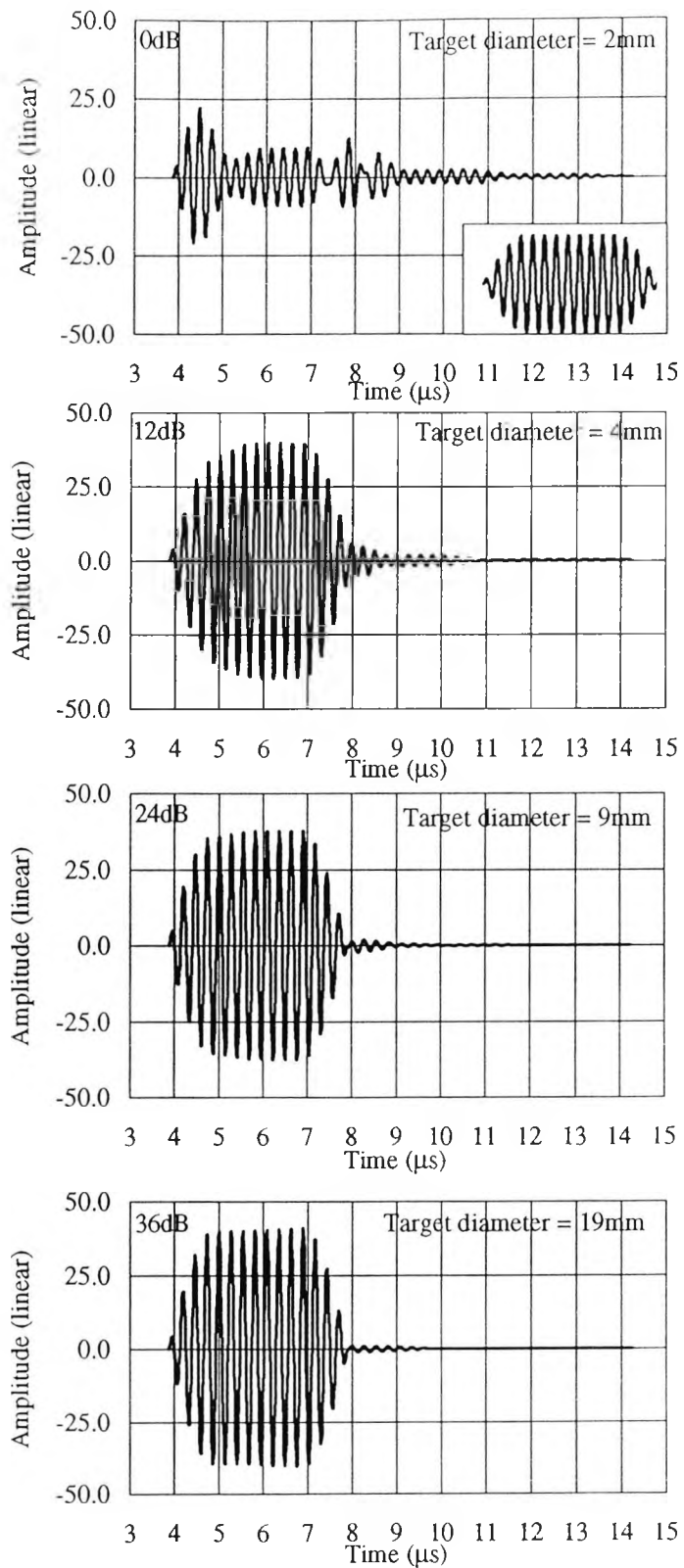


Figure 4.3.4b: Calculated echo responses for several target sizes at 12mm range assuming a 19mm diameter source emanating a 15-cycle pulse (shown inset) centred at 3.8MHz.

For both source velocity functions, moving from 4mm target to the bigger targets, the increase in the overall echo amplitude is proportional again with to target size. This is because the echo response is dominated by the plane-wave contribution.

Finally, note that in this section the variation of echo response with target size is discussed at just one range (12mm). An investigation of the variation of echo response with range for two different target sizes is discussed in the next section. These variations in echo amplitude with target size and range have important implications for defect sizing using DGS diagrams as discussed in section 4.4.2.

4.3.3 Variation of echo responses with target range in the near field.

In this section, the variation of echo response with range is considered only in the near field. In the far field the variation of echo responses is well documented and will be considered later when dealing with DGS diagrams in section 4.4. The way in which the axial response from 2mm and 4mm diameter targets varies with near-field range is illustrated in Figures 4.3.5 and 4.3.6. Both theoretical and experimental results are given. The theoretical source velocity function has been chosen to be a back wall echo (shown inset) from 10mm aluminium block. To match the calculated amplitudes with the measured amplitudes, the positive peak amplitude of the calculated echo response for the 2mm target at 12mm range was scaled to the measured positive peak amplitude of the same target. The subsequent results are plotted using the same scaling factor but note that the relative sensitivities in the experimental and calculated results for each target are given by the scale factors in dB in the left hand corner of each experimental measurement.

There is good agreement between the predicted and the measured echo responses at several ranges in terms of both amplitude and shape. Close to the transducer (Figure 4.3.5) at a range of 12mm, the echo response is the same as that described in Figure 4.3.1. The multipulse structure due to diffraction effects is clearly evident. With increasing range, the PD between the plane and diffracted compression edge waves becomes smaller causing them to progressively overlap. With the short pulse excitation used here and with these near field results, the

MEASURED

CALCULATED

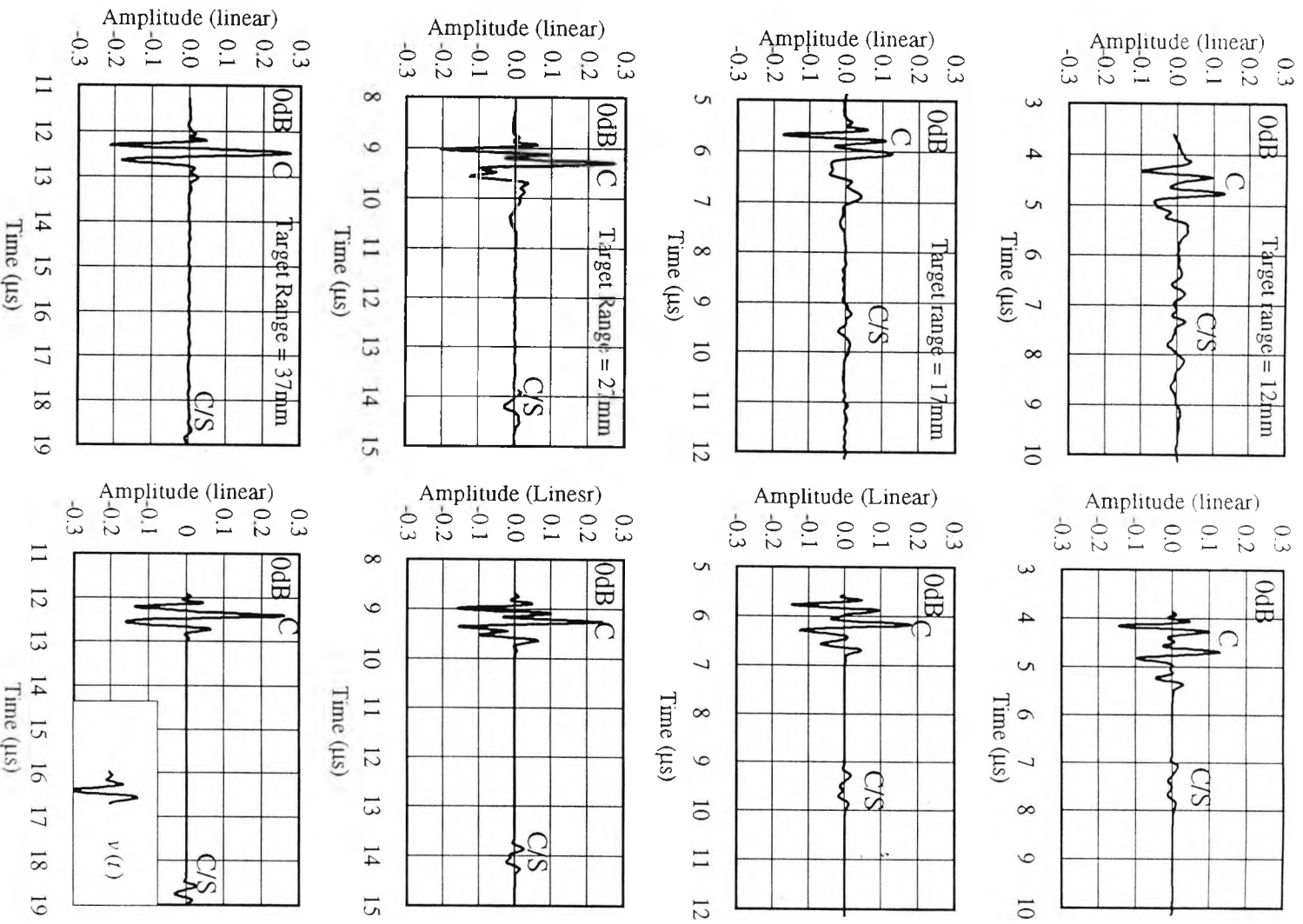


Figure 4.3.5: Variation of short pulse echo responses with range for the 2mm diameter FBH.

MEASURED

CALCULATED

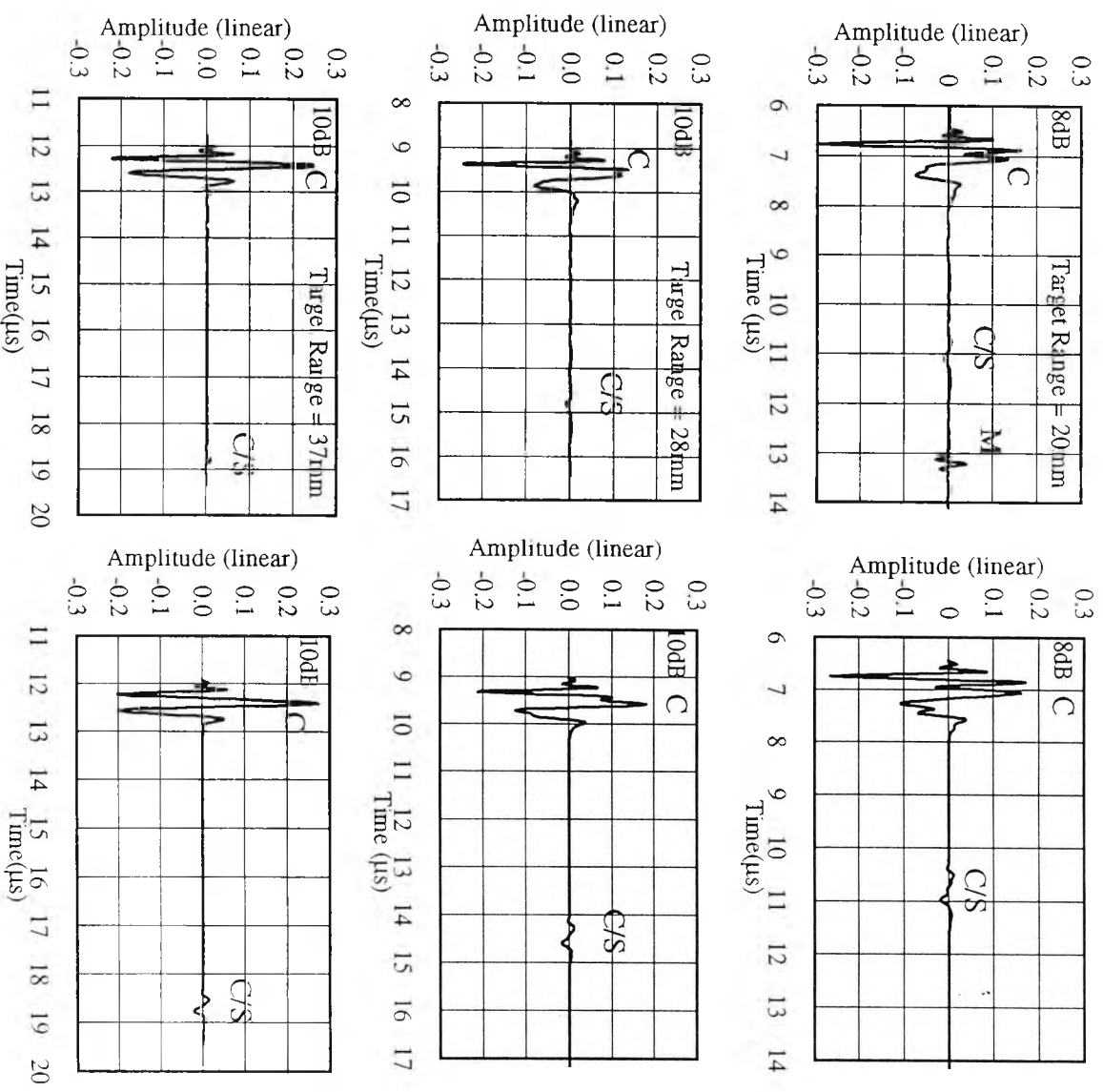
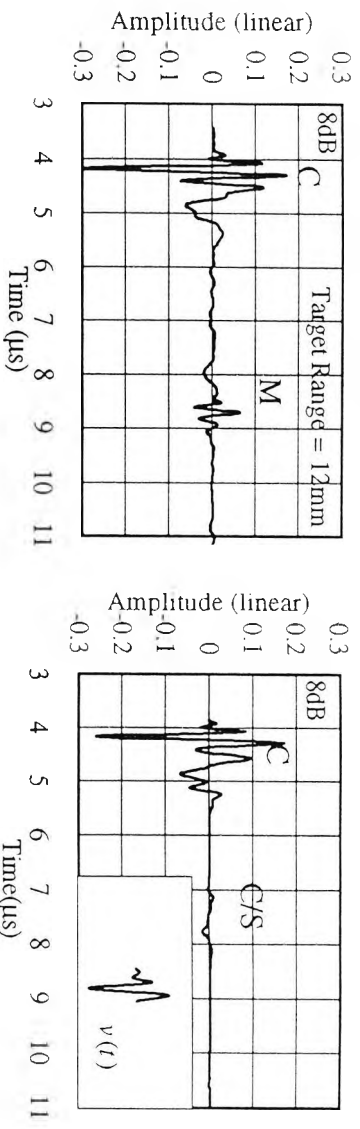


Figure 4.3.6: Variation of short pulse echo responses with range for 4mm diameter FBH.

pulses can only interfere constructively to give an increase in pulse amplitude with range. Note also that as a result of the variation of mode conversion with angle subtended at the source rim, the contribution of the compression edge wave becomes larger with range while the shear edge wave contribution becomes smaller, exactly as predicted in Section 2.3.3. These effects result in the echo amplitude with the 2mm target increasing by 6dB as the target range increases from 12 to 37mm.

From Figure 4.3.6 it can be seen that the rise in echo amplitude with range for the case of the 4mm target is smaller than that for the case of 2mm target. The increment in the echo amplitude between 12mm and 37mm is roughly 2dB. This is because the edge wave contribution is relatively smaller (see Section 4.3.2 above) than the compression plane wave contribution. So, even though their contribution is increasing with range, their effect on the overall response is too small to produce a pronounced increment in the amplitude. Further discussion about the variation of short pulse echo amplitude with range and size is introduced Section (4.4.1)

Similar sets of results for those shown in Figures 4.3.5 and 6 for short pulses are given in Figures 4.3.7 and 8 but for a multi-cycle pulse centred at 3.8 MHz. A different set of ranges was used, corresponding to a PD range from λ to 0.5λ . The matching between calculated and measured amplitudes was done in the same way as in the case for the short pulse results but this time the matching range was 25mm. Again, the relative sensitivities in the experimental and calculated results for each target are given by the scale factors in dB in the left hand corner of each experimental measurement.

For the case of the 2mm target (as shown in figure 4.3.7) at 25mm range, the false 'double' pulse structure as explained before is clearly seen. When moving to a further range, i.e. 29mm ($PD = 0.92\lambda$), the central null region in the pulse disappears and instead there is just a slight drop in amplitude as a result of the partial destructive interference. Further away from the transducer, at range of 35mm ($PD 0.77\lambda$), there is partial constructive interference, leading to an

MEASURED

CALCULATED

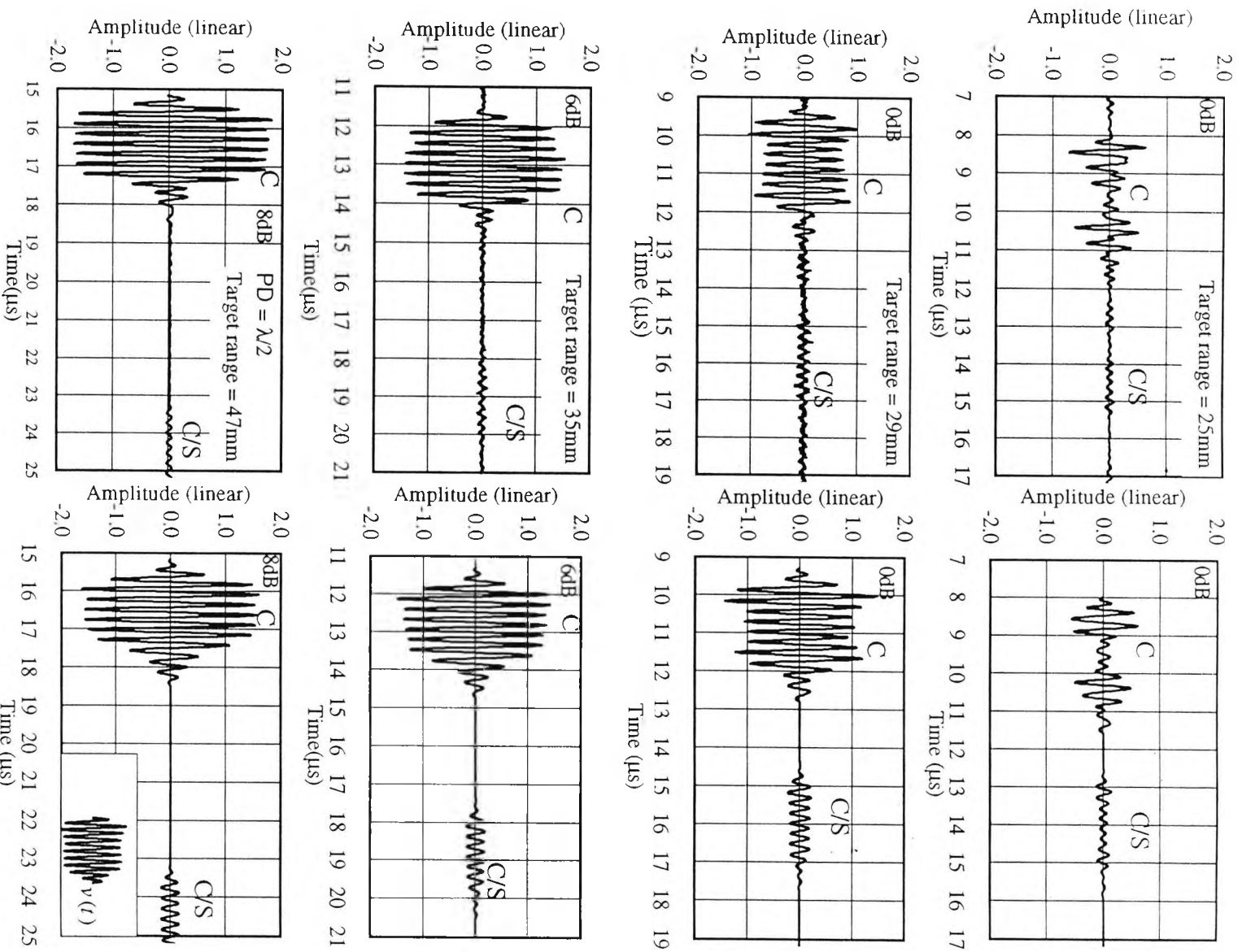


Figure 4.3.7: Variation of multi-cycle pulse (3.8MHz and 19mm diameter transducer) echo response with range for 2mm diameter FBH.

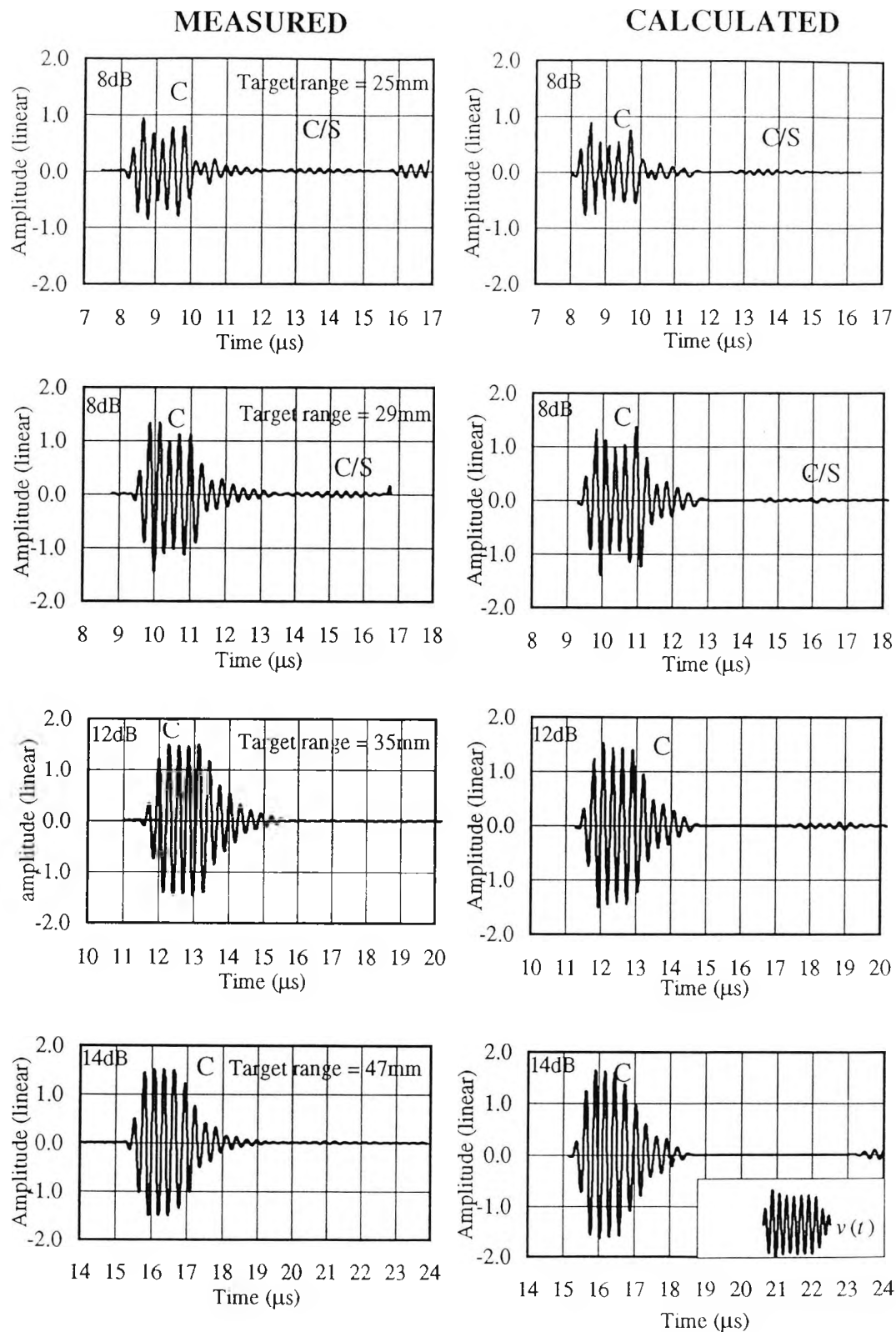


Figure 4.3.8: Variation of multi-cycle pulse (3.8MHz and 19mm diameter transducer) echo response with range for 4mm diameter FBH.

increase in amplitude compared to those at the shorter ranges. When the target position is at the range where PD is 0.5λ (47mm), full constructive interference occurs giving rise to a pulse having an amplitude which is some 17dB higher than that at the considerably shorter range of 25mm.

For the case of the 4mm target, (as can be seen in Figure 4.3.8) at a range where PD is λ , i.e. 25mm, as explained earlier in Section 4.3.3, the destructive interference between plane and edge waves is less noted than in the case of the 2mm targets. At further ranges, the variation of the echo response has a similar behaviour to that of the 2mm target, especially at 47mm range where the PD is $\lambda/2$. Finally the increase in amplitude when moving from 25mm to 47 mm is roughly 10dB. The implications of these large echo amplitude variations with range are further discussed when the relation between the target size and its echo amplitude and range are investigated in section 4.4.3

4.3.4 Effects of uncertainties in transducer radius.

In the previous sections variations in echo responses with target size and range have been explored. Investigations showed that accurate predictions of echo responses depend very much on the true diameter of the transducer used. So, at this point, it is appropriate to demonstrate quantitatively how uncertainties in the transducer diameter affect the echo response.

Figure 4.3.9 shows two sets of calculated echo responses for 1mm diameter FBH at a destructive interference range (35mm) assuming a 5MHz transducer excited with two different multi-cycle pulses (shown inset). The transducer diameter has been slightly changed from 19mm (the wanted radius) to 19.2mm and 20mm diameter. These changes in the diameter represent errors that might result from measuring its effective diameter. These errors are approximately 1% and 5% respectively.

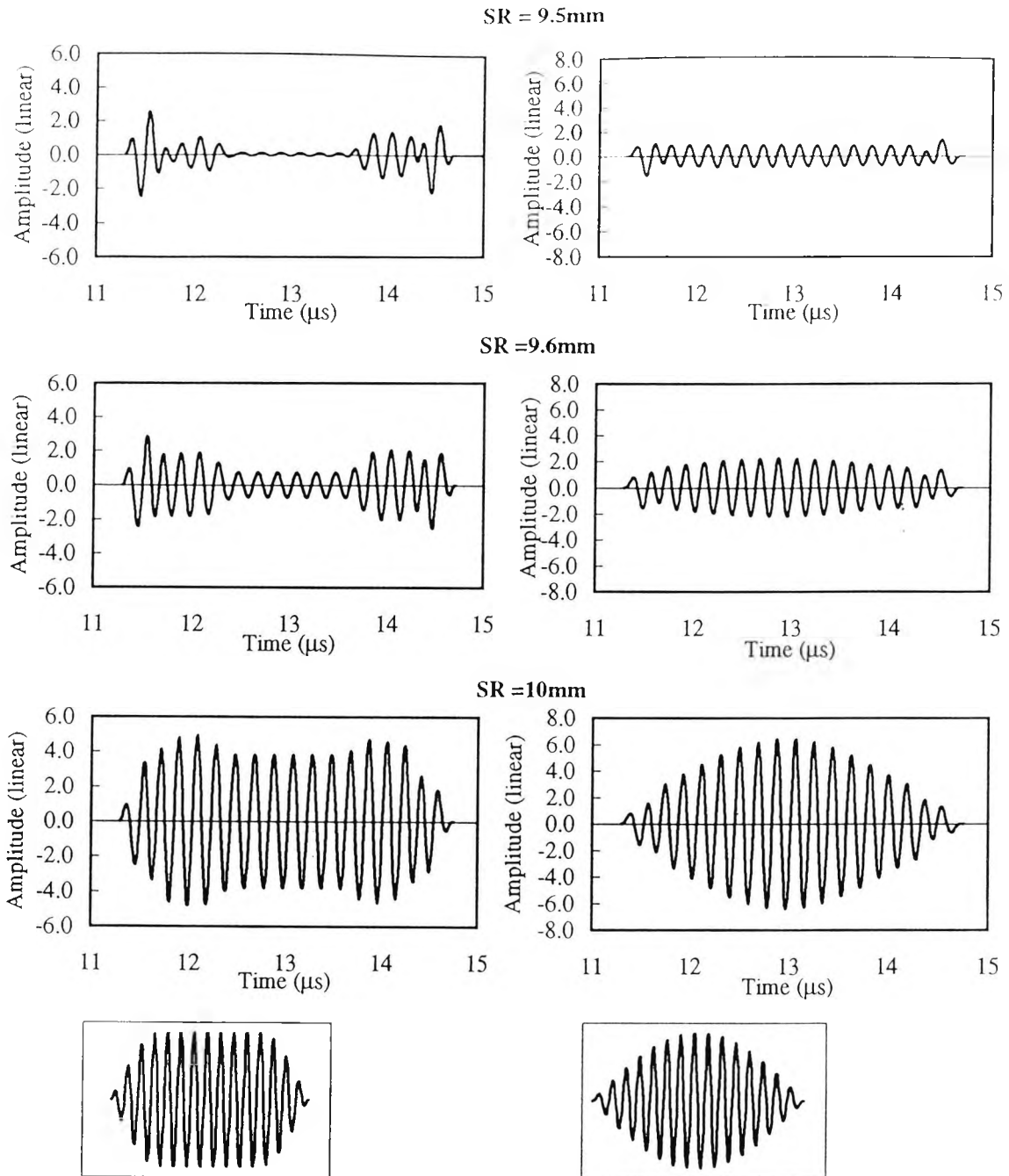


Figure 4.3.9: Two sets of echo responses for 1mm diameter target at a destructive interference range (35mm) obtained with different source radiuses (SR), excited with two different source velocity functions (at the bottom of each set). The echo response shows only the C group contribution since other groups contributions are negligible.

From Figure 4.3.9 the variation in echo pulse shape and amplitude are clearly demonstrated for the uncertainties in the transducer diameter, assuming the two source velocity functions. These differences are listed in Table 4.3.1.

Type of source function	source diameter uncertainty	echo amplitude change	Echo shape change
Plateau	1%	+8%	slight
	5%	+100%	rapid
Sine envelope	1%	+54%	slight
	5%	+150%	rapid

Table 4.3.1: Changes in echo amplitude and shape of echo responses for 2mm-diameter target at a range of 35mm as a result of uncertainties in transducer diameter.

Figure 4.3.10 shows two sets of calculated echo responses for the same target size but at a constructive interference range (22mm). Generally the uncertainties in the transducer radius has no great effect on the echo response shape. However, the effects on the amplitude are noticeable. Again, these differences are listed in Table 4.3.2 below.

Type of velocity function	Source diameter uncertainty	Echo amplitude change	Echo shape change
Plateau	1%	-7%	negligible
	5%	-44%	negligible
Sine envelope	1%	-8%	negligible
	5%	-58%	negligible

Table 4.3.2: Changes in echo amplitude and shape of echo responses for 2mm-diameter target at a range of 22mm as a result of uncertainties in transducer diameter.

As can be seen in the above two tables, the uncertainties in the source diameter have greater effects when the target is at a destructive interference range. This arises because, for small targets the interference is between two nearly equal amplitude contributions. Also, a small change in the edge wave contributions will have a greater effect when there is destructive rather than constructive interference. The uncertainties discussed above are returned to in Section 4.4.4 when discussing the use of the present model to calculate DGS diagrams.

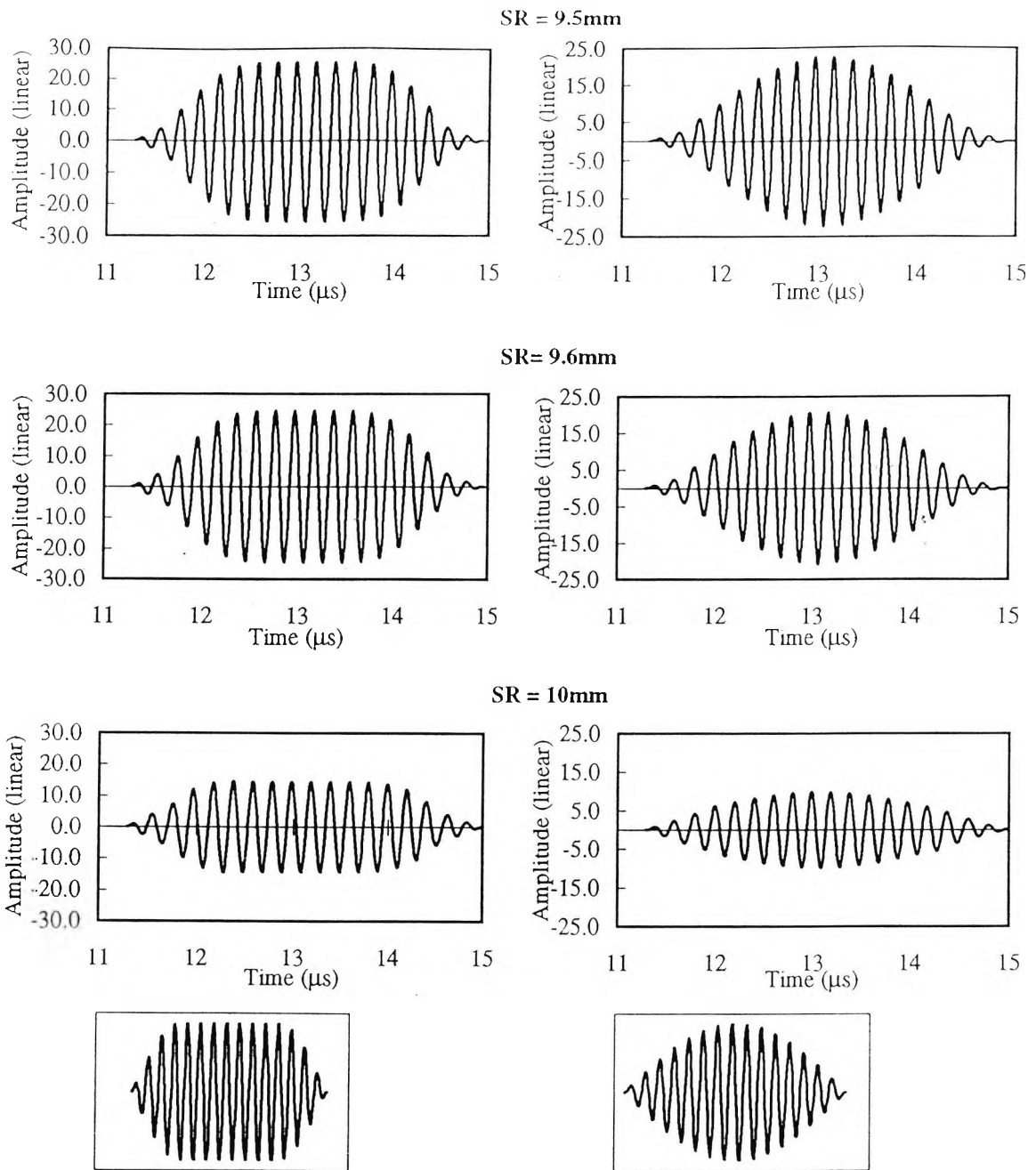


Figure 4.3.10: Two sets of echo responses for 1mm diameter target at a constructive interference range (22mm) obtained with different source radii (SR), excited with two different source velocity functions (at the bottom of each set).

4.4 New DGS diagrams for FBH targets in a solid medium

In the following Sections, experimental DGS diagrams for 2mm diameter FBH's at different ranges are compared with the corresponding calculated curves predicted by the model. The effect of the source velocity function on the diagrams is then considered before showing the way in which the method of amplitude detection affects the curves.

Since the DGS diagrams will be calculated out to ranges much greater than those considered so far, it is necessary to consider any implications for numerical accuracy. For targets at the near-field ranges considered so far, a 10ns time increment (δt) was fine enough to produce accurate pulse shapes. Numerical experiments showed that accurate predictions of echo pulse shapes could be made provided that

$$\delta t < \sim 0.05TD, \quad (42)$$

where the time difference TD is given by PD/c. When calculating DGS diagrams it would not be efficient if δt was set to conform with the greatest range considered since calculation time would be unnecessarily long in the the near field. To save time, δt is automatically calculated to approximately conform to the relationship of Eq (42).

In all calculated DGS curves shown in this section, the source characteristics are assumed to be a 19mm diameter transducer emanating a pulse (short or multi cycle pulse) centred at 5MHz, unless stated otherwise in the text.

4.4.1 Measured and calculated DGS diagrams for 2mm FBH targets.

Figure 4.4.1 shows sections of calculated and experimentally measured DGS diagrams for a series of 10, 2mm-diameter FBH's at ranges varying from 12mm ($PD = 2.1\lambda$) to 60mm ($PD = 0.47\lambda$) in an aluminium block. The experimental results were obtained using the same wide band, 19mm diameter, 4MHz transducer (Aerotech Alpha F08179) as used to obtain the short pulse echo responses given in Section 4.3.3. In order to obtain a good comparison between the measured and calculated diagrams, the modelling results were calculated with the theoretical

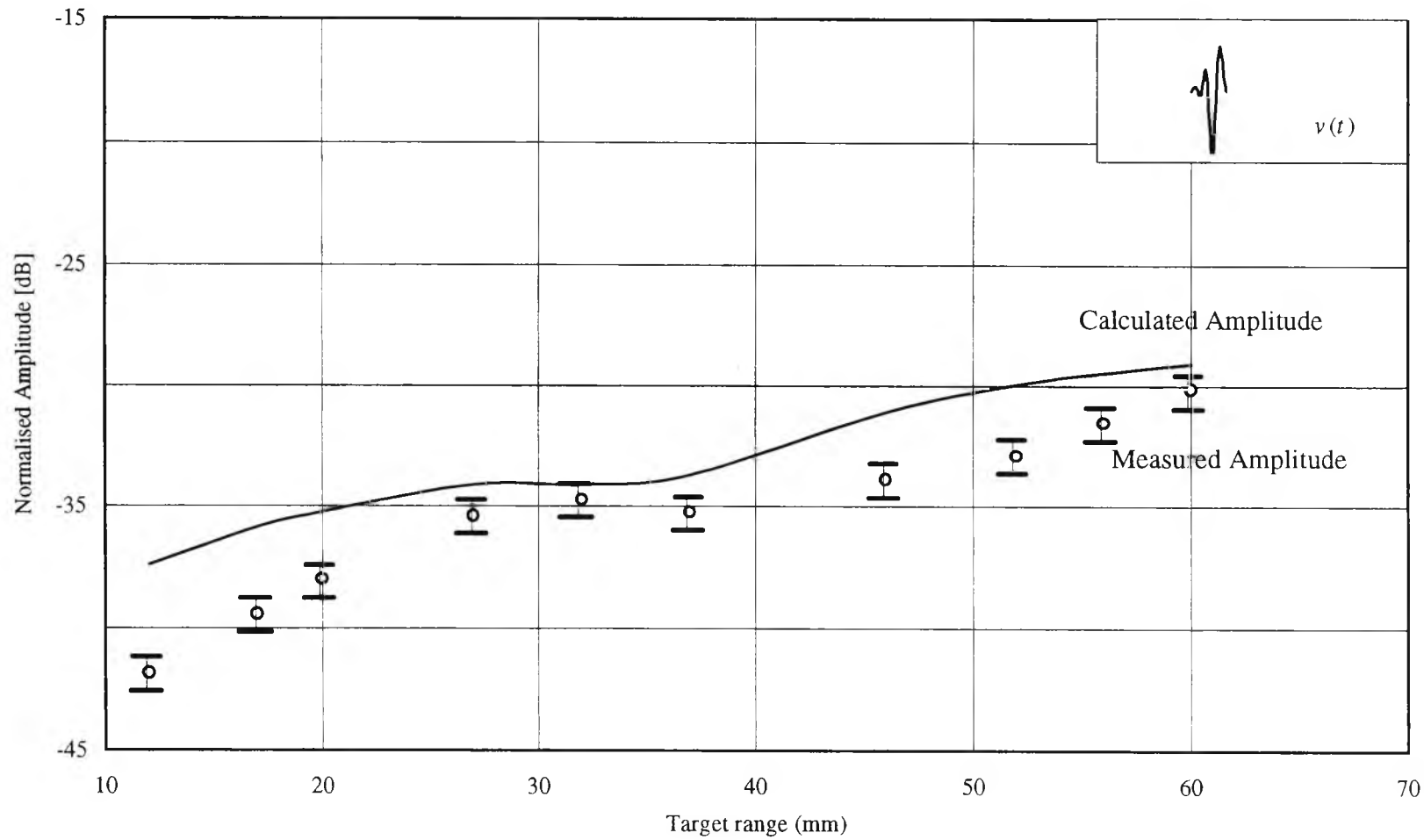


Figure 4.4.1: Calculated and Experimentally obtained DGS diagrams for 2mm diameter flat-bottomed holes in aluminium, positioned at several ranges from a 19mm diameter transducer excited with 4MHz pulse (shown inset).

source velocity function matched to that of the real transducer (see Sections 4.3.1 & 2). When measuring the velocity function, a time increment of 10ns was used. As was described earlier in Section 2.4, this increment may not be as required for the numerical calculations. Here we need to conform to Eq (42), and where necessary linear interpolation between the sampled data points was used.

In both sets of results, peak-to-peak echo amplitudes were taken and plotted using the same normalised scales as in the original DGS diagrams shown in chapter 2. Note however that the distance scale is now linear. The measured echo amplitudes were taken after digitally recording the echoes on the Lecroy 9410 oscilloscope, with sampling frequency of 100MHz. Note that the calculated *and* measured results may be plotted to the same relative amplitude scale, since they are separately normalised to their own echo amplitude for $G=1.0$.

In general, it can be seen that there is good agreement between the two curves, the maximum difference being about 4dB, bearing in mind the errors due to experimental uncertainties, such as machining tolerance, transducer positioning and coupling, as mentioned in section 4.1.

For the short pulse transducer used and over the near field as considered in Figure (4.4.1), it can be seen that the variations in echo amplitude with range are small. For example, the increase in the echo amplitude between 27mm and 47mm ranges is just 3dB. A similar effect was shown in section 4.3.3, where the echo responses themselves were given. However as was also demonstrated earlier (Figure 4.3.7) there will be fluctuations in near field echo amplitudes when a narrow band multicycle pulse transducer is used.

To demonstrate this, Figure 4.4.2 shows experimentally measured DGS diagrams obtained using the narrow-band 19mm Harisonic transducer to give a multicycle pulse centered on 3.8MHz (shown inset). A corresponding calculated curve is included for comparison. The band (23-63mm) of target ranges was chosen so that the PD varied from just over 1λ to just under $\lambda/2$, thereby including ranges where we move from destructive to constructive interference (of the compression wave components, see Figure 4.3.7). In both sets of results, peak to peak relative

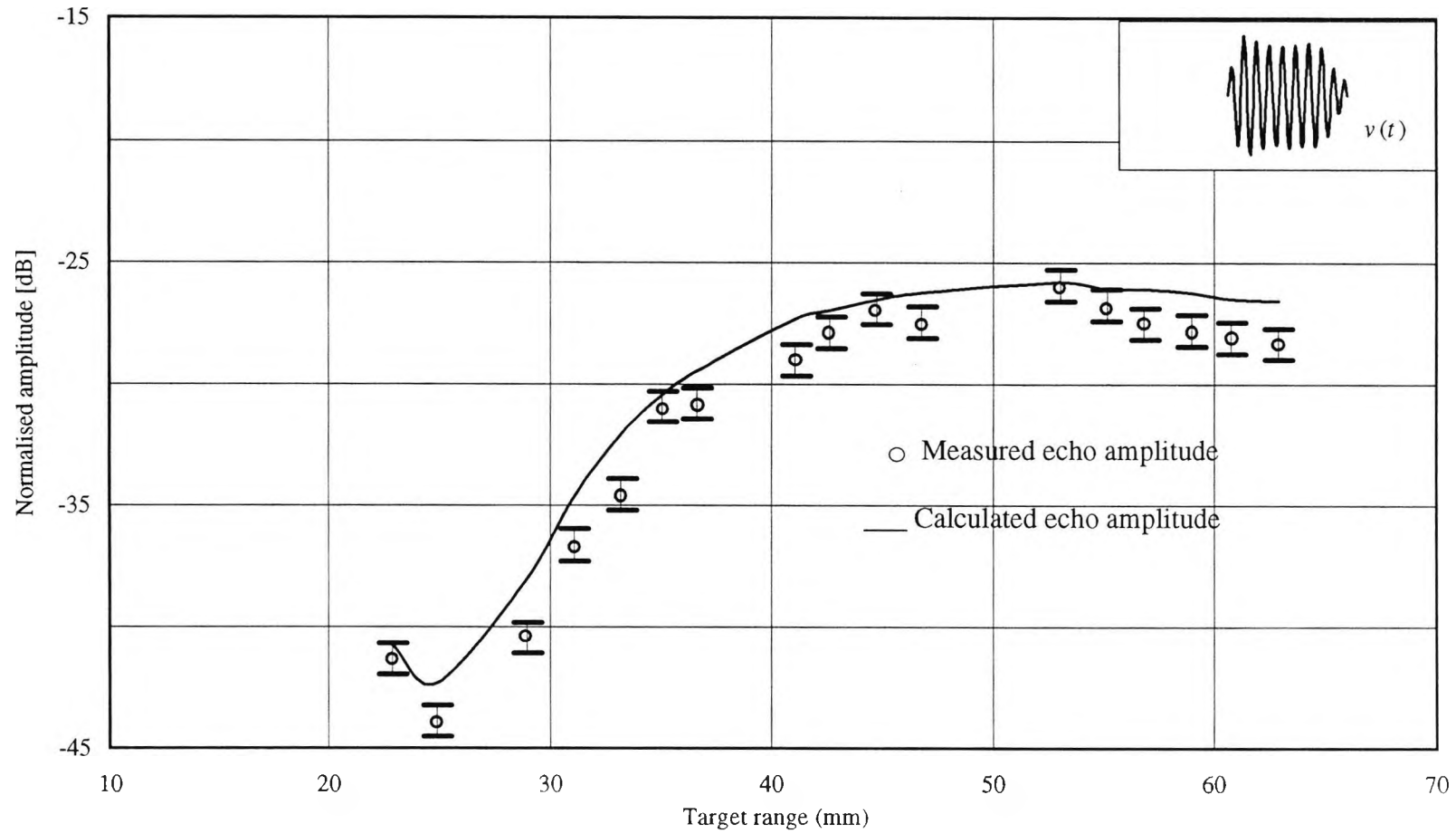


Figure 4.4.2: Comparison between Experimentally obtained DGS diagram and calculated DGS diagrams for 2mm diameter flat-bottomed holes in aluminium assuming a 19mm diameter transducer excited with a 3.8MHz multi-cycle pulse (shown inset).

amplitudes were taken and plotted using the same normalised scales as in Figure 4.4.1.

In general, there is good agreement between the calculated and measured results, shown in Figure 4.4.2, the maximum difference being about 3dB (or 4.5dB including the estimated error). In contrast to the relatively small change in amplitude with range with the short pulse results of Figure 4.4.1, there is now a variation of some 18dB as the range varies from 25 to 47mm.

It should be noted here that in both Figures (4.4.1 and 4.4.2) all the experimental points came below the calculated points. The reasons for such behaviour can be referred to several reasons. First of them is the coupling conditions at the moment of capturing the data. As mentioned before (section 4.1.1, p 60-61) if the couplant was not uniform all over the face of the transducer, the contribution of edge wave will be weak. Hence, the measured amplitude could be less than what it should have been if the couplant was uniform.

The second reason could be the roughness of the targets. As mentioned in chapter two, the model assumes the target to be smooth and planar. However, the experimentally available targets, have some roughness in their surfaces. This roughness causes more scattering of the beam. The combination of such effects causes the measured echo amplitudes for the targets to be smaller than those of the calculated ones.

Having shown that the model can predict the echo amplitude for targets over several ranges with reasonable accuracy, we may use it to investigate how various experimental conditions and uncertainties would affect DGS diagrams in general.

4.4.2 Effect of the source velocity function on DGS diagrams

In his original work Krautkramer (1959) mentioned the effect of the form of the ultrasonic pulse on DGS diagrams, especially in the near field region. In the present work, this effect is taken into account by changing the source velocity function. However, he did not fully explain this effect. In this section DGS curves are produced for various source velocity functions including both short- and multi-cycle pulses. The explanation for each set of curves is given.

Figure 4.4.3 shows DGS curves calculated for FBH targets assuming a single cycle, sinusoidal pulse (shown inset). These curves are presented in terms of the usual dimensionless parameters G and A (as defined by Krautkramer, 1959, section 2.3, p 36-37). As usual, the echo amplitudes for all targets at all ranges were normalised to the echo amplitude of a target which has the same diameter as the probe, at a range (25mm) within the near field of the probe.

As seen in Figure 4.4.3, for the smallest target ($G = 0.05$), there is a rise in echo amplitude with range for ranges up to about $1.5NF$. Up to $0.8NF$ there is a steady rise in amplitude. In order to explain this rise it is helpful to consider the detailed structure of some appropriate echo responses.

Figure 4.4.4 shows at the top both on-axis and 0.5mm off-axis impulse responses for a point target at 12 and 22 mm range. Beneath are shown the impulse responses of a finite target of radius 0.5mm together with the corresponding echo responses assuming a short pulse velocity function. From the upper results (a & b), it can be seen that the $P_c E_c$ component of the impulse response increases with range for targets both on- and off-axis. This increase stems from the way in which the mode conversion factor increases with range as explained in Section 2.2. However for the off-axis results (b), the increase is also because the $P_c E_c$ components are less smeared out with time at the longer range. Although both effects can still cause the rise in the $P_c E_c$ pulse when considering finite-sized targets, a more important effect comes in to play, as is demonstrated in the lower results (c & d)

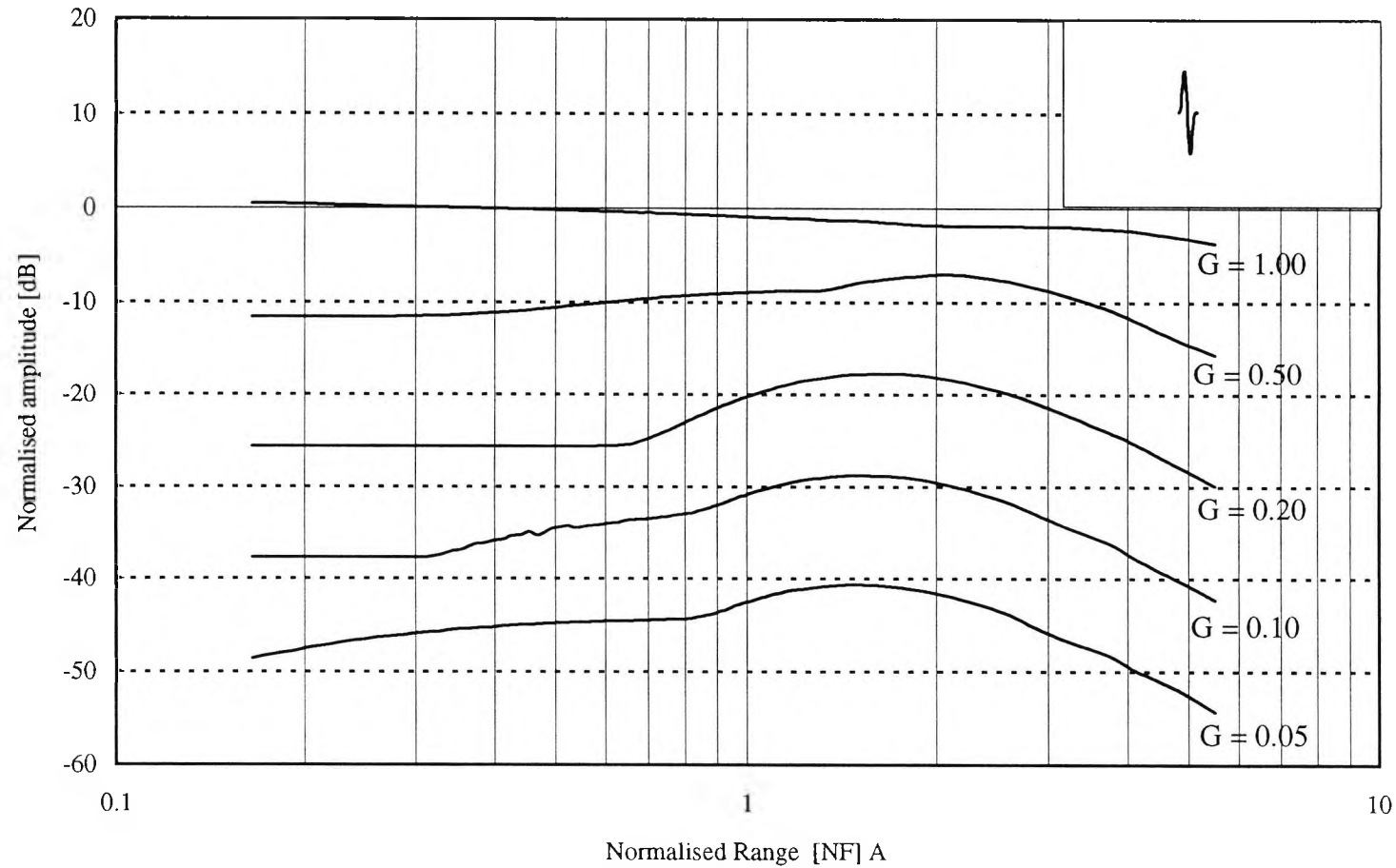


Figure 4.4.3: Calculated DGS diagrams using the new model assuming a 19mm diameter transducer excited with a 5MHz sinusoidal single cycle (shown inset). The echo amplitude is normalised to the echo amplitude of 19mm diameter target.

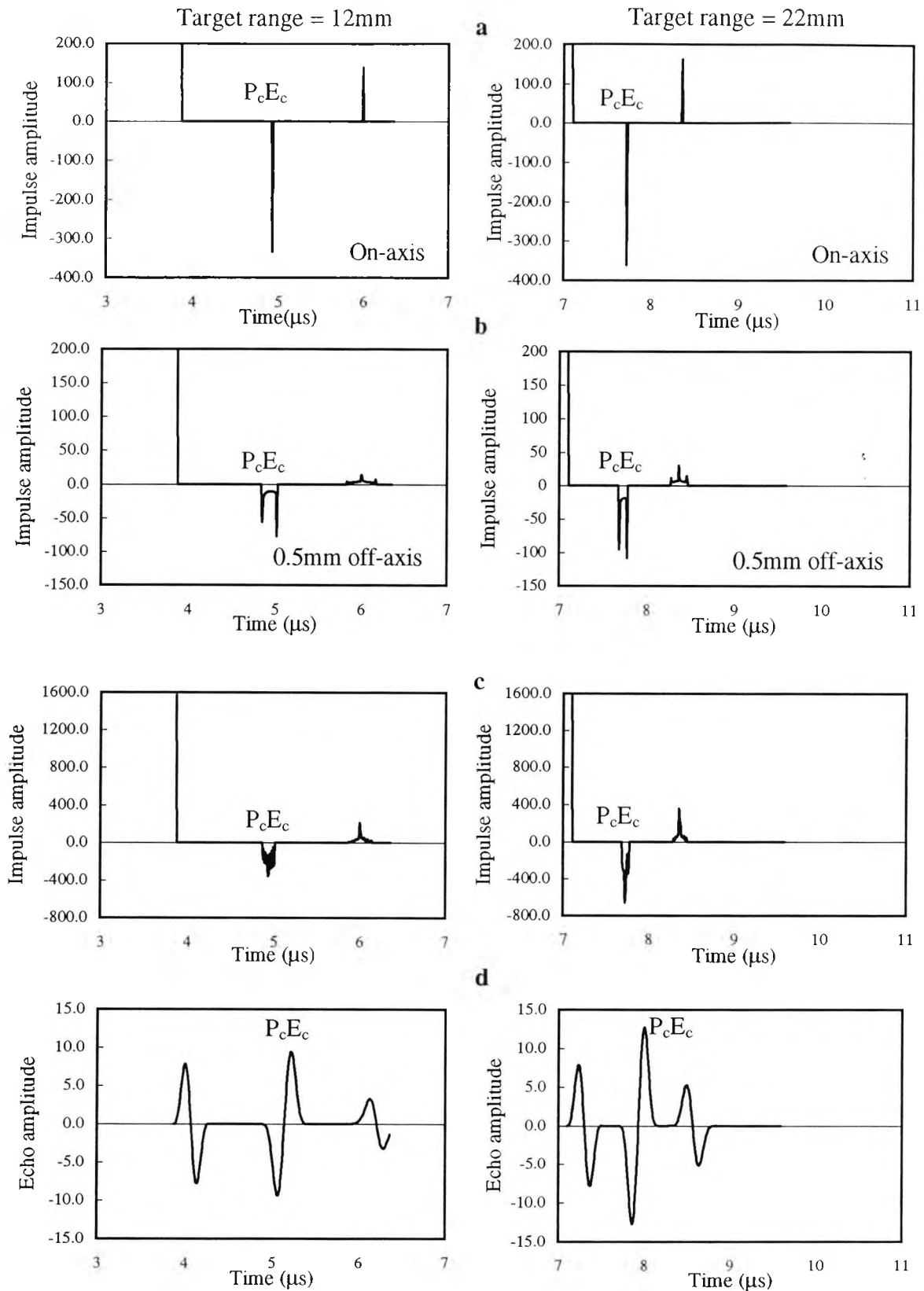


Figure 4.4.4: Impulse responses both on-axis and 0.5mm off-axis for a point target at 12 and 22mm range (a & b respectively). Impulse response (c) and echo response (d) for a 0.5mm radius target at both ranges.

for the 0.5mm radius target. The impulse response for a finite sized target is the sum of the contributions from all the elementary point targets that make its surface (see section 2.3 in Chapter 2). So, for a 0.5mm radius target ($G = 0.05$), the total $P_c E_c$ impulse response is the integration of the $P_c E_c$ impulse responses of point targets from on-axis to 0.5mm off-axis. In addition to the effects discussed above, since the off-axis contributions become more time compressed with range the integration will cause the total $P_c E_c$ impulse response for this target to increase with range, as shown in the lower result (c). For such a target size, this impulse response is the largest component of the total impulse response. When the total impulse response is convolved with the source velocity function, the amplitude of the $P_c E_c$ pulse increases. So even if there is no overlapping of components within the overall response (up to about $0.8NF$ corresponding to $PD > \lambda$) the echo response of this target will increase with range as demonstrated in result (d). It is this "integration effect" that causes the steady rise in amplitude with range (up to $0.8NF$) for $G = 0.05$ in the DGS curves shown in Figure 4.4.3. It should be mentioned that the integration effect will apply to DGS diagrams calculated using both the solid and fluid models, as will be demonstrated later in Section 4.5.

From 0.8 to $1.5NF$ range, there is a steeper rise in amplitude with range for $G = 0.05$. The reason for this rise in addition to that due to the integration effect is that the path difference between the plane and the edge waves becomes closer to $\lambda/2$ and hence they start to interfere constructively.

As discussed above, there is a rise in echo amplitude with range up to $1.5NF$ for small targets ($G = 0.05$). However, as G increases, different behaviour is observed in the curves. Consider the behaviour of the curve $G = 0.1$. Up to roughly $0.3NF$, the echo amplitude remains constant with range. The reason for this "flatness" in the plots, is that for this size of target the plane wave contribution becomes larger than that of the edge wave. As a result, when the peak to peak amplitude of the echo pulse is measured, the plane wave component ($P_c P_c$) will be the dominant factor in the total echo response, in contrast to the situation with smaller targets, where the $P_c E_c$ pulse is the dominant factor. Because the plane wave does not

change with range in a lossless medium, the echo amplitude will stay constant and hence the flatness in the curves. Beyond $0.3NF$ and up to $1.5NF$, the echo amplitude increases with range. Just as was the case for smaller targets, this is due to both the integration effect and the overlapping of the components within the overall response.

For $G = 0.2$, the distance within the near field, up to which the amplitude remains constant increases to $0.65NF$. Again, this is because as the target size increases, the plane wave component becomes more dominant.

From the progression of the $G = 0.1$ and 0.2 curves, it is expected that the echo amplitude will be constant over a larger range of distances for $G = 0.5$ curve. Interestingly, the range of distances at which the echo amplitude remains constant is less than that for $G = 0.2$, i.e. the amplitude remains constant up to just $0.4NF$ range and then rises. The unexpected rise in amplitude is because as the target size increases, impulse responses components corresponding to the edge wave become closer to the plane wave impulse response component. This is because the PD between plane and edge waves at the target periphery becomes smaller. Hence the separation between the components is less than the length of the source velocity function at ranges from $0.4NF$ onward. As a result, when the source velocity is convolved with the impulse response, overlapping between the corresponding echo pulses takes place. This overlapping between the pulses causes the rise in the peak-to-peak echo amplitude. Note also that this explanation is also valid for DGS curves constructed using the fluid models as will be seen in Section 4.5.

In the very far field, the echo amplitude decreases with range for all target sizes, the reason for this decrease in amplitude is that the plane and edge waves start to interfere destructively since the PD is now less than $\lambda/2$. As the range increases, the echo amplitude decreases and the echo amplitude becomes zero at infinite distance, where there will be complete destructive interference between equal amplitude components.

The above explanation for the form of short pulse DGS curves can also be used when considering curves calculated using a multi-cycle pulse. However, the multi-cycle curves show more fluctuations with range because the various components within the overall response now overlap over a much greater region of the field. Figure 4.4.5, shows theoretical DGS curves generated for FBH targets assuming a 15-cycle sinusoidal pulse (shown inset). Again, these curves are presented in terms of the usual dimensionless parameters G and A as mentioned earlier.

Because the compression edge wave contribution is strongest for smaller targets, the effects of interference between plane and edge waves on the echo amplitude are more evident than with larger targets. Such strong interference causes the large variations in echo amplitude with near field range. As the target size increases, the plane wave contribution becomes larger than that of the edge wave. As a result, interference effects on echo amplitude become less. This results in less fluctuations in the echo amplitude for larger targets.

Within the near field, there is good agreement between the general form of the curves given in Figure 4.4.5 and the original curves published by Krautkramer (shown in Figure 2.3.1), but it should be born in mind that his results were taken for disc-like targets in water and were not for exactly the same pulse shape. Also the new curves have the same general form as those given in the more recent work of Schmerr and Sedov (1989) and Sumbatyan (1994).

Despite the fact the new model gives similar DGS curve to those produced using fluid models (Schmerr and Sedov, 1989) there are some differences between these curves as explained later in Section 4.5.

In the far field, there is a linear reduction in amplitude with distance, as predicted by Krautkramer as well as by Schmerr and Sedov and Sumbatyan.

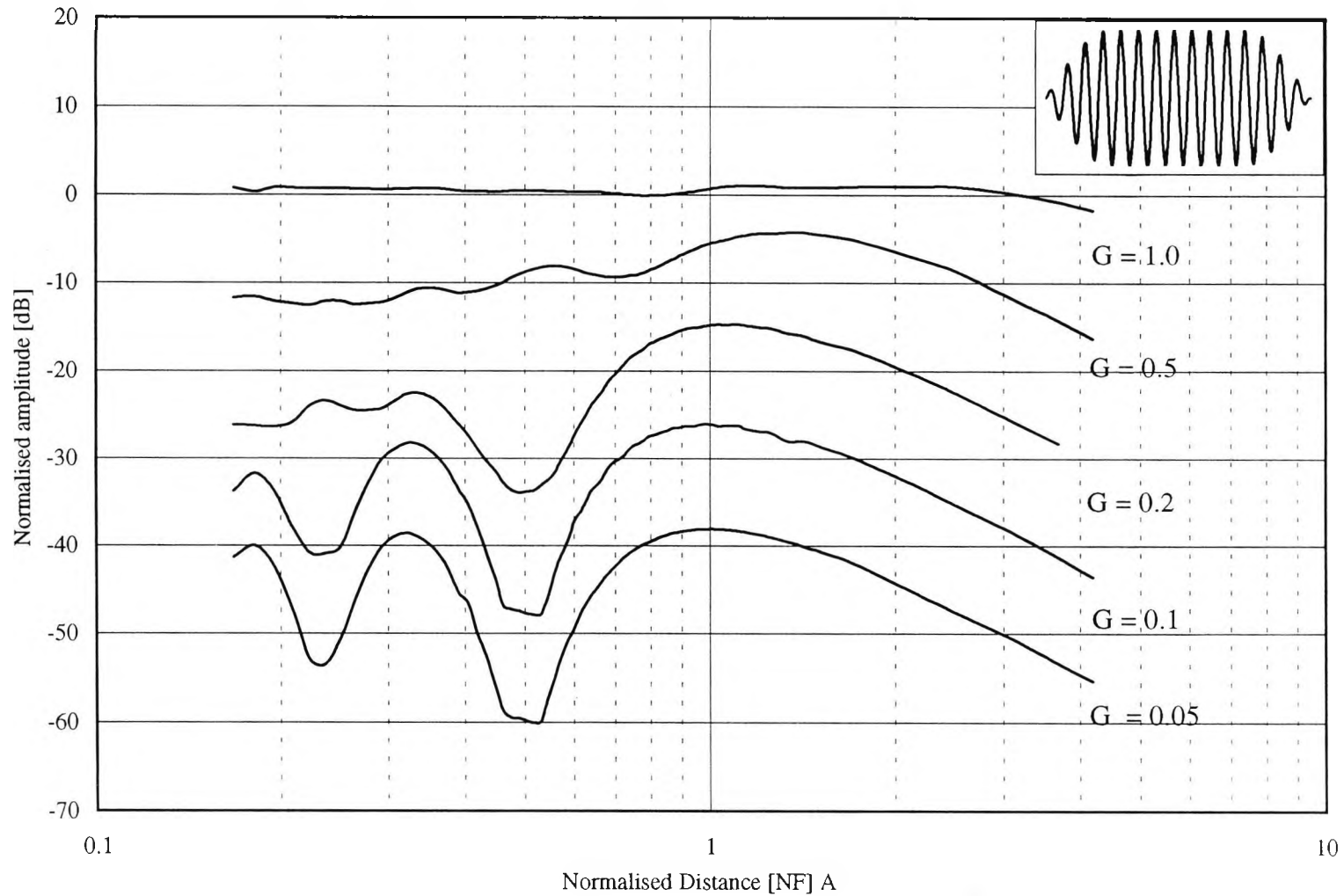


Figure 4.4.5: DGS diagrams calculated using the solid model assuming a 19mm diameter transducer excited with 5MHz 15-cycle sinusoidal pulse (shown inset).

One point which is noted from the curves of Figure 4.4.5 is that, for small values of G (0.05 and 0.1), the variation in amplitude from 0.5 to 1 NF distance is more than 20dB. This variation can be one of the greatest drawbacks in sizing small defects using the DGS method. A similar variation was shown in the measured waveforms of the 2mm diameter target, where the echo amplitude at 47mm is nearly 10 times bigger than the echo amplitude at 25mm (Section 4.3.3). With larger targets ($G = 0.5$ and 1.0), this particular drawback is less of a problem due to the domination of the echo response by the plane wave, as explained in section (4.3.2).

Note when using the present model to calculate DGS diagrams, it is not necessary to calculate the whole echo response including the shear-wave components, provided that their effect on the compression edge-wave components (within the C packet) *is* included. As mentioned earlier in Section 2.3.3, the shear wave amplitude is always smaller than that of the compression wave within the ranges shown in Figures 4.4.3 and 5. Hence, when just the overall amplitude of the response is required, as in DGS curves, the shear edge wave contribution can be truncated, thereby reducing calculation times by a factor of around ten times. Using the truncated responses, the time to carry out the calculations made in producing the curves shown in Figure 4.4.5 was approximately 2 hours on a 486DX PC.

So far in this section, the considerable differences between DGS diagrams produced using short and multi-cycle pulses have been demonstrated and explained. In practice, when sizing defects using DGS diagrams there are times when the effect of smaller changes in pulse shape are required. For instance when changing transducers of nominally the same type and centre frequency.

Figure 4.4.6 shows two sets of DGS diagrams produced assuming that the velocity function was two variants of a multi-cycle pulse (shown inset). The two functions are the same as used earlier in Section 2.4. They have the same centre frequency (5MHz) and number of cycles (15), but different envelopes.

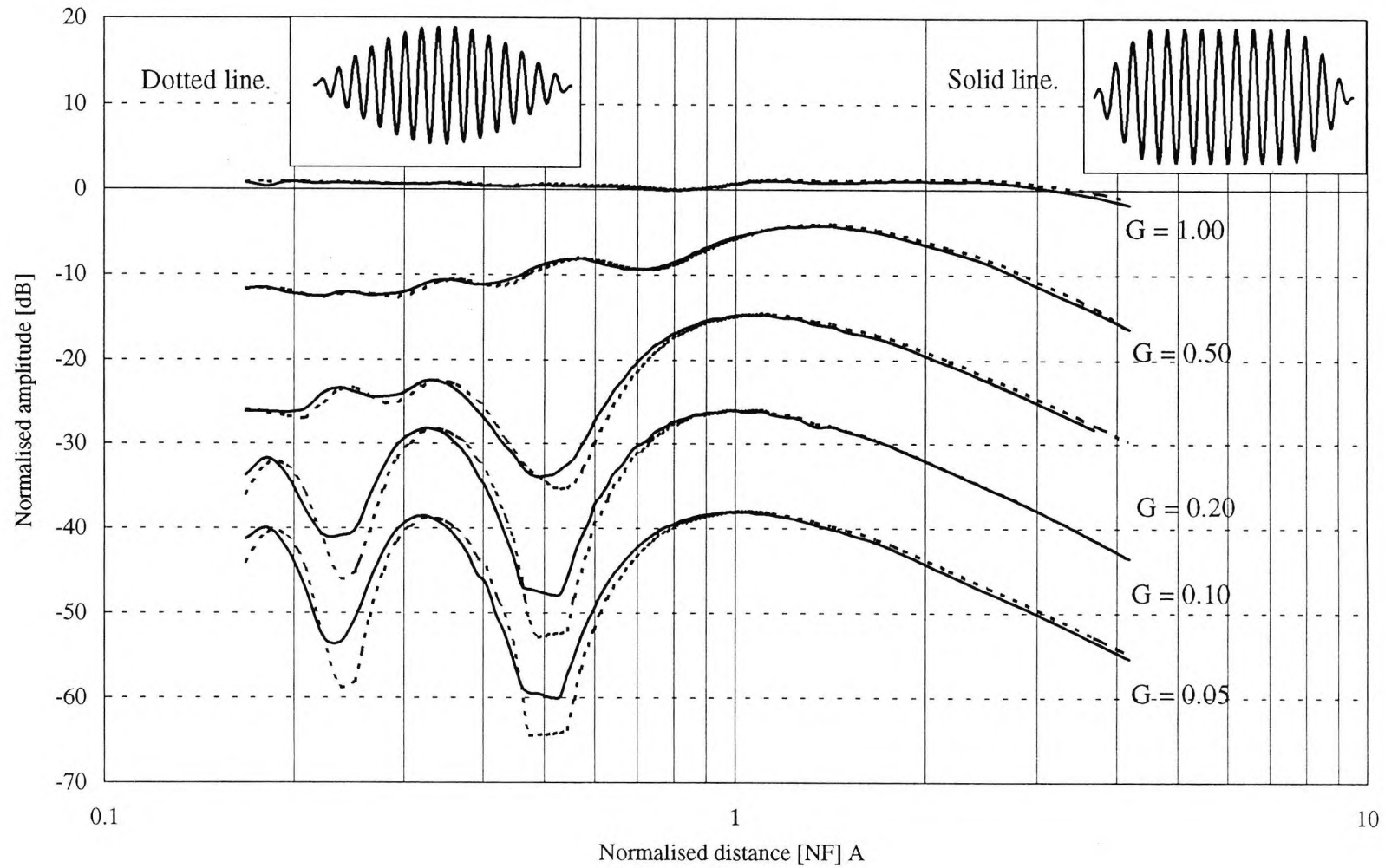


Figure 4.4.6: Comparison between two DGS diagrams constructed using different velocity functions (shown inset).

At certain ranges in the near field, it can be seen that for small targets, there are some differences between the relative echo amplitudes using the two functions. As can be seen, the differences are greatest at destructive interference ranges, - $0.25NF$ ($PD= 2\lambda$) and $0.5NF$ ($PD= \lambda$). As an example at $0.5NF$ and for $G = 0.05$, the difference in relative echo amplitudes using the two functions is 6dB. This difference is because at a destructive interference range, the plane and edge waves are *subtracted* within the steady-state region of the echo pulse. Where the two overlapping components are of similar size, the overall peak-to-peak echo amplitude is likely to be that of the *transient* region of the echo response (see Figure 4.3.2). The transient regions for the echo responses are not the same because the source velocity functions are different. The plane and edge waves are of similar sizes, hence small changes in any of these sizes produces large changes in the total pulse shape. The combined effects of subtracting two equal quantities and different envelope functions causes the discrepancies in echo amplitude.

At ranges other than those where destructive interference occurs, the differences in echo amplitude using the two functions are much smaller, this is because the echo amplitude is a measure of the height of the *steady* state region of the echo pulse. When the plane and edge waves that have similar sizes are *added* at these ranges, the different rising and decaying times of the velocity function will have small effect on the total echo amplitude.

The difference in amplitude becomes less as G increases at the same range. Beyond $G = 0.5$, the amplitudes are virtually the same because as mentioned earlier, the echo response is dominated by the plane wave component.

In summary, the shape of the DGS curves in the near field region depends very much on the source velocity function. For a short pulse, there is a constant or/and continuous rise in the echo amplitude (depending on the target size) with range. For multi-cycle pulses, there are fluctuations in the echo amplitude with range, that decrease as the target size increases. Also, using two different multi-cycle source velocity functions can cause some significant differences in echo amplitude even for quite similar driving functions. These differences occur for targets that are up to

half of the transducer diameter. Note that this only happens when the target is at a destructive interference range within the near field. At other ranges, the excitation pulse can make small or no differences on echo amplitude measurement

In the far field, the shape of the DGS curves is the same for both short and multi-cycle pulses.

4.4.3 Effect of the method of amplitude detection on DGS diagrams.

Figure 4.4.7, shows two sets of theoretical DGS diagrams produced assuming a 19mm diameter source excited with a 5MHz 15-cycle pulse. One set is produced by taking the peak-to-peak amplitude of the echo responses (as has been done throughout, so far). The other is produced by calculating the mean of the absolute values of compression packet C at each range for each target size.

In the near field of the source and for small values of G ($G = 0.05$), the main differences in echo amplitude using the two methods are clearly seen at a (destructive interference) range of $0.5NF$ where $PD=\lambda$. There is a difference of about 4dB between the two methods. The reason for the relative amplitude of the echo response of the target using the peak to peak method being higher than that using the mean value method, can be explained by referring to the echo pulse shape themselves as shown in Figure 4.4.8. The Figure shows calculated echo responses for 1mm, 4mm and 19mm diameter FBH's at 35mm range assuming the same source parameters used to obtain the DGS curves shown in Figure 4.4.7. At this destructive interference range, the echo response for the small target ($G = 0.05$) is small compared to that of echo response for the larger target ($G = 1.0$) using the two methods. However, the null region in the echo response causes the mean of the pulse to be very small. Hence, when the echo response is normalised to the mean of the larger target ($G = 1.0$), its mean will be less than the peak-to peak amplitude.

As the target size increases the plane wave contribution will be larger than that of the edge wave. So, at the same range, interference effects on the echo response

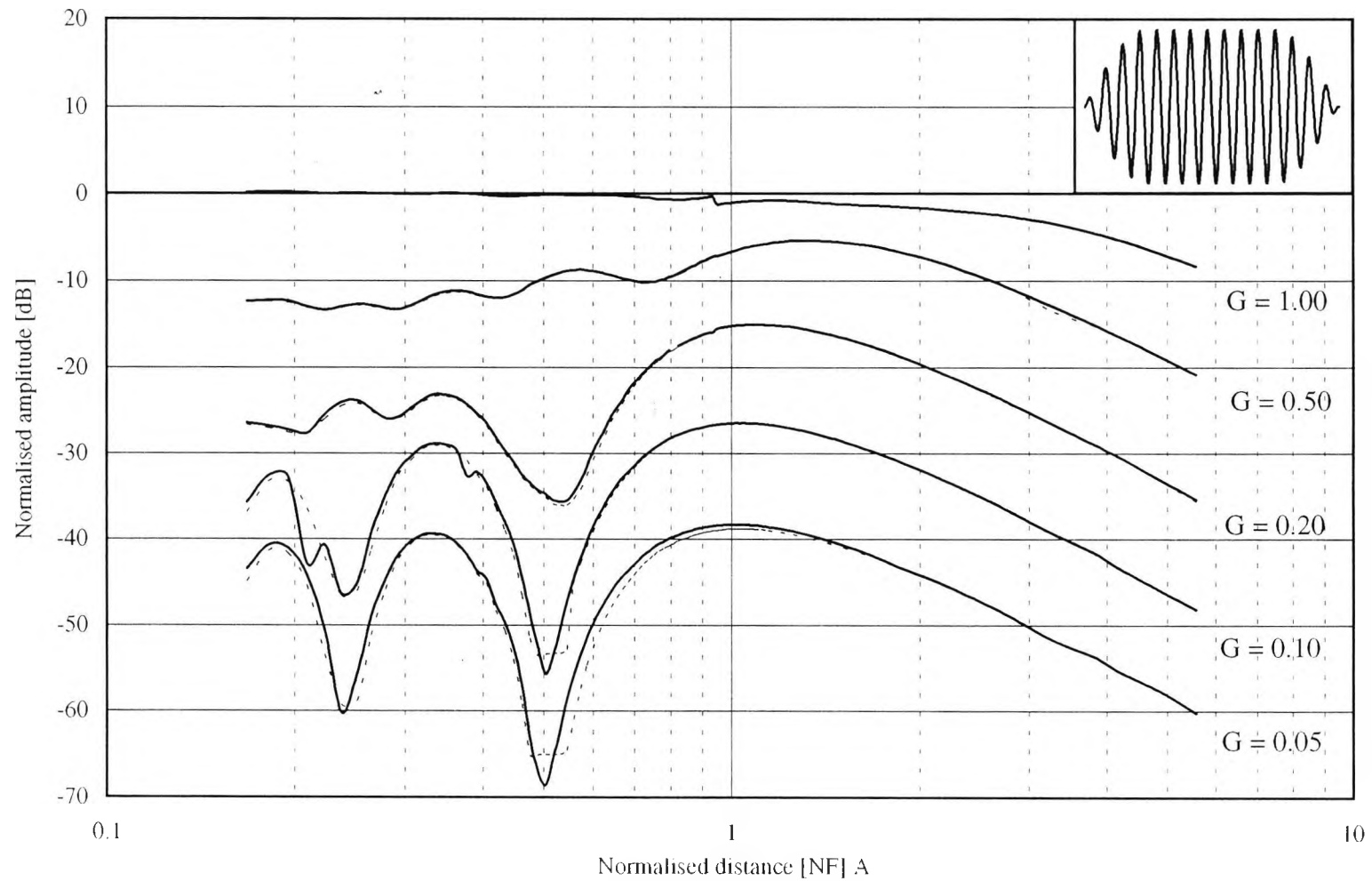


Figure 4.4.7: Calculated DGS diagrams using two different methods of amplitude detection, one is peak to peak (the dotted line), the other is the mean of the pulse (the solid line) assuming a 19mm diameter transducer excited with a 5MHz, 15-cycle pulse (shown inset).

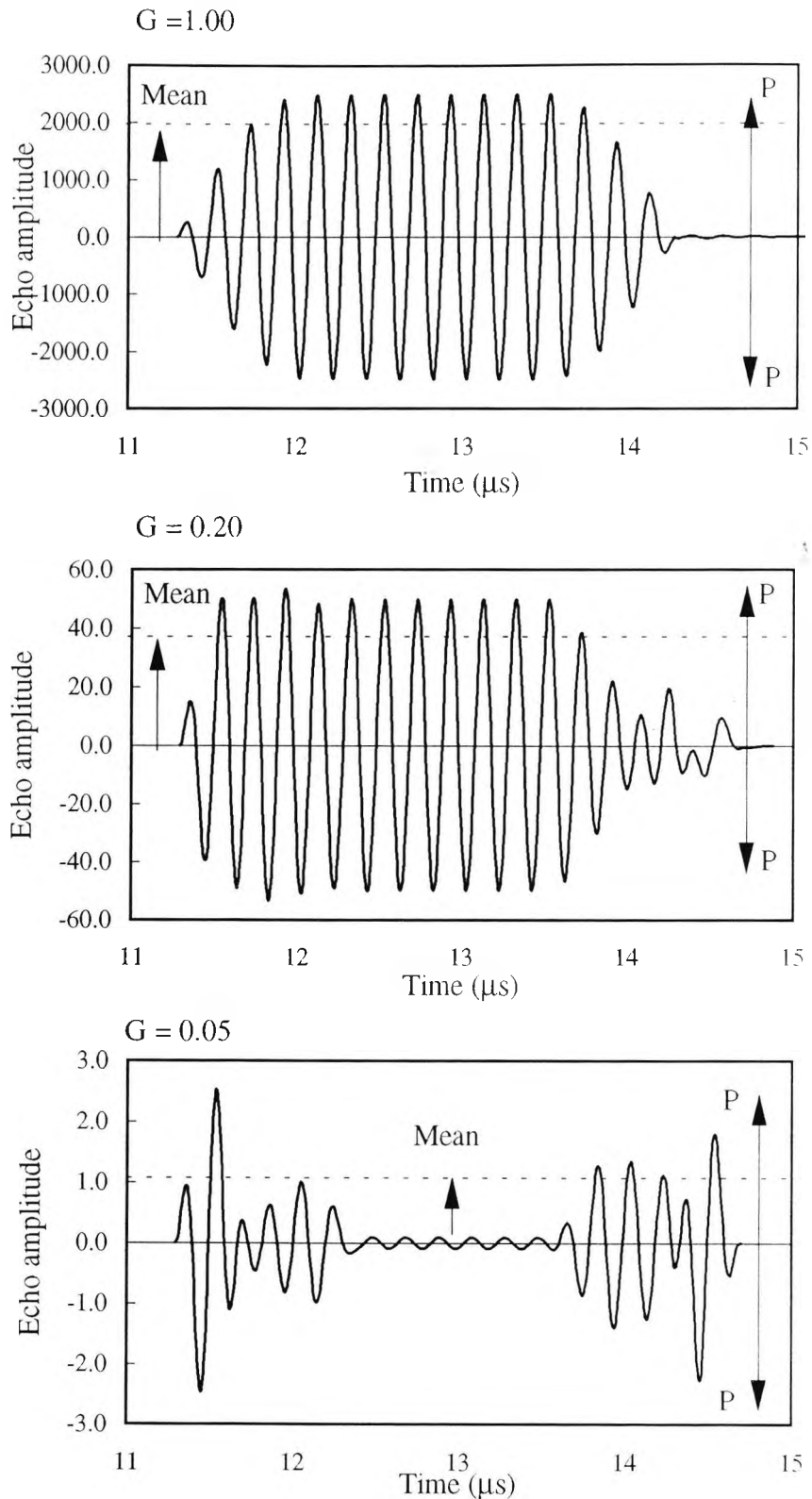


Figure 4.4.8: Calculated echo responses for 1mm ($G = 0.05$), 4mm ($G = 0.20$) and 19mm ($G = 1.00$) diameter FBH's at a range ($\sim 0.5\text{NF}$) which represents a minimum at the DGS curves shown in Figure 4.4.7. The height of the dotted line represents the mean of the absolute values of the pulse. The two headed arrow represents the peak-to-peak (p-p) amplitude.

will be small and the null region disappears. This results in increasing the mean of the pulse. Hence, when the echo response is normalised it is nearly the same using both methods. This is clearly demonstrated in Figure 4.4.8 for the 4mm ($G = 0.2$) target.

At other ranges within the near field, the differences are considerably smaller using the two methods, since at such ranges, interference effects on the echo response will not cause rapid changes in the echo shape.

In the far field, for small and large values of G , there are negligible differences in echo amplitude using the two methods, since again the plane and edge waves partially overlap and hence the normalised echo amplitudes for both methods are nearly equal.

4.4.4 Effect of transducer radius on DGS curves.

In section 4.3.4, the effect of uncertainties in the source diameter on the echo pulse shape was investigated. In this section, the effect of such uncertainties is extended to the DGS curves.

Figure 4.4.9 shows two sets of calculated DGS curves. One set is produced assuming a source diameter of 20mm. The other set is produced assuming a 5% uncertainty in the source diameter (19mm diameter). For both sets of curves, the source velocity function consists of 15 cycles centred at 5MHz.

At short ranges there are significant differences between the two curves, especially for small targets. For example, within the near field of the source and for $G = 0.05$, the difference in echo amplitude can be as much as 10dB. The reason for such differences is that the edge wave contribution is strongest for such sizes. As a result, any miscalculations in the source transducer and hence the PD between these waves and the plane wave will produce dramatic differences in the predicted echo amplitudes.

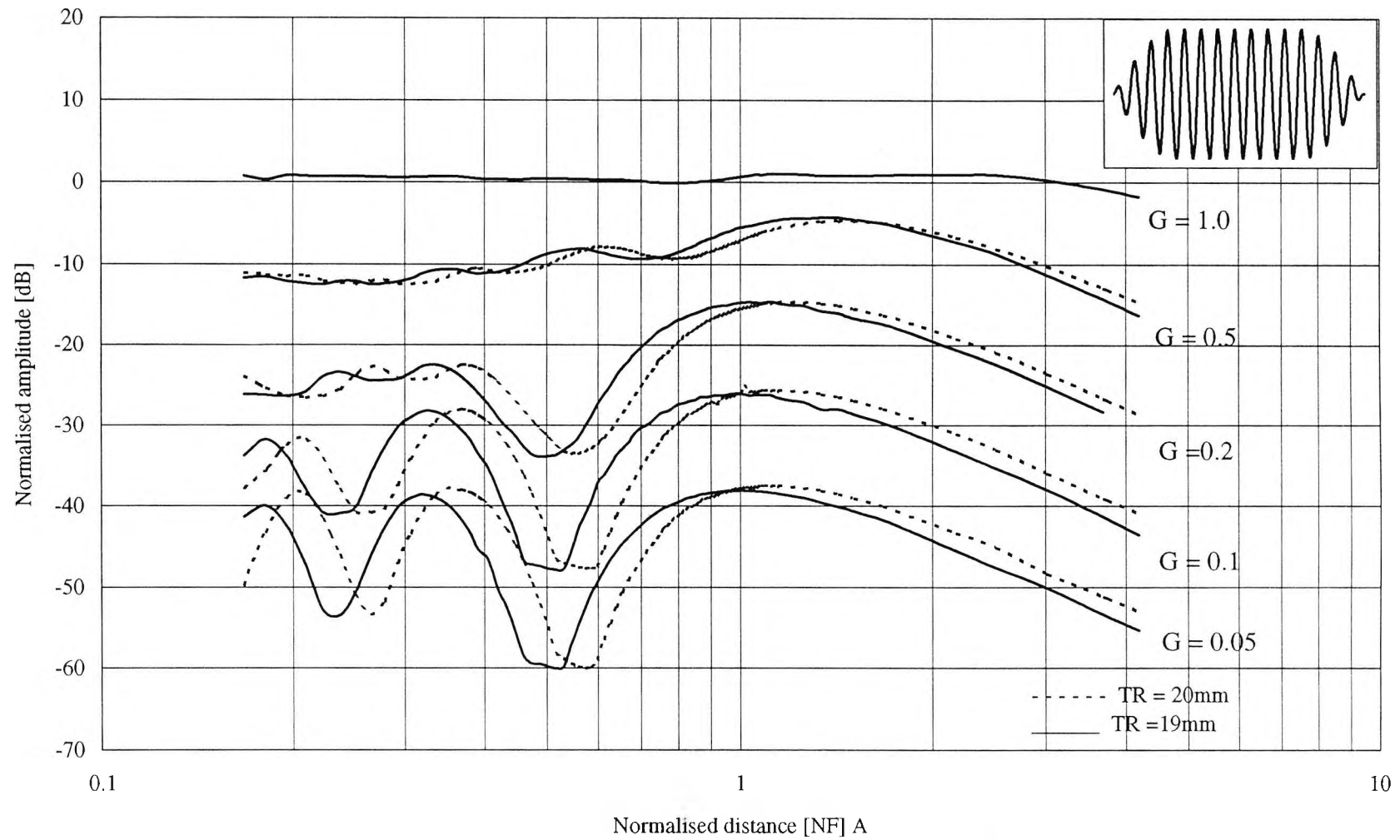


Figure 4.4.9: DGS curves calculated assuming uncertainty in the transducer radius. TR stands for transducer radius.

As the target size increases, the differences in the echo amplitude becomes smaller. For $G = 0.5$ the differences in amplitude are less than 1dB for all ranges within the near field of the source. This is because as explained in Section 4.3.2, the echo response is dominated by the plane wave and hence any miscalculations in the PD will have very small effect on the predicted echo amplitude.

In the far field, for small and large targets, discrepancies in echo amplitudes become less with range since the PD is less sensitive to changes in range. Hence, uncertainties in the source diameter will have only a small effect on the echo response.

4.5 Comparison between DGS diagrams calculated using the solid and fluid models

As mentioned in section 4.4 there are some differences between curves produced using the fluid and solid models. In order to show these differences, a comparison between diagrams produced using the new solid model and diagrams produced using an earlier fluid model (McLaren and Weight, 1987) is introduced. The comparison is made for short and multi-cycle pulse sources, respectively.

Earlier in Figure 4.4.1, a DGS curve calculated using the solid model was compared with an experimental DGS diagram for a 2mm target. These results are repeated here in Figure 4.5.1, but with a further curve calculated using the fluid model. As can be seen, the solid model gives a DGS diagram closer to the experimentally obtained result than does the fluid model, taking into account the systematic differences between the measured and calculated curves mentioned in section 4.4.1. An explanation for the higher amplitudes predicted by the fluid model is given below, after further comparisons between the two models are made.

To extend the comparison, Figure 4.5.2 shows a number of DGS curves produced using both the fluid and the solid models. Throughout, the source velocity function is a single cycle sinusoidal pulse centred at 5MHz (shown inset).

Before going into the comparison between the curves, it should be pointed out that the normalisation of the curves has no effect on the differences between the curves. Since both sets of curves are normalised to the echo amplitude of a target that has the same diameter as the source ($G = 1.0$) positioned at a range within the near field of the source. From Figure 4.5.2, for such targets, echo amplitudes are equal within the near field of the source, whatever model is used.

For small targets ($G = 0.05$), there is rise in the echo amplitude with short ranges for both models. As mentioned earlier in section 4.4.1, this is due to the integration of the echo impulse responses over the target surface. However, the echo amplitude given by the fluid model is slightly higher than that obtained using

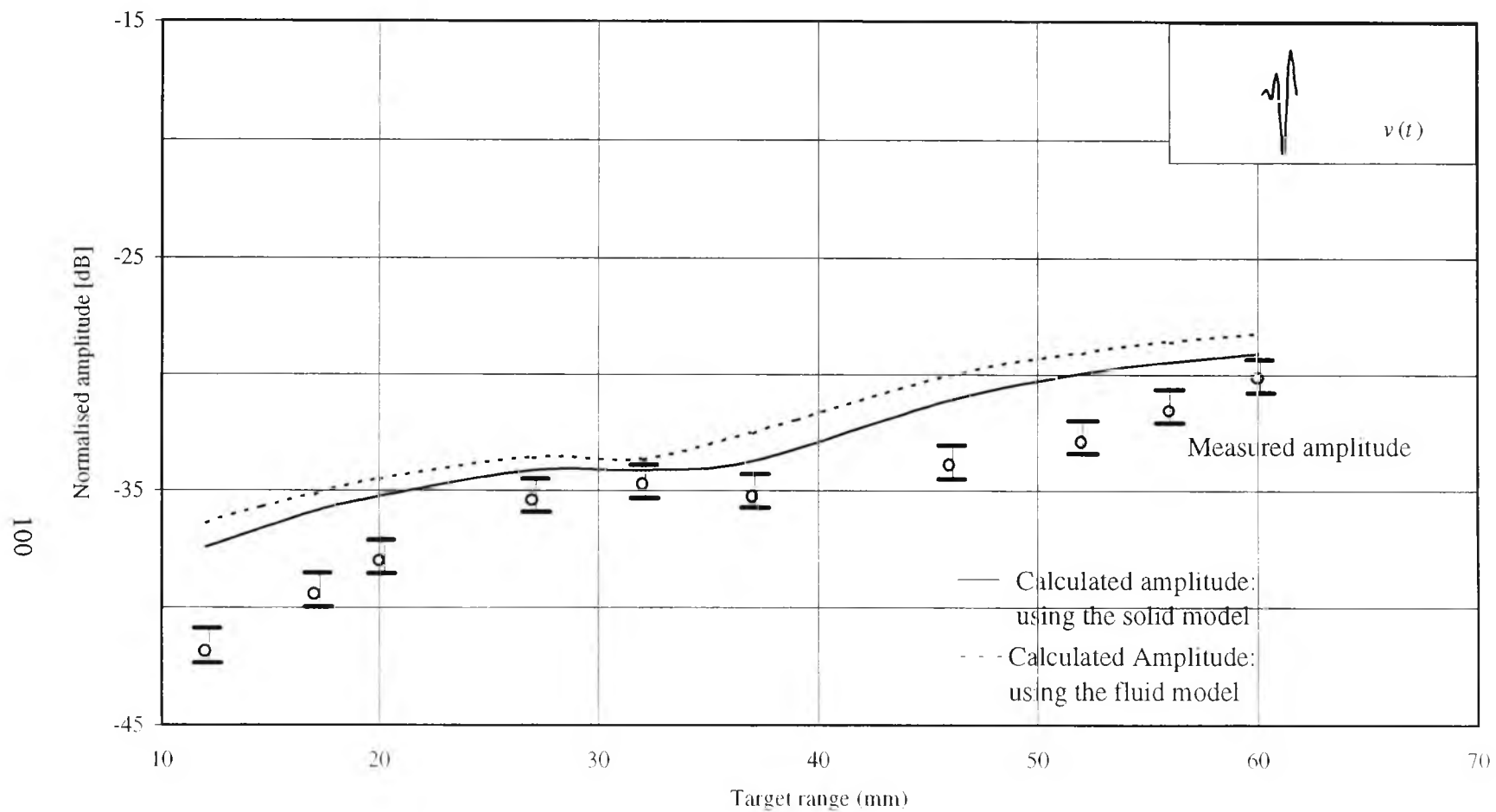


Figure 4.5.1: Comparison between experimentally obtained DGS diagrams for 2mm Diameter flat-bottomed holes in aluminium and calculated DGS diagrams using the fluid and the solid models, using a 19mm diameter excited with a 5MHz short pulse (shown inset).

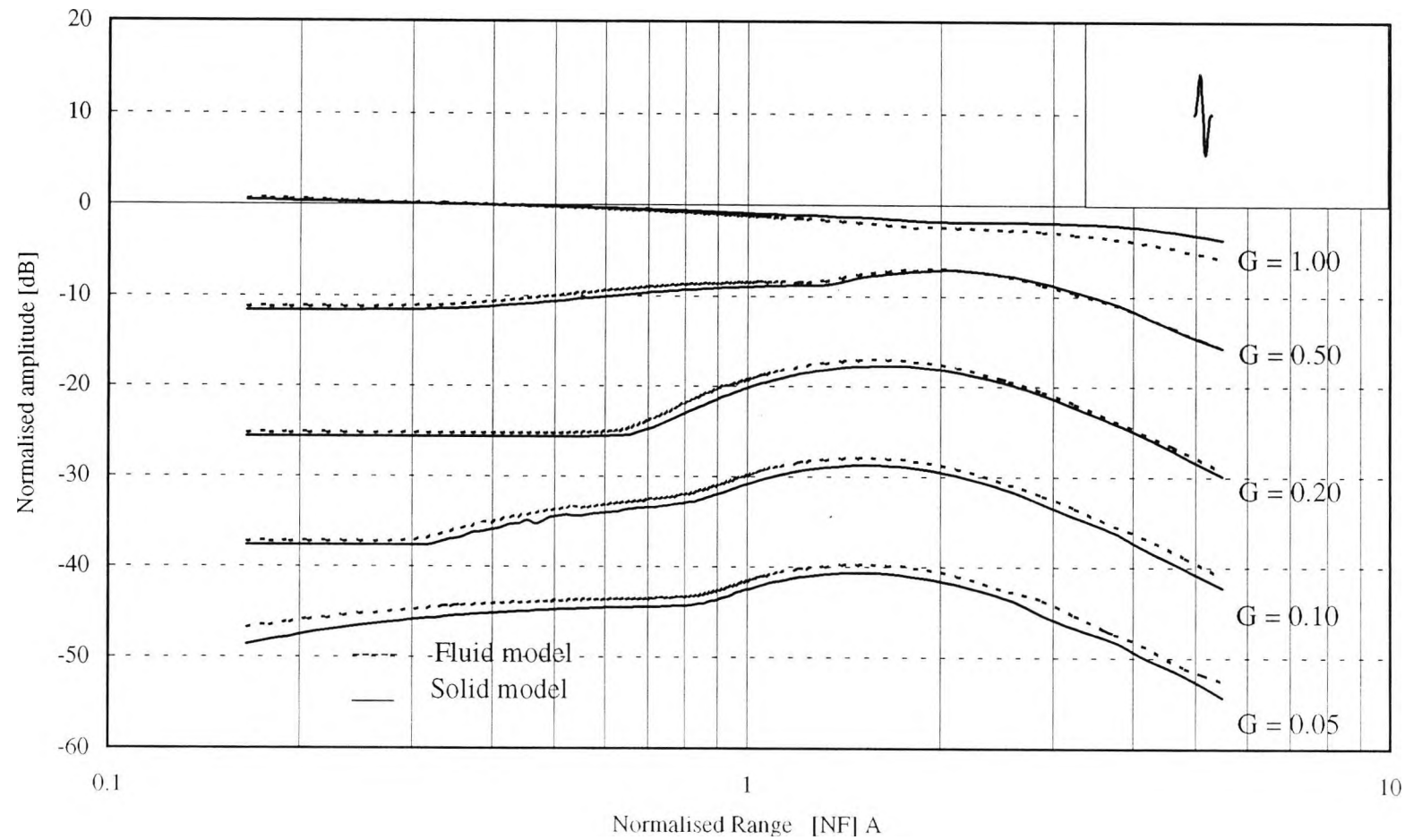


Figure 4.5.2: Comparison between DGS diagrams for FBH's calculated using the fluid and the solid model, assuming a 19mm diameter transducer excited with 5MHz single sinusoidal pulse (shown inset).

the solid model, especially at shorter ranges. This stems from the fact that in the solid model, part of the compression edge wave is converted to a shear edge wave, and so the compression packet C decreases in amplitude. Because this effect is much stronger at the short ranges, the difference in echo amplitudes using the two models is slightly bigger there. As the target size increases, the difference in echo amplitudes using the two models becomes less. This due to the domination of the echo response by the plane wave, with increasing target size.

With multi-cycle pulses there are also differences in the echo amplitudes using the two models. Figure 4.5.3 shows a comparison between the measured multi-cycle DGS curve for a 2mm target (shown in Figure 4.4.2) and calculated DGS curves using the two models. Again, this figure shows clearly that the solid model gives a predicted DGS diagram closer to the experimentally obtained DGS diagram than does the fluid model.

Again, with multi-cycle pulses, the comparison between the two models is extended theoretically to more target sizes and more ranges, as shown in Figure 4.5.4. As shown in the comparison with the measured DGS curve in Figure 4.5.3, for small targets there are some differences between the two sets of diagrams, especially at destructive interference ranges within the near field region. As an example, For $G = 0.05$ and at $0.5NF$ range, the fluid model would give a larger amplitude for small targets than does the solid model by some 6dB. These differences are relatively high compared to the differences shown in the case of DGS curves constructed assuming short pulse sources. As G increases, in general the differences in echo amplitude using the two models become smaller.

From Figure 4.5.4 it can be seen that within the near field region, at two destructive interference ranges (i.e. $0.25NF$ and $0.5NF$) the differences between the models vary. At other ranges, within the near field, the differences between the models are relatively the same. This stems from the fact that in the solid model the compression edge wave contribution within the C packet varies with range. So, at two destructive interference ranges, the subtraction between two nearly equal

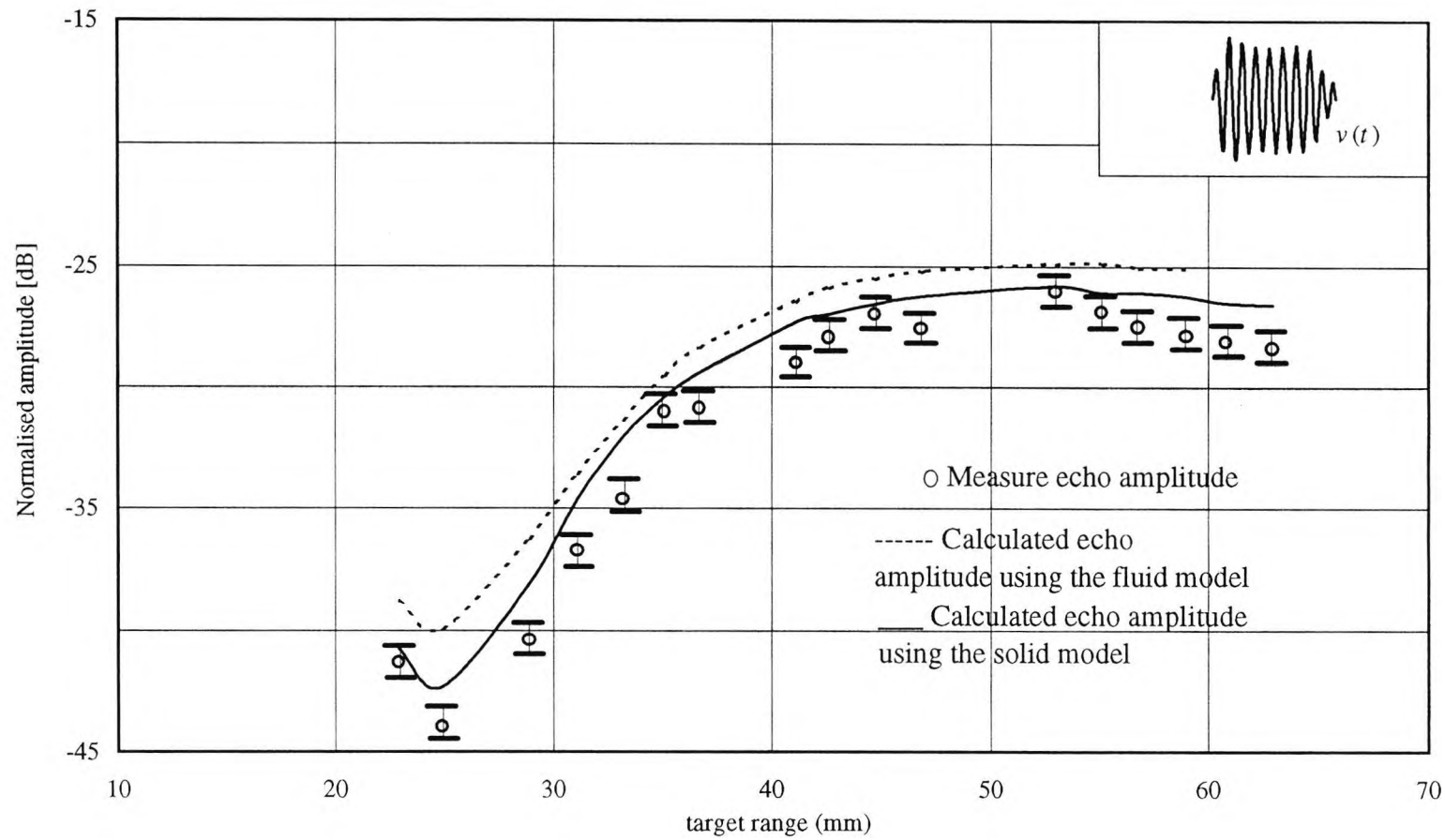


Figure 4.5.3: Comparison between Experimentally obtained DGS diagram and calculated DGS diagrams using the fluid and the solid models for 2mm diameter FBH's, using a 19mm transducer excited with 3.8MHz multi-cycle pulse (shown inset).

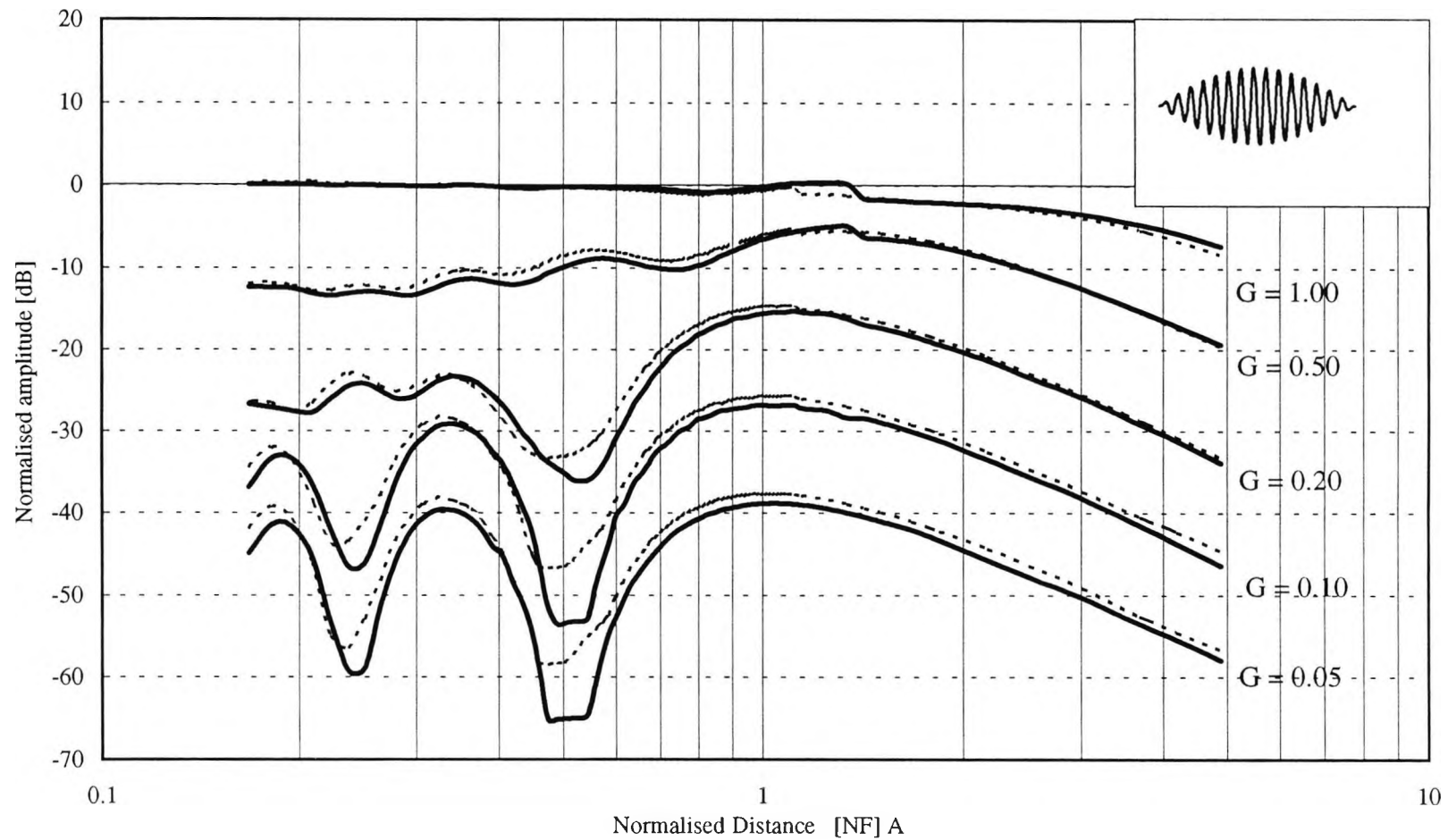


Figure 4.5.4: Comparison between DGS diagrams constructed using the solid model (Solid line) and the fluid model, (Dotted line) assuming a 19mm diameter transducer excited with 5MHz 15-cycle sinusoidal pulse (shown inset)

components, as mentioned in section 4.4.2, (The plane and edge wave) produces larger differences when one component slightly changes. At other ranges, when one component changes slightly small errors are produced when the two components are added.

An important conclusion that can be drawn from the above comparison between the two models is that, the use of the fluid model to estimate a target size at the destructive interference range might result in giving the impression of the existence of a target that is two times larger than its real size.

For large values of G , i.e. $G = 0.5$ and 1.0 ., at all ranges, there are no noticeable differences in the echo amplitudes using the two models. since for larger targets the contribution of the edge waves is much smaller than that of the plane wave. This implies that the fluid model can be used to estimate the size of large targets in solid medium.

As a result of the differences noted in construction of the DGS diagrams, using the fluid and solid models, it is suggested here, that some correction factors are added to the DGS diagrams constructed using the fluid model and used to estimate target sizes in solid. It should be noted that these correction factors, should be calculated for each transducer when applied to the same testing material, since both pulse shape and the near field are characteristics of the source.

Some authors (Schmerr and Sedov, 1989), argued that their fluid model can be used to predict echo amplitude of targets in solid medium, with either small or large targets, because they considered that the existence of the shear waves has negligible effect on the echo wave-forms of the targets. Other people, (McLaren and Weight, 1987), argued that using the fluid model to predict the echo amplitude of targets in solid medium could give some errors in the estimation of the target size, especially for small values of G . For larger values of G , they argued that there are no differences in estimating the size of large targets in solid using the fluid model.

This work has shown that there are differences between the two models in estimating the target size, especially for small targets, at certain ranges within the near field when multi-cycle pulse is used. This would support the argument of McLaren and Weight that care should be taken when estimating target sizes in solid using a fluid model. When short pulse is used, the fluid model can be used to estimate small and large target sizes in solid medium if the small differences reported in this thesis are tolerable. Hence the argument of Schmerr and Sedov can be valid for the short pulse case.

5- DISCUSSION: IMPLICATIONS AND APPLICATIONS FOR NDT

Although some of the results in chapter 4 have already been discussed, in this chapter the results are discussed in more detail, especially in terms of their implications for NDT. First the implications for individual echo responses and their interpretations are considered, before going on to discuss the implications for defect sizing using DGS diagrams.

This is followed by the introduction of a new method to use the model as a "theoretical standard block".

5.1 Interference effects on the echo response.

5.1.1 Short pulse

For small targets at close ranges (i.e. for $PD > \lambda$), interference between plane and edge waves does not take place when using wide band transducers that have pulse shapes similar to the short pulse source velocity shown in chapter 4 (section 4.2 and 4.3, p 58 and 60). An obvious consequence of this multipulse structure is that it could lead to false identification of non-existent targets. When the small target is off axis, the edge wave contribution becomes small and only the plane wave pulse will dominate the echo response. Hence the multipulse structure disappears. This implies that a skilled NDT operator can ease the detection of the target without any false interpretation by moving the transducer, so that the target is off-axis.

As the target size increases, the echo response consists mainly of plane waves. Hence the multipulse structure will be very small. As a result misinterpretations of the echo response will be minimised.

With short pulse transducers, at ranges where there is no overlapping between plane and edge waves, the variations in the amplitudes of the echo responses of small targets are small in the near field of the probe, since interference between plane and edge waves does not take place. At further ranges, where PD is less than λ , there is a rise in the amplitude of the echo response due to the overlapping between these waves.

As the target size increases, variations of echo amplitude with range is small since the echo response is mainly dominated by the plane-wave component.

Finally, it is of course likely that the shape of the target could dramatically change the echo waveform and hence the amplitude of the target. This is clearly seen, when comparing the echo amplitude of the 2mm diameter FBH's and the 2mm diameter round-bottomed holes shown in Figures 4.2.1 and 4.3.1. The difference in amplitude between the two targets is nearly 6dB. This means that, as would be anticipated, the flat-bottomed hole will give a larger amplitude than the round-bottomed hole despite both having the same diameter.

5.1.2 Multi-cycle pulses.

When the excitation pulse contains several cycles, interference between the plane and edge waves is clearly seen in the echo responses of the targets. This interference causes dramatic changes (unlike the short pulse measurements) in the shape and the amplitude of the echo responses of the targets, especially for small targets. As an example of the severe change in pulse shape that can occur, the measured echo response of the 2mm target using the long pulse transducer at 25mm range could give the false impression of two closely spaced targets. Again, this problem disappears if the target is off-axis.

The variation in the amplitude of the echo response of small targets with range in the near field of the probe, is shown to be very large, especially for small targets. This is confirmed experimentally, as seen in Figure 4.3.7 where the echo amplitude for the 2mm target at 47mm is nearly ten times the amplitude at 25mm range. These large variations in echo amplitude with range might give the impression of a target which is some ten times larger than its size.

As the target size increases, the contribution of the edge wave becomes smaller compared to that of the plane wave. As a result the variation in amplitude with range, in the near field of the probe, becomes smaller (as seen in Figure 4.3.8). For example, the ratio of echo amplitudes of a 4mm diameter target ($G = 0.2$) positioned at the same ranges as the 2mm diameter target, Figure 4.3.8, is equal to

1: 4. Although the ratio is smaller than that obtained for the echo amplitude of the 2mm diameter target, it still might give the impression of a target which is some four times bigger than its real size.

For larger targets which are nevertheless smaller than or equal to the transducer diameter ($G = 0.50$ and 1.00), the variations in echo response and amplitude with range are small. This again implies that errors in estimating target size will be smaller with such large targets.d

5.2 Defect sizing using DGS diagrams.

The new model, introduced in chapter 2, gave the ability to produce full theoretical DGS diagrams for flat-bottomed holes in a solid medium, positioned in the near and the far fields of the transducer and for arbitrary pulse shape. Hence defect sizing using the DGS method can be extended theoretically to the near field of the probe using rapidly generated "calibration" curves.

This work highlights the drawbacks in using DGS diagrams for defect sizing. For example, the fluctuations with range in the echo amplitude of small targets, within the near field of the transducer (excited with multi-cycle pulse), can cause misinterpretations of different size targets positioned at different distances. This is shown in the experimental DGS diagram obtained for 2mm target (Figure 4.2.2), where the difference in the echo amplitude of the same target but at different range can be 18dB. However, when the excitation pulse is short, the variations of echo amplitude with range are minimised. For example, the experimentally obtained DGS diagram for the same target (Figure 4.4.1) shows that the variation in the echo amplitude of the target with range when moving from 12mm to 60mm is about 5dB.

The main advantage that could be gained from the DGS curves is that they give a very good indication to the variations in echo amplitude with range. For example, for short pulse transducers they can show clearly that there is a rise in the amplitude with near field range for small targets. Also, they can warn the skilled operator, prior to the inspection process, of the large variation in the echo amplitude when a multi-cycle transducer is used.

Another practical fact which can be deduced about DGS diagrams is that these curves are not universal and they depend heavily on the transducer parameters. This means that each transducer requires a complete set of DGS diagrams. However, the ability of the new model to produce DGS diagrams for any

conventional transducer can eliminate this problem by producing calculated DGS diagrams for each probe.

In practical NDT, measurements of the target range might contain certain errors. Hence, there will be an error in determining the target size from the measured echo amplitude. Another application of the model is to relate such errors in target position to errors in measuring its size, especially in the near field of the transducer. In order to demonstrate this error, DGS diagrams for a series of target sizes of 1mm, 1.2mm, 1.4mm, 1.6mm, 1.8mm, and 2mm diameter were obtained assuming a 19mm diameter source excited with multi-cycle pulse centred at 5MHz. The range of these targets varied from 23mm to 47mm. Figure 5.2.1 shows these calculated DGS diagrams. To show how an error in the target range could lead to an error in its size is explained in the following example.

Consider Figure 5.2.1 and assume that the real target range was 31mm and its real size was 1.4mm. However, the measured target range was equal to 30mm. When trying to relate the measured range to the measured amplitude, the NDT operator would assume that the target size is 1.2mm. So, a difference of 1mm target range could lead to an error of more than 15% in the target sizing.

Also, from Figure 5.2.1 the possibility of errors in target sizing which come as a result of errors in target ranges increases when the ranges are close to the destructive interference ranges. This possibility, interestingly, decreases when the target ranges are closer to the constructive interference range. This effect arises from the way the waves are added or subtracted as mentioned in Section (4.4.3).

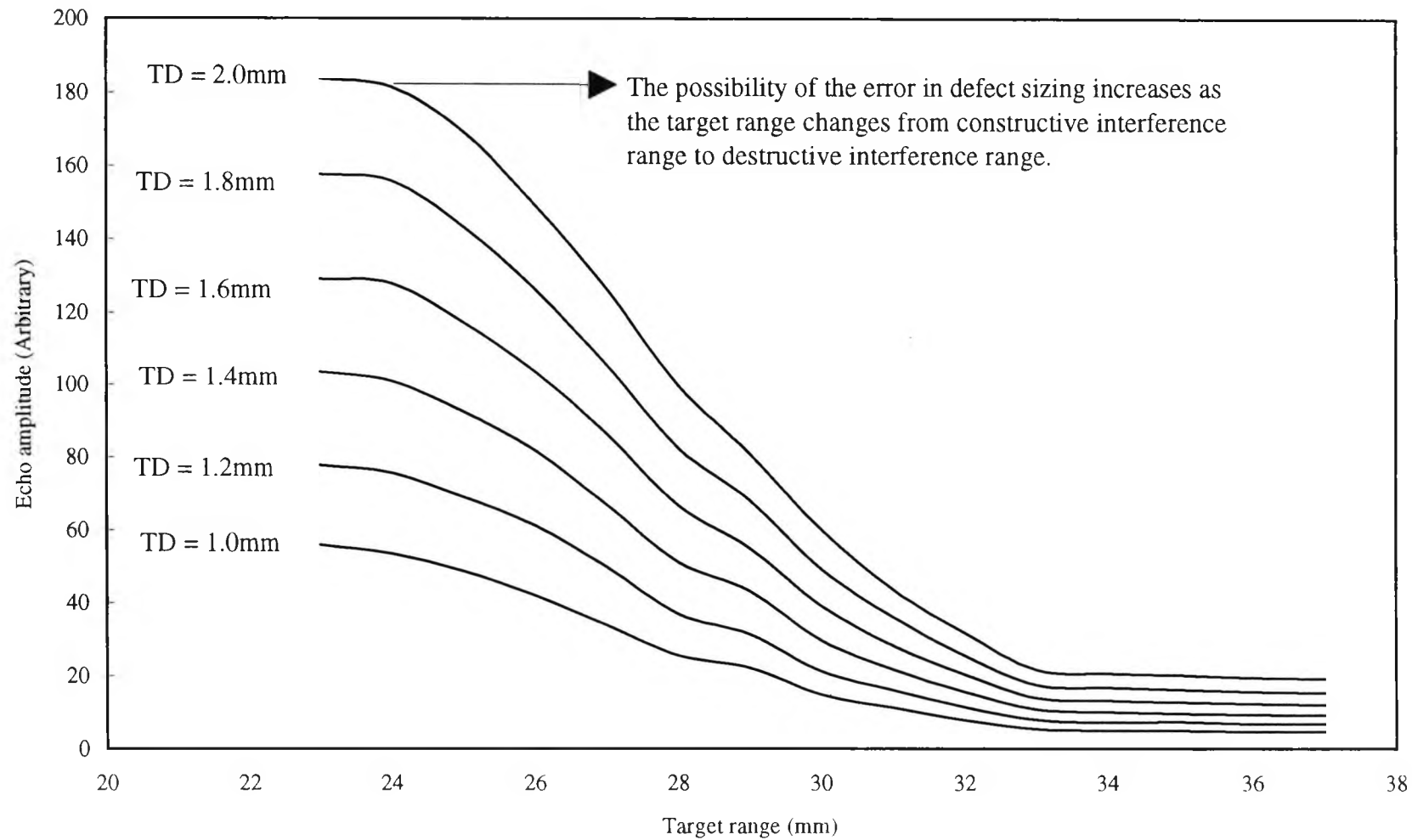


Figure 5.2.1: A section of DGS diagrams calculated for several target sizes which vary from 1mm to 2mm diameter. Note that closer to the destructive interference range, the possibility of defect sizing error increases. TD = Target Diameter

5.3 Application of the model as theoretical calibration blocks.

Standard reference blocks must be prepared from material with the same or similar alloy content, heat treatment and amount of hot or cold working as the material to be inspected, to ensure equal sonic velocity, attenuation and acoustic impedance in both reference standard and the test piece (ASTM handbook, 1989). These blocks can be divided according to their utility. For example, there are area-amplitude blocks and distance-amplitude blocks. The former deals with FBH's at a certain range in the block but with different size. The latter deals with FBH's having the same size but at different ranges in the block.

In the area-amplitude blocks, the holes should be in the very far field of the probe since at this range the echo amplitude is proportional to the target area. However this means that the blocks should have a certain thickness, so that the metal range is at least equivalent to the far field of the transducer. Here, the model can replace the area blocks by simulating the echo responses of the area amplitude blocks for the tested material. However, at the present, the simulation can only be done for materials that are very close to medium characteristics assumed by the model i.e. isotropic, very low noise and very low attenuation materials. For other test materials, reference blocks must be prepared. Since the model can be used by the NDT industry to simulate certain reference blocks, there are opportunity to save money and time. All that is needed to simulate the calibration blocks is to measure the sound speed in the material to be tested and the source velocity function for the transducer used in the testing. These parameters are then fed to the model and the theoretical reference curves can then be produced.

As a demonstration of the ability of the model to simulate such blocks, Figure 5.3.1 shows theoretical arbitrary echo amplitudes versus target area for various sizes of normally aligned, axial FBH's in aluminium. These results were obtained at 15mm range in the field of 19mm diameter transducer excited with single (solid line) and multi-cycle pulses (dotted line) centred at 5MHz. A peak-to-peak echo amplitude has been used in detecting all echo amplitudes. Target sizes range from 1mm

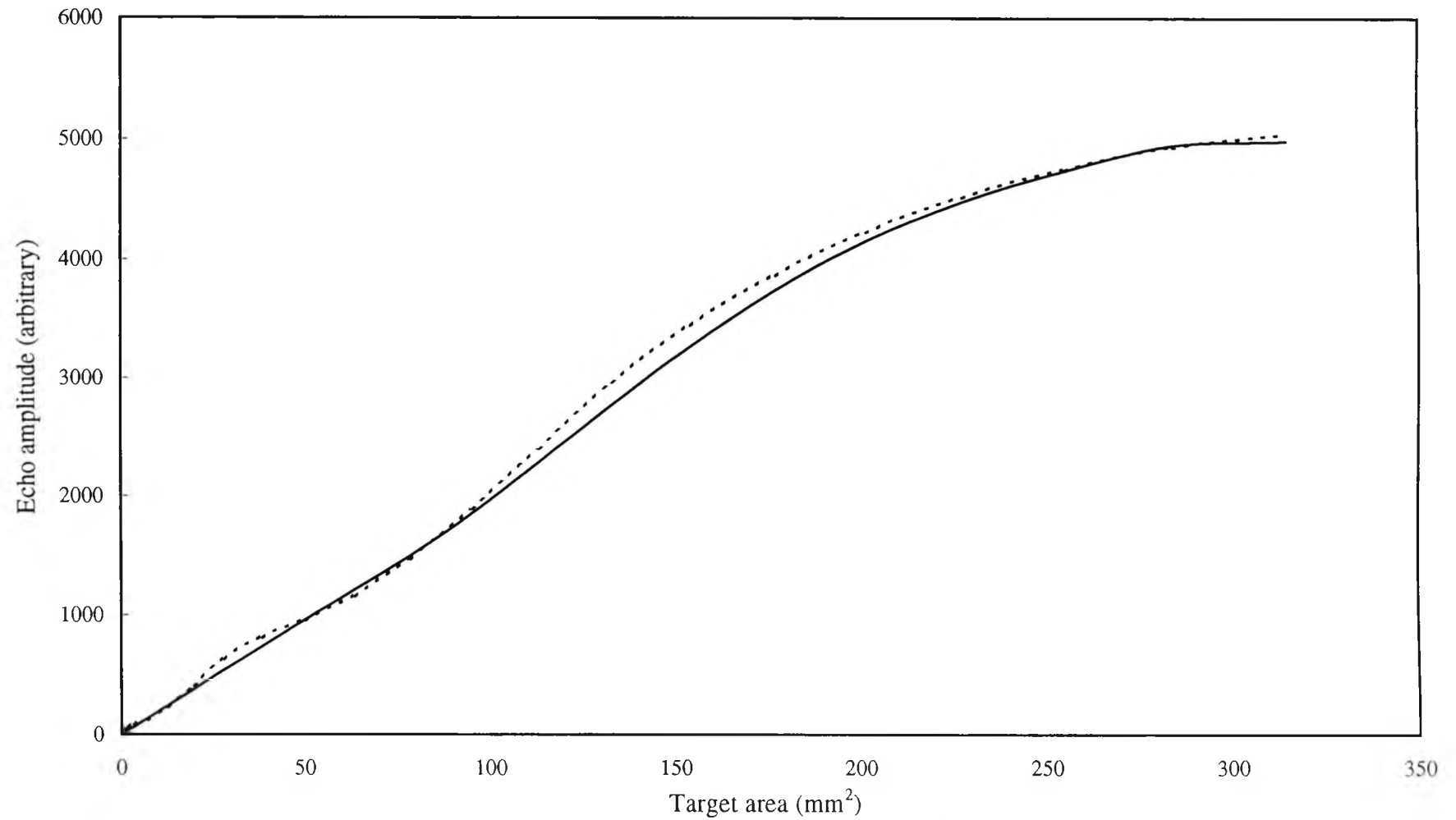


Figure 5.3.1: Area-amplitude curve at 15mm range. The echo amplitudes were obtained assuming a 5MHz and 19mm diameter circular transducer excited with single pulse (solid line) and multi-cycle (15cycles) pulse (dotted line).

diameter, up to a target with dimensions slightly larger than the source aperture (20mm diameter).

As seen in Figure 5.3.1, the echo amplitude is proportional to target area for all targets with a diameter less than 6mm assuming the single cycle pulse. Above this size there is a departure from linearity, the echo amplitude becoming greater than would be expected. As the target area approaches that of the transducer the rate of increase in the echo amplitude decreases. The reason for the deviation from linearity is explained elsewhere (Weight, 1984 and McLaren, 1987) and here the focus is towards the effect of the source velocity function on the area-amplitude relationship.

For the case of a multi-cycle pulse, the same behaviour can be seen, but there is a slight deviation from linearity for small targets. This could be due to the effect of the multi-cycle source velocity function on the echo responses, where interaction between plane and edge waves occurs. To demonstrate this effect on the echo response, an enlarged part of the curve shown in Figure 5.3.1 is given in Figure 5.3.2. This figure shows clearly the slight departure from linearity (for targets up to 20mm² in area) in the relation between echo amplitude and target area for the case of multi-cycle pulse. Also, from the figure the difference in echo amplitude calculated using the two different velocity functions for the same target area is relatively high. As an example, for a target diameter of 2mm, the difference in echo amplitude is nearly 40%. As the target size increases, the difference in the calculated echo amplitude, as seen in Figure 5.3.1, becomes smaller.

In order to demonstrate clearly the effect of interference between plane and edge waves on the area-amplitude relation, another curve is constructed for the same target sizes but at a range where destructive interference between plane and edge waves occurs (35mm) is shown in Figure 5.3.3. As seen in the figure, the echo amplitude for small targets obtained with the multi-cycle source velocity function is smaller than that obtained with single cycle. Figure 5.3.4 shows this large contrast in the echo amplitudes of small targets (0 to nearly 20mm²) using the two source

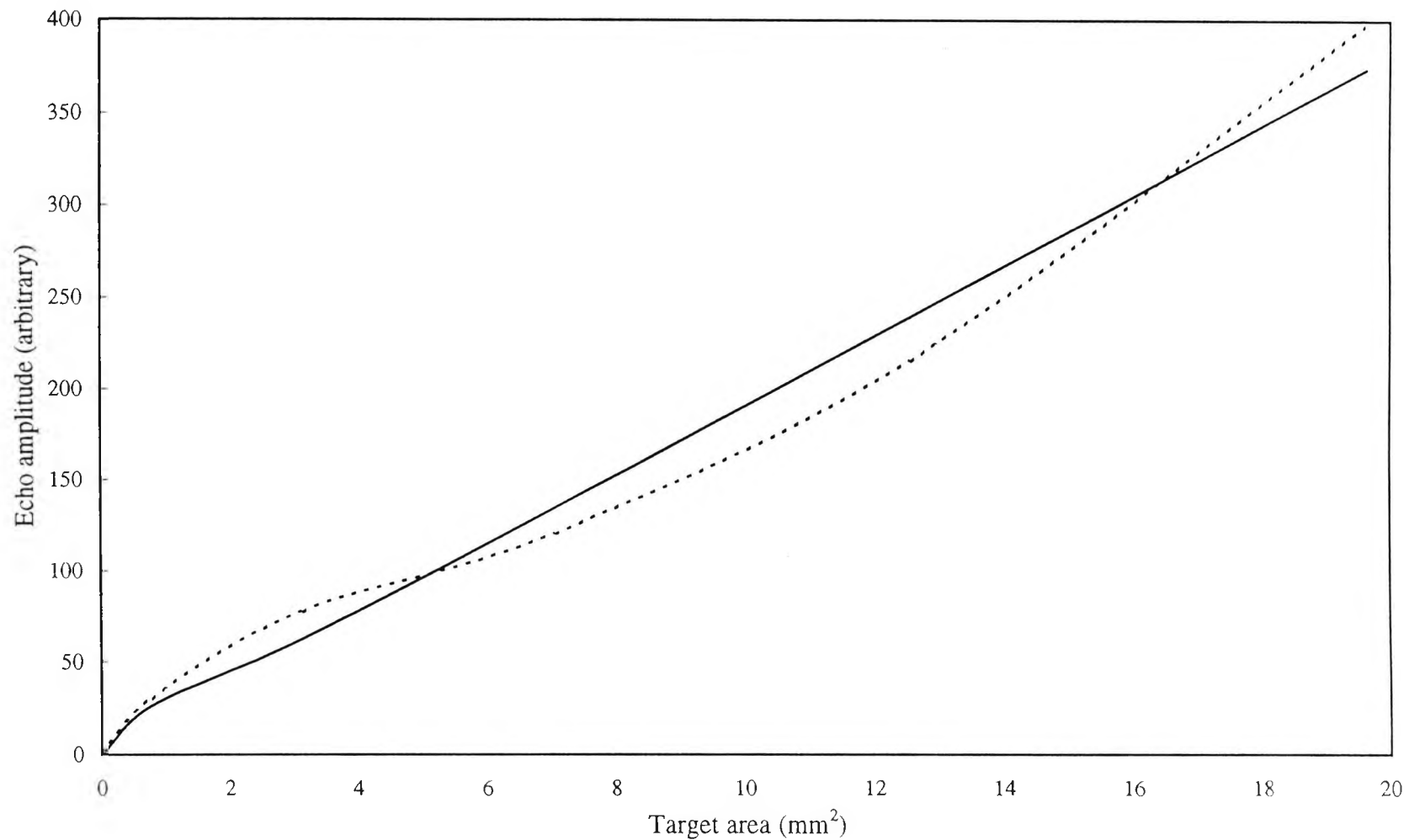


Figure 5.3.2: Enlarged view of the left hand side of the curve shown in figure 5.3.1. This enlargement shows clearly that the source velocity function produces small differences in the echo amplitude for the same target sizes at this range.

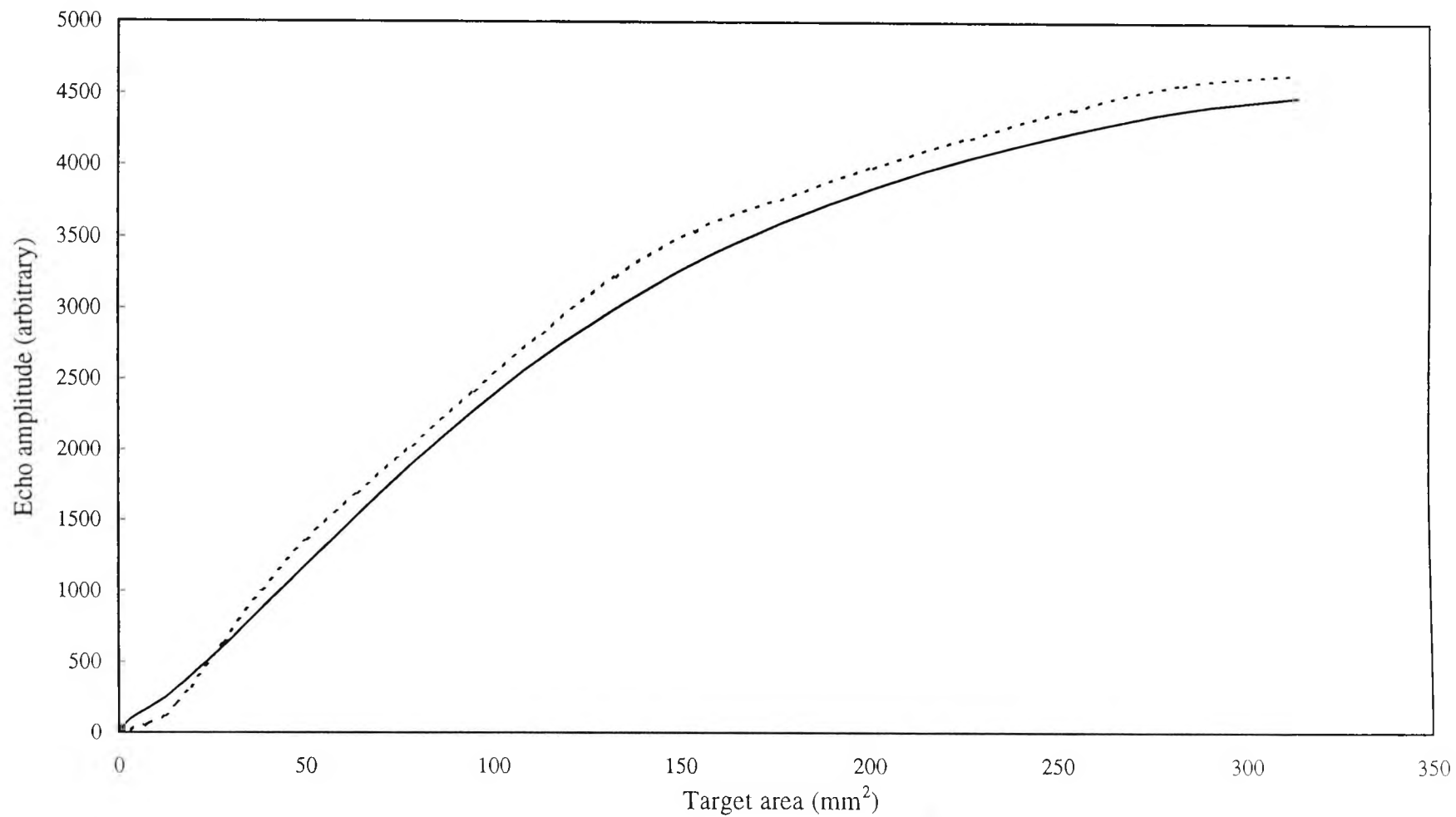


Figure 5.3.3: Area-amplitude curve at a destructive interference range (35mm). The echo amplitudes were obtained assuming the transducer parameters mentioned in figure 5.3.1 excited with single pulse (solid line) and multi-cycle pulse (dotted line).

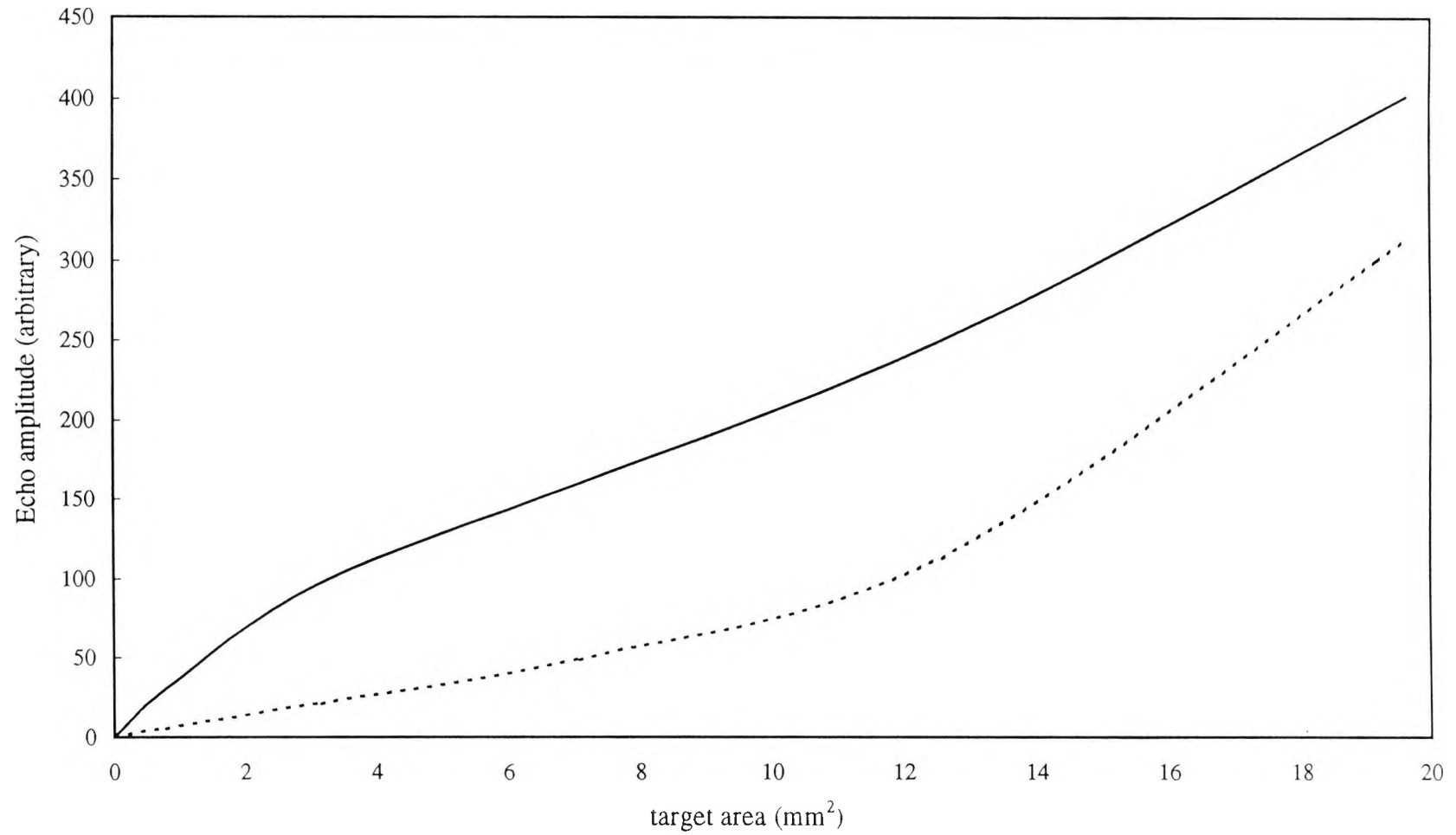


Figure 5.3.4: Enlarged view of the left hand side of the curve shown in figure 5.3.3. This enlargement shows clearly that the source velocity function can produce large differences in the echop amplitude for the same target size. These differences could reach up to 5 times and decreases as the target size increases.

velocity functions. For the 2mm diameter target, the echo amplitude using a multi-cycle pulse is lower than that calculated amplitude using the single pulse by nearly 14dB. As the target size increases, the interference effects become smaller. Hence, the difference in echo amplitude calculated for the targets using different source velocity functions becomes smaller. This is clearly seen for the 5mm diameter target, where the echo amplitude using multi-cycle pulse is only 2dB lower than that calculated using the single cycle pulse .

Figure 5.3.5 shows the same area-amplitude relation for the same target areas but at a range where constructive interference between the plane and edge waves occurs (22mm). As expected, the echo amplitude for small targets calculated assuming a multi-cycle pulse is larger than their echo amplitude calculated assuming a short pulse. This contrast can be clearly seen in the enlarged section of the area amplitude relation for small targets (0 to nearly 20mm²) shown in Figure 5.3.6. From the figure, the echo amplitude using the multi-cycle pulse is larger than that calculated using the single pulse by 7dB, for the 2mm diameter target case. Again, as the target size increases, the difference in echo amplitude becomes smaller. For 5mm diameter target the echo amplitude calculated using multi-cycle source function is higher than that calculated using short pulse only by 0.3dB.

The common fact concluded from Figures 5.3.1,3 and 5 is that for large targets the difference in echo amplitude calculated using both source velocity functions is small (the differences vary between 0.3dB to 1dB at the most). Hence, for targets larger than 5mm diameter, the source velocity function has only a small impact on the relation between target area and its echo amplitude.

As a final check on the use of the model as a theoretical calibration block, Figure 5.3.7, shows area-amplitude relation at a very far distance from the transducer (400mm) for the same target area. The source velocity function consists of 15 cycles centred at 5MHz. For small targets, a linear relation between target area and amplitude is clearly seen. However, as the target size increases there is a deviation

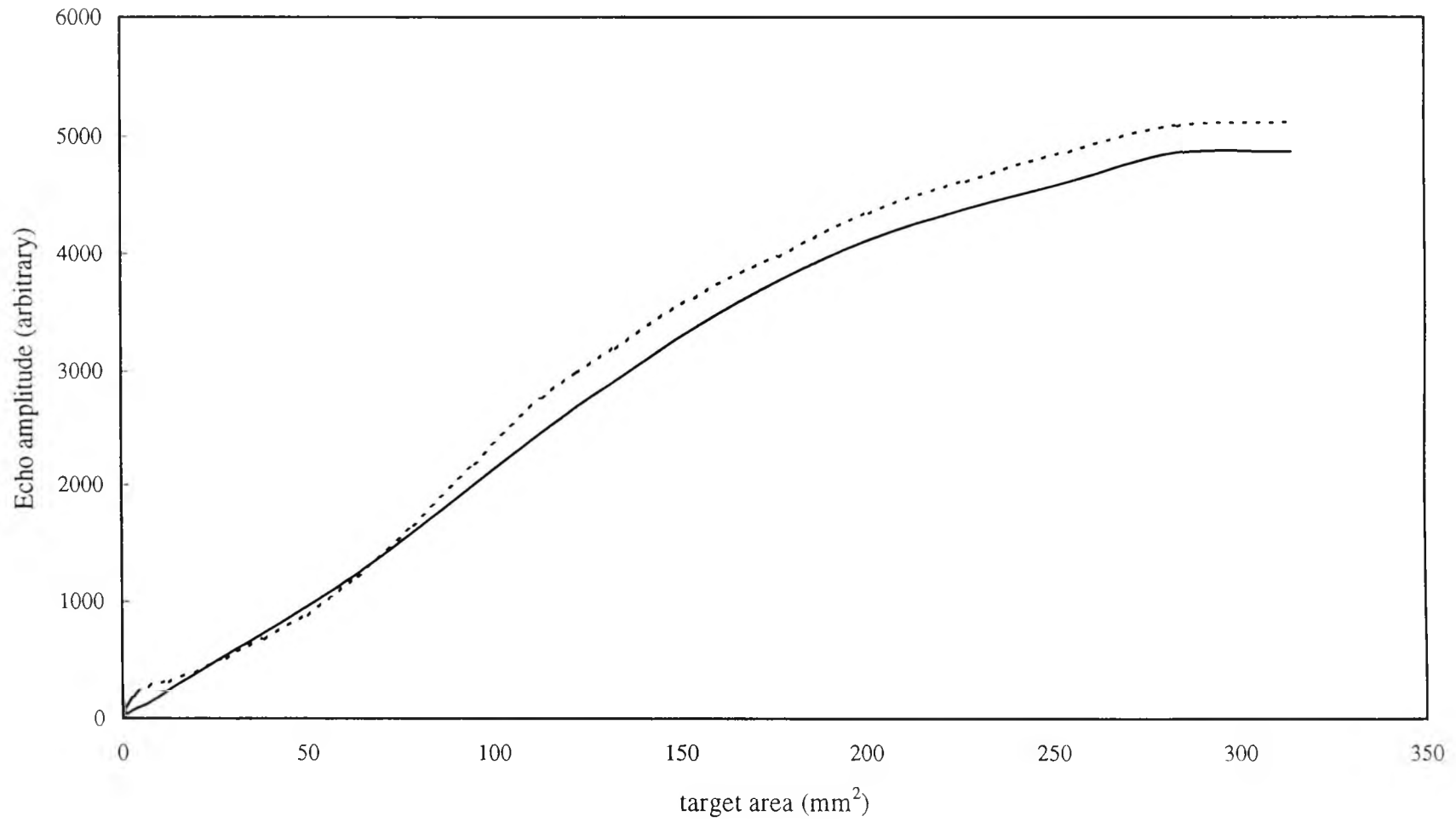


Figure 5.3.5: Area-amplitude curve at constructive interference range (22mm).

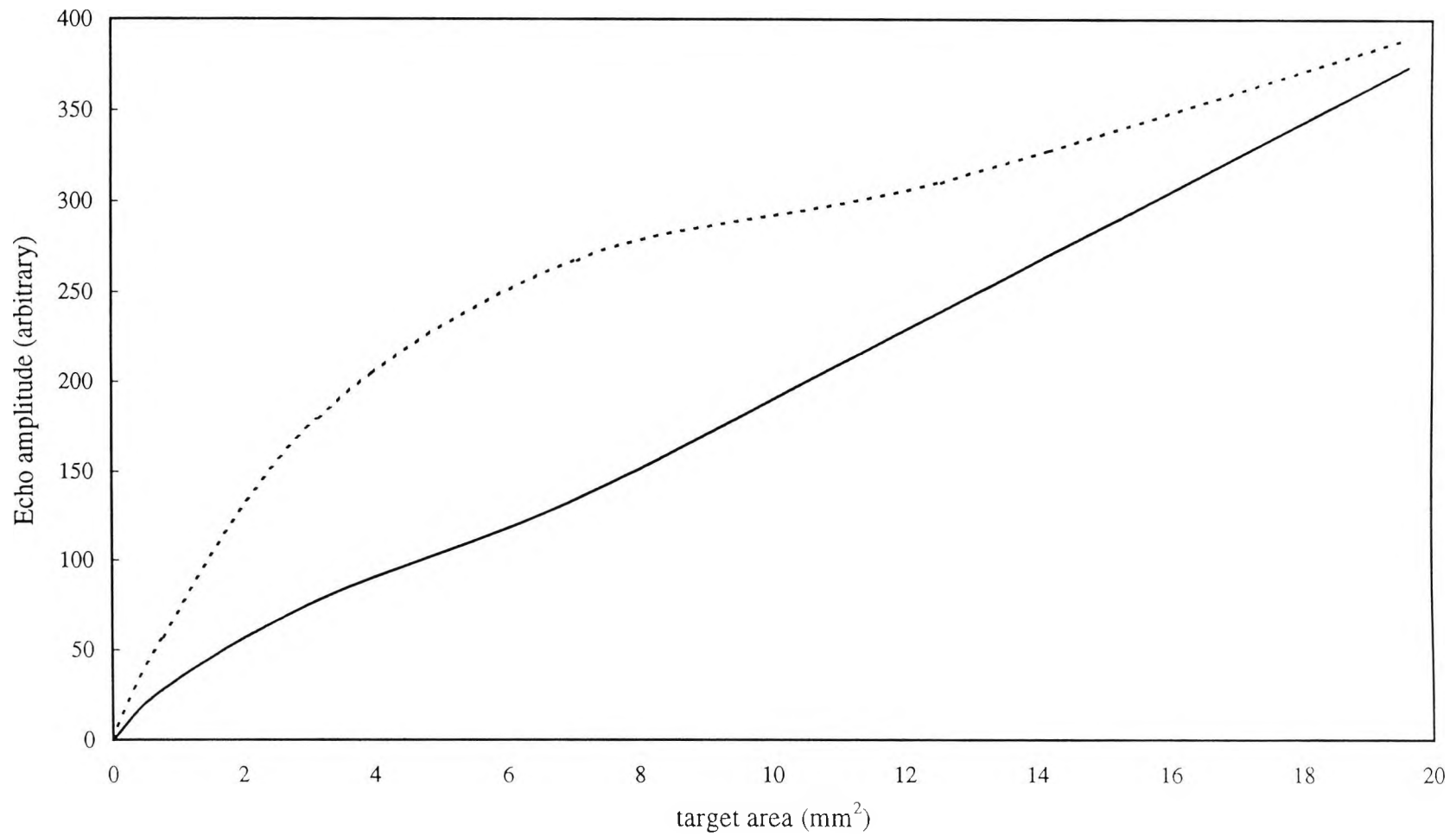


Figure 5.3.6: Enlarged view of the left hand side of the curve shown in figure 5.3.5. Note here that the difference in echo amplitude using produced for the same target sizes could as much as 2 times. This time, is larger using the multi-cycle pulse. The differences decrease as the target size increases.

from linearity. This theoretical deviation agrees well with similar deviations recorded experimentally (see for example, ASTM handbook, 1989).

Finally, a major conclusion that stems from Figures 5.3.1,3 and 5 is the amount of time and material that could be saved in producing the area-amplitude curves theoretically. In producing the same relation experimentally, three different blocks are needed for each range. In addition, the targets machining at each range require specialised machining and equipment.

In summary, the present model can be used as a theoretical standard to complement and extend current ultrasonic calibration and sizing procedures that use FBH's. In order to do this, it is suggested that a topic for future work could be to compare such theoretical curves with those measured using standard calibrations blocks..

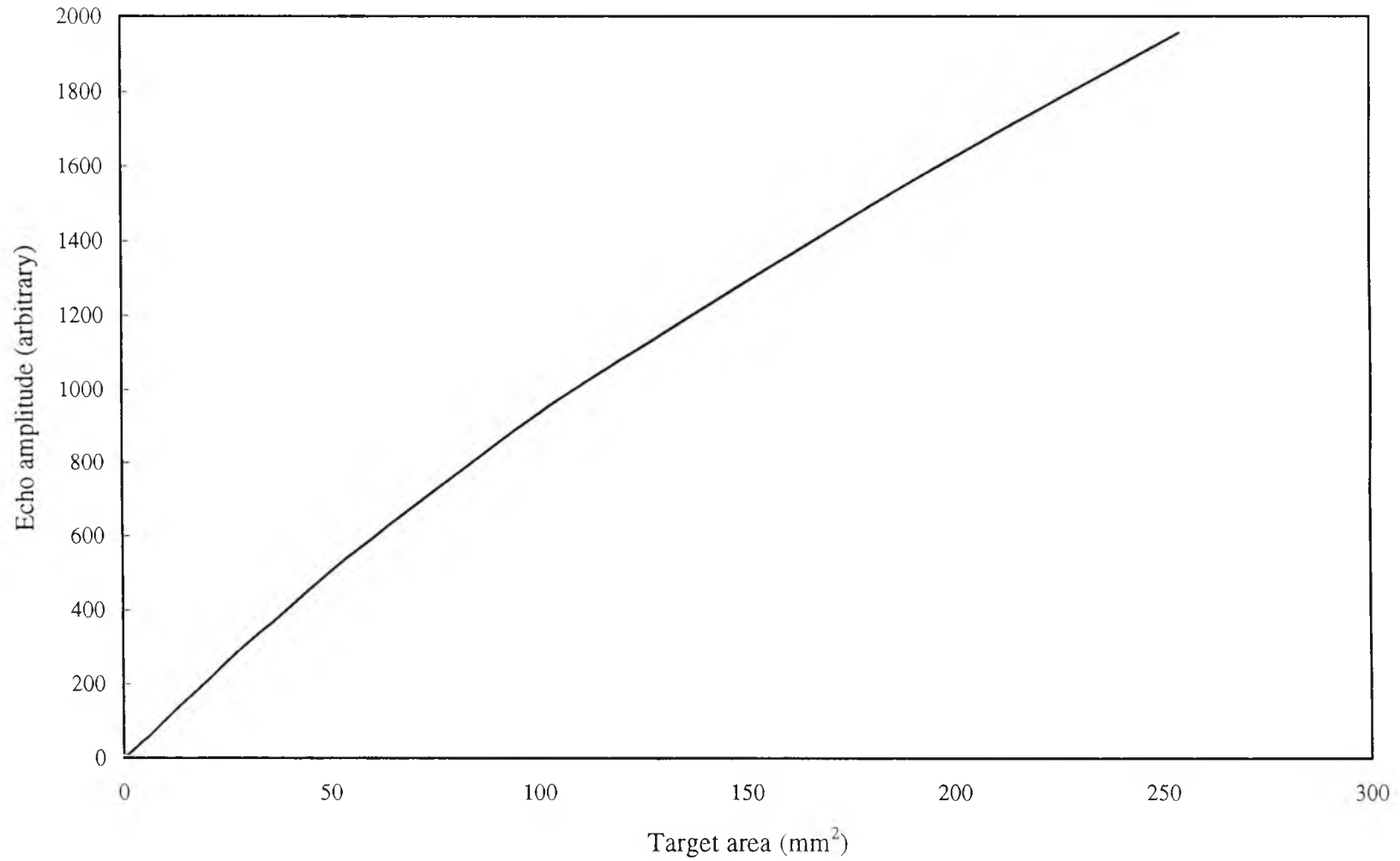


Figure 5.3.7: Area-amplitude curve at 400mm range. The curve behavior agrees with the experimental curve shown in the ASTM handbook

6- SUGGESTED FUTURE WORK

The main developments which can follow the present work can be divided into two parts. One deals with the development of the modelling. The other deals with DGS diagrams. These developments are summarised as follows.

It would be a great advantage if the model was modified so that it could calculate the echo responses of targets in anisotropic solids and not just the isotropic ones that the current model considers. This a very important step in the NDT industry, since many of the new composite materials are highly anisotropic materials.

The DGS diagrams produced using the model could be tested practically by determining the unknown size of a defect from its echo amplitude. This can be done by constructing a DGS diagram for a certain transducer and then using these curves to determine the size of the defect using 'blind' trials.

Finally, One of the further developments which could be made to the DGS diagrams is the extension of the current DGS diagrams to off-axis targets and not just on-axis targets. Because variations in echo amplitude with range will be minimised. It is left as a future work to produce these diagrams theoretically and compare them experimentally with measured ones.

7- CONCLUSIONS.

An earlier model for predicting echo responses for point-like targets in a homogeneous lossless solid can be extended to calculate echo responses for circular disc-like targets. The new model gives rapid calculation times compared to numerical methods and can be implemented on a PC. There is good agreement between the predictions of the model and the experimental measurements of the echo responses of flat-bottomed holes in aluminium. These verifications were done using both narrow and wide band transducers.

The model can be used to explain and aid the interpretation of the complicated multipulse structure of echoes from targets of simple geometry in terms of the propagation, scatter and reception of three waves: compression plane waves and compression- and shear-edge waves. Such structure can lead to false prediction of non-existent targets, especially for the case of small targets

The interference between plane and edge waves seen in the echo responses for targets using transducers excited with multi-cycle pulses can dramatically affect the shape and amplitude of the responses. For example, the amplitude of the echo response for a given target at different ranges in the near field can vary by a factor of 10.

A calculated section of a DGS diagram plotted using the new model shows good agreement with an experimental curve obtained from measurements of the echo responses from a number of mostly near-field FBH targets in aluminium. This comparison was done using transducers excited with short and multi-cycle pulses.

The new model has been used to produce full theoretical DGS diagrams for targets in a solid. These diagrams take into account the effect of the radiated shear edge waves that exist even with directly coupled compression wave transducers and shear waves produced by the process of mode conversion at the target. Also, the same model is used to explain the form of these diagrams produced for transducers excited with short and multi-cycle pulses. For example, with a transducer excited

with a short pulse there are no near field fluctuations in the relative echo amplitude of the targets with range. However, when a multi-cycle pulse is used, there are large variations in the echo amplitude of the target with range in the near field of the probe, especially for small targets. These variations could reach 20dB for smaller values of G (0.05, 0.10).

Some factors, such as the transducer radius, source velocity function and the method by which the echo amplitude is detected, are shown to have some effects on multi-cycle DGS diagrams. These effects are most pronounced when the targets are at ranges where destructive interference between plane- and edge-wave components occurs.

Comparison between short pulse DGS diagrams calculated assuming either a fluid-like medium or a solid medium, shows that the relative echo amplitudes of the targets in the case of the fluid model are slightly higher than the echo amplitudes of targets in the case of the solid model, especially for the case of small targets. This was verified when the two models are compared with experimentally obtained DGS diagrams using 2mm diameter FBH targets in aluminium. However for larger targets, there is in general good agreement between the two models.

For the case of a transducer excited with a multi-cycle pulse, the DGS diagrams produced assuming a fluid or solid model have a similar form. There are however, localised differences that can result in errors of around a factor of 2 if a fluid model is used to calculate DGS curves subsequently used to estimate the size of the target in a solid. Again, this is mostly noticed for small targets. These differences were also verified when comparing DGS diagrams calculated using both models with experimentally obtained curves for the case of 2mm diameter FBH targets in aluminium. This means that a more accurate way of defect sizing using the DGS diagrams method could be implemented using the solid model.

For DGS diagrams produced assuming a short pulse, the differences between the solid and the fluid models are small even for the case of small targets. This was

verified when comparing DGS curves produced by both models with experimentally obtained curves for 2mm diameter FBH's. Hence the fluid models can be used to size defects in solids provided that wide-band short pulse transducers are used.

The accuracy of target sizing using DGS diagrams can be optimised by calculating a set of curves for all of the experimental conditions pertaining. But it must be borne in mind that a major drawback of the DGS method remains, the assumption of planar, normally-aligned targets.

The applications of the model could be extended further so as to be used as 'theoretical standard area and distance blocks'. This was shown theoretically, especially for the case of area blocks. It was also shown that the source velocity function can dramatically affect the area-amplitude relationship, especially for small targets.

REFERENCES

J. D. Achenbach,

"Recent developments in ultrasonic modelling for crack detection and characterisation, in: Mathematical modelling in NDT (Clarendon press, Oxford", 35-55, (1988) .

K. Aki and P. G. Richard,

"Quantitative seismology- Theory and experiments, Freeman, San francisco, 1980.

J. C. Baboux and R. Kazys,

"Analysis of the transient ultrasonic fields radiated by in solids by circular and annular sources", J. Acoust. Soc. Am., 92, 2942-2951, (1992).

P. Bastien,

"Difficulties in the ultrasonic of defects size", Non-destructive testing, 147-151, (1968).

H. E. Boyer,

"Metals Handbook, 9th Edition, vol. 17, Nondestructive inspection and quality control", (1989).

G. Bradfield,

"Correlating echo and flaw magnitudes", Letter to the Editor of Non-Destructive Testing, 317-318, (1968).

L. F. Bresse and D. A. Hutchins,

"Transient generation of elastic waves in solids by a disk-shaped normal face source", J. Acoust. Soc. Am., 86, 810-817, (1989).

M. Certo,

"Mathematical modelling of ultrasonic inspection", Proceeding of 3rd European Conference on NDT, Florence, Italy, 345-354, (1984).

R. K. Chapman,

"An integrated model of ultrasonic NDT and its practical applications, in: Mathematical modelling in NDT Proc.", Clarendon press, Oxford, 209-232, (1988).

H. Djelouah and J. C. Baboux,

"Transient ultrasonic field radiated by a circular transducer in a solid medium", J. Acoust. Soc. Am., 92, 2932-2941, (1992).

G. A. Georgiou, M. Blackmore, R. Chapman and D. Firth,

"The application of the geometrical theory of diffraction to modelling pulsed ultrasonic inspection: A system model", Br. J. NDT., vo31, No.10, 551-561, (1989).

K.G. Hall,

"A Qualtitative evaluation of variable angle ultrasonic transducers by the photo elastic visualisation method", Ultrasonics, 15, 245-252, (1977).

- R. Halmshaw,**
"Nondestructive Testing of Materials", Edward Arnold, London, (1991)
- A. J. Hayman,**
"Schlieren visualisation of focused ultrasonic images", PhD thesis, The City University, London, (1982).
- A.J. Hayman and J.P. Weight,**
"Transmission and reception of short ultrasonic pulses by circular and square transducers", J. Acoust. Soc. Am., 66, (945-951).
- J. D. Hislop,**
"Flaw size evaluation in immersed ultrasonic testing", Non-destructive testing, 183-192, (1969).
- A. T. de Hoop,**
"A modification of Cagniard's method for solving seismic wave problems", Appl. Sci. Res., B8, 349-365, (1959).
- A. Ilan and J. P. Weight,**
"The propagation of short pulses of ultrasound from a circular source coupled to an isotropic solid", J. Acoust. Soc. Am., 88, 1142-1151, (1990).
- K. Kawashima,**
"Quantitative calculation and measurement of longitudinal and transverse ultrasonic wave pulses in solid", IEEE Trans. Sonics. Ultrason. SU-31, 83-94, (1984).
- J. Krautkramer,**
"Determination of the size of defects by the ultrasonic impulse echo method" British Journal of Applied Physics. 10, 240-245 (1959).
- V. Krstelj and D. Markucic,**
"Mathematical modeling of disk reflector response as a contribution to the in situ ultrasonic inspection", Rev. Sci. Instrum, 68 (3), 1557-1563, (1997).
- K. J. Langenberg, U. Aulenbacher,**
"Recent developments in ultrasonic modelling for crack detection and characterization", in: Institute of mathematics conference on mathematical modelling in NDT, Jesus College, Cambridge, (1986).
- A. Lhemery,**
"A model for the transient ultrasonics field radiated by an arbitrary loading in solid", J. Acoust. Soc. Am., 96, 3776-3786, (1994).
- A. Lhemery,**
"Impulse response method to predict echo responses from defects in solids. part I. Theory", J. Acoust. Soc. Am. 98, 2197-2208, (1995).

S. McLaren,

"High resolution ultrasonic nondestructive testing", PhD thesis, The City University, London, (1987).

S. McLaren and J. Weight,

"Transmit-receive mode responses from finite-sized targets in fluid media", *J. Acoust. Soc. Am.* 82, 2102-2112, (1987).

A. McNab and G. Muir,

"Flaw Sizing of Real Defects", *British Journal of NDT*, 130-134, (1978).

J. A. Ogiliviy and I. D. Culverwell,

"Elastic model for simulating ultrasonic inspection of smooth and rough defects", *Ultrasonic*, 29, 490-496, (1991).

D.E. Robinson, S. Lees, and L. Bess,

"Near field transient radiation patterns for circular pistons", *IEEE Trans. Acoust. Speech signal process. ASSP-22*, 395-403, (1974).

W. Sachse, N. N. Hsu, and D. G. Eitzen,

"Visualisation of transducer produced sound fields in solids", *IEEE Symposium Proc.*, 139- 143, (1978).

L. Schmerr and A. Sedov,

"The Flat bottom hole: An ultrasonic scattering model", *Res Nondestr Eval*, 1: 181-196, (1989).

L. Schmerr and A. Sedov,

"An elastodynamic model for compressional and shear wave transducers", *J. Acoust. Soc. Am.*, 86(5), 1988-1999, (1989).

A. Sedov, L. Schmerr and S. J. Sung,

"Ultrasonic scattering by a flat-bottom hole in immersion testing"
J. Acoust. Soc. Am. 92, 478-486 (1992).

R. Stacey and J. P. Weight,

"Ultrasonic response from targets in solid media using finite difference methods", *IEE Proceedings-A*, Vol. 140, No. 4, 303-316, (1993).

P. R. Stepanishen,

"Transient radiations from pistons in an infinite planar paffle", *J. Acoust. Soc. Am.* 49, 1629-1638, (1971).

M. A. Sumbatyan,

"Calculation of reflection diagram from a circular crack for a normal ultrasonic fault finder", *Sov J Solid Mech* (translated to english by Allerton Press), 24, 128-132, (1989).

M. A. Sumbatyan and N. V. Boyev,

"Mathematical modeling for the practice of ultrasonic inspection" *Ultrasonics*, 32, 5-11 (1994).

S. J. Sung, L. Schmerr and A. Sedov,

"DGS diagrams and frequency response curves for a flat bottom hole: A model-based approach", *Res Nondestr Eval*, 3: 201-219, (1991).

L. Wang, J. Deng and J. Shen

"A time-domain boundary element model for ultrasonic pulse echo", *Ultrasonics*, 35 125-130, (1997).

J. P. Weight and A. J. Hayman,

"Observation of the propagation of very short Ultrasonic pulses and their reflection by small targets," *J. Acoust. Soc. Am.* 63,396-404 (1978).

J. P. Weight,

"A model for the propagation of short pulses of ultrasound in a solid," *J. Acoust. Soc. Am.* 81, 815-826 (1987).

J. P. Weight,

"A model to predict the ultrasonic echo responses of small targets in solids", *J. Acoust. Soc. Am.*, 94 (1), 514-526, (1993).

J. P. Weight,

"Ultrasonic beam structure in fluid media", *J. Acoust. Soc. Am.*, 76, 1184-1193, (1984).

J. P. Weight,

"The propagation and reception of wide-band ultrasonic pulses", PhD thesis, The City University, London, (1982).

C. Wells,

"Have we the answer to the need for recording both ultrasonic weld testing and sensitivity?", *British Journal of N. D. T.* 78-86, (1968).

V. Whittaker,

"A review of non-destructive measurement of flaw size". *British Journal of N. D. T.* 92-100, (1972).

C. F. Ying, M. X. Li, and H. L. Zhang,

"Computations and measurements of transient stress waves and electrical voltages generated by transmitting ultrasonic piezoelectric transducers.", *Ultrasonics*, 19, 155-158, (1981).

Appendix

Table 1: Expressions for the angle of equidistant arc (2Ω) on the surface of a circular source (after Robinson). The axis and other variables are defined in Figure 2.1.

Region	Time Limit	Ω (ct)
Inside geometrical beam, $y < R$	$t_0 \leq t \leq t_1$	π
	$t_1 \leq t \leq t_2$	$\cos^{-1}\left(\frac{c^2 t^2 - x^2 + y^2 - R^2}{2y(c^2 t^2 - x^2)^{0.5}}\right)$
On edge, $y=R$	$t = t_0 = t_1$	$\pi/2$
	$t_1 < t \leq t_2$	$\cos^{-1}\left(\frac{(c^2 t^2 - x^2)^{0.5}}{2R}\right)$
Outside geometrical beam, $y > R$	$t_0 < t < t_1$	0
	$t_1 \leq t \leq t_2$	$\cos^{-1}\left(\frac{c^2 t^2 - x^2 + y^2 - R^2}{2y(c^2 t^2 - x^2)^{0.5}}\right)$

where

$$\begin{aligned}
 t_0 &= x/c, \\
 t_1 &= (1/c)[(R-y)^2 + x^2]^{0.5}, \\
 t_2 &= (1/c)[(R+y)^2 + x^2]^{0.5}.
 \end{aligned}$$